UNIVERSIDADE FEDERAL DE SÃO CARLOS
CENTRO DE CIÊNCIAS EXATAS E DE TECNOLOGIA
PROGRAMA DE PÓS-GRADUAÇÃO EM CIÊNCIA E ENGENHARIA DE MATERIAIS

CRACK NETWORK MONITORING UPON CURING AND DRYING OF HIGH-ALUMINA MgO-CONTAINING REFRACTORY CASTABLE VIA DIGITAL IMAGE CORRELATION

Vinicius Fiocco Sciuti

São Carlos
December 2020

UNIVERSIDADE FEDERAL DE SÃO CARLOS
CENTRO DE CIÊNCIAS EXATAS E DE TECNOLOGIA
PROGRAMA DE PÓS-GRADUAÇÃO EM CIÊNCIA E ENGENHARIA DE MATERIAIS

CRACK NETWORK MONITORING UPON CURING AND DRYING OF HIGH-ALUMINA MgO-CONTAINING REFRACTORY CASTABLE VIA DIGITAL IMAGE CORRELATION

Vinicius Fiocco Sciuti

Tese apresentada ao Programa de Pós-Graduação em Ciência e Engenharia de Materiais como requisito parcial à obtenção do título de DOUTOR EM CIÊNCIA E ENGENHARIA DE MATERIAIS

Orientador: Dr. Rodrigo Bresciani Canto
Coorientador: Dr. Victor Carlos Pandolfelli
Agência Financiadora: Capes/PROEX - Processo: 88882.332721/2018-01
Capes/PDSE - Processo: 8881.188511/2018-01

São Carlos
December 2020

To everyone I met and with whom I shared, even during coffee breaks, the challenges and achievements of this Ph.D.

CANDIDATE'S VITAE

Master's degree in Material Science and Engineering by Graduate Program in Materials Science and Engineering – PPGCEM - UFSCar – (2016)

Bachelor's degree in Materials Engineering by Federal University of São Carlos – UFSCar – (2014)

UNIVERSIDADE FEDERAL DE SÃO CARLOS

Centro de Ciências Exatas e de Tecnologia
Programa de Pós-Graduação em Ciência e Engenharia de Materiais

Folha de Aprovação

Defesa de Tese de Doutorado do candidato Vinicius Fiocco Sciuti, realizada em 23/12/2020.

Comissão Julgadora:

Prof. Dr. Rodrigo Bresciani Canto (UFSCar)

Prof. Dr. Marco Aurelio Liutheviciene Cordeiro (UFSCar)

Prof. Dr. François Hild (CNRS)

Prof. Dr. Nicolas Pierre Schmitt (UPEC)

Prof. Dr. Ricardo Afonso Angélico (USP)

O presente trabalho foi realizado com apoio da Coordenação de Aperfeiçoamento de Pessoal de Nível Superior - Brasil (CAPES) - Código de Financiamento 001.
O Relatório de Defesa assinado pelos membros da Comissão Julgadora encontra-se arquivado junto ao Programa de Pós-Graduação em Ciência e Engenharia de Materiais.

ACKNOWLEDGMENT

To CAPES - Coordenação de Aperfeiçoamento de Pessoal de Nível Superior for the financial support to this Ph.D by a PROEX grant # 88882.332721/2018-01.

This study was financed in part by the Coordenação de Aperfeiçoamento de Pessoal de Nível Superior - Brasil (CAPES) - Finance Code 001.

Also the financial support by the PDSE grant #8881.188511/2018-01 used during my internship at LMT, CAPES (Brazil).

ABSTRACT

Crack Network Monitoring upon Curing and Drying of High-Alumina MgO-Containing Refractory Castable via Digital Image Correlation

MgO particles are added to high-alumina refractory castable formulations to form spinel at high temperatures. However, these particles react with water forming brucite, which causes heterogeneous expansions in the material that usually induces damage. Damage was studied by Impulse Excitation Techniques, which gives access to a global Young's modulus. Digital Image Correlation (DIC) is a full-field technique that can provide field information about damage. In this dissertation, DIC was applied to cubic and bar-shaped specimens of the refractory castable mentioned, during curing and drying, in an in-house climatic chamber. This application was validated by tomographic volumes that showed cracks initiating on the surface and propagating to the center of the specimen. The images were analyzed using the software Correli-3.0, which implements a global approach (*i.e.,* FE-based DIC). The Mechanical Regularization and the Brightness and Contrast Correction tools were applied to enhance the use of fine discretizations. The cracks were identified and quantified using maximum principal strain fields, which is the basis of other parameters defined in the dissertation (*e.g.,* the Mean Crack Opening Displacement and the Surface Crack Density). The importance of a Representative Elementary Volume was highlighted by comparing the results of cubic and bar-shaped specimens. Further, the Principal Component Analysis was applied to the displacement and the maximum eigen strain fields obtained via DIC. It revealed the crack network as the most relevant component with a temporal development of a sigmoidal curve where a two-parameter Weibull law was satisfactorily fitted. The approach allows the need for user-defined thresholds to be avoided for crack quantification Finally, an Adaptive Meshing (AM) procedure was implemented to locally refine the mesh on regions with cracks.

Keywords: Digital Image Correlation; Crack Network; Singular Value Decomposition; Adaptive Meshing

RESUMO

Monitoramento da rede de trincas durante a cura e secagem de concreto refratário aluminoso contendo MgO via Correlação de Imagens Digitais

Partículas de MgO são adicionadas a formulações de concretos refratários aluminosos para formar espinélio em altas temperaturas. Estas partículas reagem com a água formando brucita durante o processamento do concreto, causando expansões localizadas que geralmente danificam o material. A evolução do dano vem sendo estudada pela técnica de Excitação por Impulso (EI), na qual este é uniformizado por todo o CDP. Correlação de Imagens Digitais (CID) é uma técnica que proporciona informações mais detalhadas como campos de dano. Nesta tese, a CID foi aplicada para CDPs de formato cúbico e de barra, produzidos com o concreto refratário mencionado. O concreto foi curado e secado em uma câmara climática construída no laboratório, a qual possui janelas para aquisição de imagens. A aplicação da CID foi validada por análise de todo o volume de um CDP via tomografia, a qual permitiu observar que as trincas se iniciam na superfície e propagam para o centro. Métodos de Regularização Mecânica e de Correções de Brilho e Contraste foram aplicados para utilizar discretizações refinadas. As trincas foram identificadas e classificadas usando os campos de deformação principal máxima. A Análise de Componentes Principais (ACP) foi aplicada aos campos de deslocamento e deformação principal máxima obtidos via CID. Os resultados da ACP revelaram que a rede de trincas é a componente mais relevante e sua evolução no modo temporal tem um formato sigmoide, ao qual foi possível ajustar satisfatoriamente uma lei de Weibull. Um procedimento que utiliza uma Malha Adaptativa (MA) foi implementado para refinar a malha de maneira local em regiões que contêm trincas. Os métodos desenvolvidos nesta tese demonstraram ser viáveis para a análise da evolução do dano durante a cura e secagem de materiais refratários e têm potencial para a aplicação em outros fenômenos que envolvem a fissuração superficial de materiais por imagens digitais.

Palavras-chaves: Correlação de Imagens Digitais; Rede de trincas; Decomposição em Valores Singulares; Malha Adaptativa.

Publications

de Melo, C. C., Macêdo, S., Sciuti, V. F., Canto, R. B. (2019). A novel mechanical test for the stress relaxation analysis of polymers. Polymer Testing, 73, 276-283.

Luchini, B., Sciuti, V. F., Angélico, R. A., Canto, R. B., Pandolfelli, V. C. (2017). Critical inclusion size prediction in refractory ceramics via finite element simulations. Journal of the European Ceramic Society, 37(1), 315-321.

Sciuti, V. F., Melo, C. C., Canto, L. B., Canto, R. B. (2017). Influence of surface crystalline structures on DSC analysis of PTFE. Materials Research, 20(5), 1350-1359.

Luchini, B., Sciuti, V. F., Angélico, R. A., Canto, R. B., Pandolfelli, V. C. (2016). Thermal expansion mismatch inter-inclusion cracking in ceramic systems. Ceramics International, 42(10), 12512-12515.

Sciuti, V. F., Hild, F., Pandolfelli, V. C., Santos, T., Smaniotto, B., Canto, R. B. (2020). Digital Image Correlation applied to *in situ* evaluation of surface cracks upon curing of MgO-containing refractory castables. Journal of the European Ceramic Society, 41(1), 1003-1014

Sciuti, V. F., Canto, R. B., Neggers, N., Hild, F. (2020). On the benefits of correcting brightness and contrast in global digital image correlation: Monitoring cracks during curing and drying of a refractory castable. Optics and Lasers in Engineering, 136, 106316

x

SUMMARY

LIST OF TABLES

LIST OF FIGURES

LIST OF ABBREVIATIONS

AM: Adaptive Meshing

ASTM: American Society for Testing and Materials

AVE: Apparent Volumetric Expansion

BCC: Brightness and Contrast Corrections

BC: Brightness and Contrast

BR: Bar Resonance

CAC: Calcium Aluminate Cements

CM: Caustic Magnesia

DBM: Dead Burnt Magnesia

DEMa: *Departamento de Engenharia de Materiais - UFSCar*

DIC: Digital Image Correlation

DOF: Degree Of Freedom

DVC: Digital Volume Correlation

FE: Finite Element

FM: Fine Mesh, related to BCC

FMB: Fine Mesh brightness correction, related to BCC

FMB: Fine Mesh contrast correction, related to BCC

FMBC: Fine Mesh brightness and contrast correction, related to BCC

GLR: Gray Level Residuals

GIMP: GNU Image Manipulation Program

H: Relative air humidity [%]

HA: Hydratable Alumina

IET: Impulse Excitation Technique

ITZ: Interfacial Transition Zone

LMT: *Laboratoire de Mécanique et Technologie*

MCOD: Mean Crack Opening Displacement [m]

MR: Mechanical Regularization

NURBS: Non Uniform Rational Basis Spline

PCA: Principal Component Analysis

PGD: Proper Generalized Decomposition

Q8: 8-noded quadrilateral element, related to BCC

Q8B: Q8 element brightness correction, related to BCC

Q8C: Q8 element contrast correction, related to BCC

Q8BC: Q8 element brightness and contrast corrections, related to BCC

RMS: Root Mean Square

ROI: Region Of Interest

RVE: Representative Volume Element

SCD: Surface Crack Density [%]

SEM: Scanning Electron Microscopy

SM: Spatial Mode, related to PCA

STD: Standard Deviation

SVD: Singular Value Decomposition

T: Temperature [°C]

TGA: Thermogavimetric Analyses

TM: Temporal Mode, related to PCA

T3: 3-noded triangular element

UFSCar: *Universidade Federal de São Carlos*

UM: uniform mesh, related to Adaptive meshing

UWP: Ultra-sound Wave Propagation

ZNCC: Zero-Normalized Cross-Correlation

ZOI: Zone Of Interest

LIST OF SYMBOLS

- $\boxtimes$: symmetrized tensorial product $[\mathbf{L}]$, related to AM
- α: power law exponent [-1 to -2], related to AM
- A: factor to account for expansion strains before cracking, related to MCOD and SCD
- $\{\boldsymbol{\beta}\}$: vector of unknows, related to AM
- b: brightness correction field, related to BCC
- b_k: nodal brightness, related to BCC
- c: contrast correction field, related to BCC
- c_k: nodal contrast, related to BCC
- $C[\mathbf{v}]$: cross-correlation product, related to DIC
- D_e: number of damaged elements, related to SCD
- δv_i: amplitudes of nodal displacement corrections, related to DIC
- $\boldsymbol{\epsilon}$: strain tensor
- ϵ_1^*: maximum principal strain threshold
- $\bar{\boldsymbol{\epsilon}}$: mean strain tensor
- $\sigma(\bar{\epsilon}_1)$: standard deviation of the maximum principal strain
- E: Young's modulus [Pa]
- $[\mathbf{E}]$: maximum eigen strain by time matrix, related to PCA
- ϕ_c^2: overall gray level residual, related to DIC
- ϕ_m^2: summation of the L2-norm of all equilibrium gaps of the inner nodes, related to MR

- ϕ_t^2: total residual, related to MR and DIC
- ϕ_{bcc}: gray level residuals after BCC, related to BCC
- f: reference image
- $\{\mathbf{f}\}$: vector of nodal forces, related to MR
- $\{\mathbf{f_r}\}$: residual forces, related to MR
- $\{\mathbf{F}\}$: the right-hand side term of the correlation system, related to DIC
- Γ_e: cracked surface, related to AM
- H: specimen height, related to AVE
- hi: hanging node label, related to AM
- $\{\mathbf{h}\}$: residual vector, related to AM
- g: deformed image, related to DIC
- $\widetilde{g}$: corrected deformed image, related to DIC
- $[\mathbf{K}]$: the stiffness matrix, related to MR
- $\mathbf{k}$: wave number of a plane wave, related to MR
- k: constant gain to the refinement threshold, related to AM
- $\{\boldsymbol{\lambda}\}$: the Lagrange multipliers, related to AM
- λ: an eigen value, related to PCA
- ℓ: element size [m or px]
- ℓ_m: regularization length [px], related to MR
- $[\mathbf{L}]$: auxiliary matrix to add the Lagrange terms to the Hessian, related to AM
- $[\mathbf{M}]$: (symmetric semi-definite positive) Hessian, related to DIC
- m: node label, related to PCA

- N: a constant dependent on the contrast in the picture and the noise level, related to AM
- $\mathbf{n}$: normal to the crack face
- n: frame number, related to PCA
- $\nabla \tilde{g}_{\{v\}}(\mathbf{x})$: gradient of the corrected deformed image, related to DIC
- $\nabla f(\mathbf{x})$: gradient of the reference deformed image, related to DIC
- ν_{GR}: number of Hessian elements after global refinement
- ν_{LR}: number of Hessian elements after local refinement
- Ω: part of the image where the displacement field is sought, related to DIC
- $|\Omega_e|$: measure of element e
- ω_m: weight that defines the scale associated with the equilibrium gap, related to MR
- p: element number, related to PCA
- $\mathbf{\Psi}_i(\mathbf{x})$: FE shape function, related to DIC
- $p1i$ and $p2i$: the DOFs of the parent nodes, related to AM
- ρ: polynomial whose roots are the eigen values of $\mathbf{U}$, related to PCA
- $q(\mathbf{x}, f)$: gray level correction field, related to BCC
- $\sigma(\overline{[\![u]\!]})$: displacement jump standard uncertainty, related to AM and MCOD
- $\sigma(\epsilon_1)$: maximum principal strain standard uncertainty, related to AM and MCOD
- $[\mathbf{S}]$: singular values matrix, related to PCA
- s: curvilinear abscissa
- s_i: singular value: related to PCA

- $\{\varsigma\}$: column vector, related to BCC
- t: time [s]
- $[\mathbf{T}]$: modal matrix containing the temporal modes, related to PCA
- $^{\intercal}$: the transpose operator
- $tick$: mold wall thickness, related to AVE
- $\theta_k(\mathbf{x})$: are (scalar) FE shape functions, related to BCC
- $\mathbf{u}$: displacement field, related to DIC
- $[\mathbf{U}]$: displacements by time matrix, related to PCA
- υ_i: unknown degree of freedom, related to DIC
- υ_p^m: measured nodal displacements
- $\overline{[\![\mathbf{u}]\!]}$: displacement jump vector, related to AM and MCOD
- $\overline{[\![u]\!]}$: mean crack opening displacement
- $[\![u^*]\!]$: crack opening displacement threshold, related to AM and MCOD
- $[\mathbf{V}]$: modal matrix containing the spatial modes, related to PCA
- $\mathbf{u^{tot}}$: total displacement field, related to PCA
- $\mathbf{u^{rbm}}$: rigid body motion displacement field, related to PCA
- $\mathbf{u^{mec}}$: mechanical displacement field, related to PCA
- V_0: initial volume of the specimen, related to AVE
- V_i: given volume, related to AVE
- V_e: volume of the specimen after expansion, related to AVE
- $\mathbf{v_0}$: amplitude of a plane wave, related to MR
- $\mathbf{x}$: pixel position
- ζ: ratio of the Frobenius norms of $[\mathbf{M}]$ and

1 INTRODUCTION

Refractory materials are capable of keeping their physical properties (*e.g.,* mechanical and thermal) and functionalities in extreme environments. The refractory castables class corresponds to materials made of aggregates bounded by a cementitious matrix [1]. These materials are used for thermal insulation in the base industry that uses high-temperatures, *i.e.,* the sectors that produce steel, metallic alloys, oil, and glass. For all these examples, the refractory material is generally in contact with corrosive substances at high-temperatures. The development of these materials directly promotes the base industry, for example, by increasing the lifetime of the parts and reducing expenses, which justifies researches in this field. High alumina castables containing magnesia (MgO) may present some advantages. To exemplify, magnesia and alumina (Al_2O_3) react to form spinel phase ($MgAl_2O_4$) *in situ* at temperatures above 1200 ℃. Microstructures containing spinel have high resistance against basic slag and thermal shock damage [2, 3]. The spinel phase can be produced at lower temperatures if fine particles of MgO are added to the castable, since they are more reactive [4–6]. Usually, the raw materials are mixed with water during the processing of the castables. The magnesia in high alumina MgO-containing hydrates spontaneously producing brucite ($Mg(OH)_2$) during them curing and drying steps [7]. The heterogeneous brucite formation promotes a considerable expansion because of the specific volume difference between magnesia (υ_{MgO} = 0.28 cm^3g^{-1}) and brucite ($\upsilon_{Mg(OH)_2}$ = 0.47 cm^3g^{-1}). It is worth noting that the fine MgO particles, which are more efficient for spinel formation, are also efficient for hydration during the process [7]. The expansion during the *in situ* brucite formation acts directly on the mechanical properties of the part. A moderated reaction closes voids increasing the Young's modulus [8], acting as a binder. However, excessive reaction damages the material [7, 9, 10].

The Bar Resonance technique (BR) [11] is commonly used to evaluate variation in Young's modulus and, consequently, the overall damage caused by the MgO hydration during curing and drying of refractory castables containing MgO [7,

9, 10, 12]. Another well known procedure is the Impulse Excitation Technique (IET) [13], which has been applied to measure the damping caused by microstructural modifications of refractory castables after thermal shock damage [14], and the Young's modulus of alumina castables [15].

Another way to quantify damage is via Digital Image Correlation (DIC), a full-field measurement technique that can be applied to the MgO hydration case to understand the crack network formation. DIC provides displacement and strain *fields* to quantify damage [16]. Also, it does not require mechanical contact with the specimen, allowing the latter to be kept in a climatic chamber during the entire test [17].

DIC can be briefly described by the registration of the pixel gray levels of a reference image and other images acquired at different instants, in which the specimen configuration has changed by the effect of loadings (*e.g.,* those induced by heterogeneous expansion due to MgO hydration in the present case). DIC was carried out using the Correli 3.0 code [18] that maps displacement fields of regions in the images. For DIC to perform well, pixels with a random distribution of gray values are necessary, which are usually obtained by speckling paint on the specimen surface. Sometimes, it is possible to use the original surface texture of the material. In global DIC, the displacement fields are discretized using a finite element mesh. Each element contains a group of pixels and the correlation algorithm computes the nodal displacements, which can be used to calculate strain fields.

The use of DIC has contributed significantly to the analysis of mechanical experiments by increasing the gathered amount of information. When applied to mechanical tests, 2D-DIC (*i.e.,* using only one camera) provides planar strain fields, whose analysis permits, for instance, the evaluation of the Poisson's ratio during the entire loading and estimates of the volumetric strain for isotropic materials [16]. DIC can be used to calibrate or validate material models when combined with mechanical tests that induce non-uniform strain states [19]. Moreover, the technique is able to compare many material points submitted to different strain states in one single specimen (*e.g.,* displacement and strain fields during

processing or in the work-life of ceramic materials). The technique has been used in many fields of mechanical, civil, and materials engineering. However, applying DIC during the processing of materials is still a field to be explored.

Correli 3.0 [18] is the software that has been used to apply DIC to advanced experiments. It is being developed at the *Laboratoire de Mécanique et Technologie* (LMT) of *École Normale Supérieure Paris-Saclay* by François Hild and collaborators. The software (and the previous versions) has been used at DEMa - UFSCar by the research group of Rodrigo B. Canto for conventional and non-conventional mechanical tests (*e.g.,* tensile and compression tests of layered composites with polymeric matrix [20–22], in uniaxial tension [23, 24], compression [25], fracture [26], visco-elastic materials [27], and sintering processes [28], for polymeric materials [29], simple compression and Brazilian tests for metallic powder green compacts [30, 31]; fracture analysis by the wedge splitting test on refractory materials [32–34].

DIC has already been applied to characterize refractory materials at laboratory scales [35, 36] to determine crack initiation [37], to study drying of concretes [38], and to monitor cracks during drying of refractory castables [17] using coarse meshes, which were improved in this doctorate. Applying DIC to measure damage in materials can increase substantially the gathered information as mentioned in a review written by Hild *et al.* [39]. In the sequel, new methodologies are presented to apply DIC *in situ* for studying the MgO hydration keeping the specimens inside a climatic chamber, which contributes to the effort to control the reaction and profit from the binder effect that occurs before damage initiation. The main challenge is to reduce the size of the elements in DIC analyses to improve the detection of very small cracks. However, the use of a fine mesh also makes the DIC results more sensitive to noise. In this context, the tasks completed during this doctorate are described as follows. A climatic chamber from previous studies [17] was improved to reduce water condensation on the windows, and to allow for the acquisition of images of two faces of the sample. New molds were crafted to diminish the influence from the molding process and also to study cubic specimens that ensure a representative volume element (considering the size of

aggregates).

Real life experimental conditions are very complex, and most of the time, scientists and engineers cannot control all experimental variables to create a perfect environment where experiments are carried out. DIC experiments usually involve lighting fluctuations that generate noise in the results. One new feature of Correli 3.0 [18] is the Brightness and Contrast Corrections (BCC). The effect of different BCCs was studied to overcome the uncertainties caused by lighting changes. Further, by applying PCA to DIC results, more information can be provided than the well-known denoising effect. For example obtaining the spatial and the temporal modes makes it possible to follow the kinetics of a damaging hydration reaction by means of kinematic analyses. The most interesting contribution is that the information about the crack network development is provided by an algebraic procedure, the PCA, and no inferences are made about what should be considered a crack or not. The first spatial mode shows that the crack opening field is the most relevant cause of displacement when the fluctuations due to rigid body motions are discarded. The first temporal is used to follow the kinetics of the underlying reaction.

Finally, an adapted mesh optimized for the present cases was developed to reduce the computational cost. The numerical procedures to deal with the hanging nodes in the proposed adaptive meshing use Lagrange multipliers in the DIC scheme. The locally refined meshes are compared with their analog uniform mesh (UM) with the smallest element size to study the computational cost reduction. There was a discrete but satisfactory gain for the present case, where the crack network diffuses on the surface. However, this procedure has great potential to reduce the computational requirement for single crack experiments. Also, it can bring good advantages if applied to Digital Volume Correlation.

2 BIBLIOGRAPHIC REVIEW

2.1 Refractory castables

Refractory materials are capable of keeping their properties (*e.g.,* mechanical, chemical, and physical) in functional levels when submitted to aggressive environments [40]. They are technical ceramics composed of large aggregates surrounded by a fine phase called matrix. The main application of this class of materials is the lining of furnaces, boilers, and vessels where they are directly exposed to corrosive substances and high temperatures. Their crucial role in this industry makes refractory ceramics a strategic material for scientific and technological advances [1, 41–43]. There are many processing routes for refractory materials. The raw materials can be transformed by pressing the particles in a preform to produce bricks and valves, for example. This kind of refractories are called shaped, when they are classified by the processing. In contrast, there are the refractory castables that are processed by adding a liquid, generally water, to the particles. They can be monolithic if processed *in situ*, for example, in the furnace lining, or can be cast into parts [1]. The castables installation is fast, practical, and cheaper if compared to shaped parts installations. Besides, their jointless feature dimishes corrosion [1]. This class of refractories has been gaining interest due to the demand of industries of the primary sector: oil, glass, and steel or other alloys. Since the early 20 th century, researchers have been seeking new methods of improving the efficiency of the processes, extend the lifetime of products and enhance the failure predictability, always considering the danger of the processes where refractories are employed [44].

The raw materials used in the formulation of refractory materials (*i.e.,* particles, matrix components, binding agents, and others) are carefully selected to obtain phases and microstructures that are suitable for the desired application. Besides, the formulation also affects processing steps, for example, the mixture, installation, cure, and drying of castables. The last two steps are more time and

energy-consuming than the others. As a consequence, there is interest in reducing the periods of curing and drying to optimize processing routes [45].

Among refractories, the ones containing $MgAl_2O_4$ spinel in their microstructure are of extreme interest for the steel industry because they have high chemical resistance against steel slag [46]. The spinel phase can be added directly to the castable formulation (called pre-formed spinel) or be produced *in situ* by the reaction of alumina and magnesia at high temperatures of $\approx$ 1400 ℃ (called *in situ* spinel). The former started to be added to refractory castable formulations in the later 80s in Japan. Nevertheless, in the next decade, fine MgO particles were added to the formulation of castables to reduce the reaction temperature to 1200 ℃ [12, 46, 47]. The spinel formation is a challenge for the dimensional control of parts because there is an expansion effect due to the difference in the specific volume of the product and the reactants (MgO and Al_2O_3), which is associated with the subject of this thesis. The expansion does not occur in the pre-formed spinel formulations; despite this, the corrosion resistance of the *in situ* spinel is higher than the former, which justifies its demand [48]. The MgO containing formulation is a challenge in itself, because of its fast hydration, which is usually excessive and damages the material. More details about MgO-containing refractories are presented in Section 2.6. On the following sections the concepts that affect the formulation are described.

2.2 Models to optimize the particle size distribution

The term “particulate aggregates” is shorten by “aggregates” in this text. The refractory materials are generally made of a backbone of large aggregates, with the average size reaching the order of centimeters. Their packing is not perfect and creates voids, which are filled by smaller aggregates that compose the matrix [49]. The number of voids in a material, *i.e.,* the packing of aggregates, directly affects the physical properties of the final product, such as mechanical strength, thermal conductivity, permeability and corrosion resistance [50]. About refractory castables, the packing also influences the rheological features of the batch during mixing and casting, the times of curing and drying, and the thermo-

mechanical behavior [51, 52]. It is then evident the importance of characterizing the size distribution of the raw materials. The granulometric fractions may assume a monodispersion where all particles have approximately the same size or a polydispersion with a variety of sizes [53]. Polydispersions can be generated by mixing many monodispersions. The mixture of fractions is beneficial because it increases the packing and, consequently, the density of the final part. The strategy of optimizing the particle size distribution can be described by choosing the proportion and the size of each fraction step by step. First, the larger particles create large voids. Then they are filled by smaller particles that generates smaller voids to be filled by even smaller particles. The steps are repeated successively until the desired packing is achieved [49]. For refractory castables, many granulometric fractions with a variety of size ranges are combined. The choice of the fraction and its proportion is assisted by mathematical models, of which the most popular are the models by Furnas, Andreasen, and Alfred [53, 54].

Furnas [55] proposed an approach based on discrete fractions (monodispertions) and on the assumption that the best packing can be obtained when the smaller aggregates fit into the voids generated by the larger ones. However, monodispertions are extremely difficult to obtain due to technical limitations, and the real ones are very narrow polydispersion fractions. This technical obstacle compromised the application of this model. Nevertheless, it was the inspiration for the following models.

The Andreasen [54] model aims to optimize the packing considering the size relation between different fractions as:

$$\frac{CPFT}{100} = \left(\frac{D}{D_M}\right)^q \tag{2.1}$$

where $CPFT$ means Cumulative Percent Finer Than (wt.%) the size D, D_M is the larger size of aggregates, and q is the packing module, which expresses the ratio between coarse and fine aggregates, *i.e.,* a high q means more coarse aggregates than fine ones [54]. Dinger and Funk [53] revisited Furnas' model employing a rigorous mathematical treatment. They proposed a more realistic model

nominated Alfred's model in praise of the University they worked, which takes into account polydispersion fractions:

$$\frac{CPFT}{100} = \left(\frac{D^q - D_m^q}{D_M^q - D_m^q} \right) \tag{2.2}$$

where D_m is the size of the smallest aggregate. All these models with increasingly robustness improves the final packing efficiency [56].

The above mathematical models help improving the packing optimization. However, they have some limitations, for example, they do not consider the morphology of the aggregates, the friction among them, their inherent porosity, and the formation of agglomerates of fractions with $D < 100$ µm. These limitations represent the distance between theoretical prediction and experimental results [57, 58]. Ortega *et al.* [59] highlighted the consolidation effect (*i.e.,* rigidity due to capillarity forces), which must be considered because of the presence of water in the process. The water is crucial in the castable casting, and it is liberated during the drying and sintering of the part, which affects the final porosity. Besides that, the authors observed that formulations using smaller aggregates are close to theoretical prediction.

The matrix of castables is formed by fine fractions with $D \leq 100\mu m$, whereas fractions with larger particles are denominated coarse aggregates [60]. The assemble of fine aggregates in the vicinity of the coarse ones is disorganized due to the high diversity of sizes, which creates a phenomenon called wall effect. It is the cause of poor packing and the appearance of voids around the coarse aggregates, resulting in a porous region denoted as Interfacial Transition Zone (ITZ) [50, 61, 62]. The presence of these defects is directly related to the proportion between coarse and fine aggregates. To exemplify, a formulation with $\frac{D_M}{D_m} > 10$ diminishes the wall effect and produces a dense refractory part, hence, a formulation with $\frac{D_M}{D_m} < 10$ generates a material with defects, which are not necessarily bad, because these defects can act as ducts, increasing the castable permeability, and permitting that the part be submitted to a faster drying protocol. Thus, the ITZ is a source of defects in the material that can affect the crack network during

the curing and drying of refractory castables.

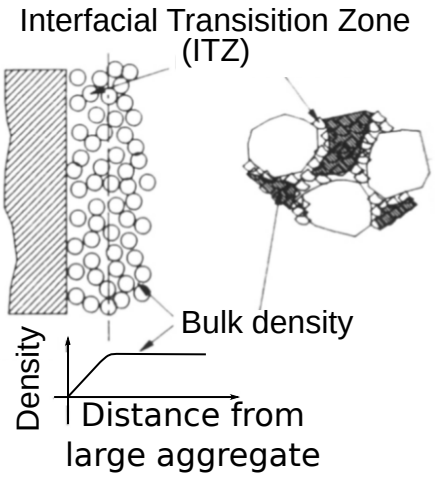

Figure 2.1: Illustration of the ITZ for the packing of aggregates with different sizes. Adapted from Roy *et al.* [62]

2.3 Rheological behavior

Refractory castables can be cast in a unique part with a specific shape, or they can be applied *in situ*. For the later, they are pumped and pneumatically "shot" onto the installation surface. These examples depict the relevance of rheological behavior. A liquid, generally water, is added to the solid fractions during the castable preparation. The liquid is evaporated during the drying and firing of the castable, producing voids in the final product. One of the castable industry challenges is to reduce the water content without compromising the castable fluidity that is required for the application. Fine and superfine aggregates can act as "lubricants" improving the yielding of the coarse ones, which is a strategy to overcome the mentioned challenge [57, 63–66]. The castables can be classified by their rheological behavior in self-flowing and vibratable. The later demands mechanical vibration during the casting. Following Andreasen's model, formulation with $q < 0.26$ generates self-molding castables, whereas $0.26 < q < 0.30$ produces vibratable ones [64].

2.4 Effect of hydraulic binders on the curing of refractory castables

Binders are additives that promote mechanical strength to the castables during the curing. They can be classified according to the mechanism that generates the binding effect, *e.g.,* hydraulic, chemical, coagulating, and sol-gel. The mechanism of hydraulic binders is the hydration of the components, and is the chosen class for the present work. They are the hydratable alumina (HA) [67] and, despite the damage caused by the excessive hydration, the magnesia. The hydraulic binder HA is commonly used in the industry. Its hydration generates a thick layer of Al_2O_3 gel, which not only links coarse and fine aggregates by filling the voids among them, but also generates sufficient green mechanical strength [68]. Special care is required because of the hydrates produced by this class of binders, mainly during the drying of the castable. This care is due to the amount of water released by the decomposition of the hydrates, which can cause the spalling of the part [69, 70].

The kinetic of hydration can be evaluated by diverse techniques. Among them, the Ultrasonic Wave Propagation (UWP) and the Termogavimetric Analyses (TGA) are highlighted. The UWP is based on the propagation velocity of the ultrasonic wave inside the material, which is related to its mechanical properties, *i.e.,* the material cohesion (or its rigidity) is related to faster propagation. This technique has been employed to study refractory castables, because it can be applied from the fluid batch (few moments after casting) until the end of the curing step, and also, because it can identify possible voids generated [71–73]. The castable is cast in special molds, generally made of silicone and equipped with supports for the transducers of the UWP device.

An example of the velocity evolution of the waves in a high alumina castable, and the division of the three steps of the binding effect are shown in Figure 2.2.

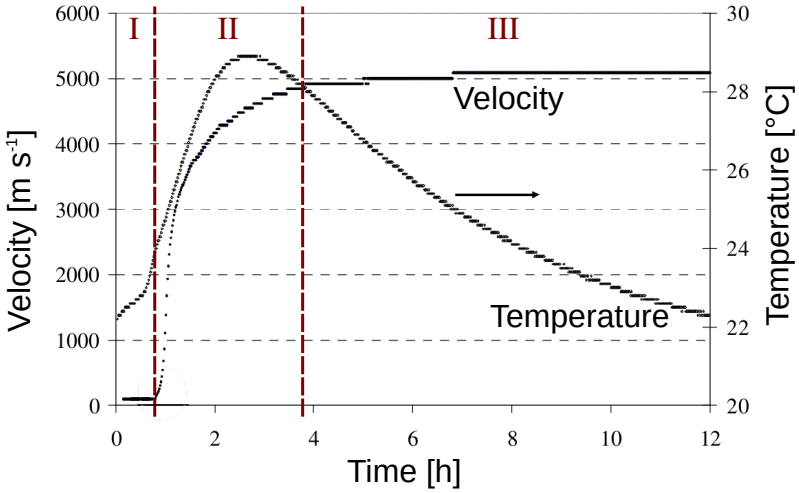

Figure 2.2: Ultrasound wave propagation velocity during the curing of a castable. Three stages indicate significant changes in the material cohesion. Adapted from Simonin *et al.* [72]

The three stages are:

I. contains the effects of the aqueous phase and ultra-fine particles, which is characterized by a low and constant velocity attributed to the discontinuous medium;

II. represents the castable percolation by hydrates formation, in this stage the wave propagation velocity increase quickly;

III. a plateau of velocity that signs the end of the hydration reaction [72].

The excessive hydration of the binder can damage the material and decrease the velocity (in stage III) due to the formation of voids.

In the TGA technique, the sample mass is monitored during a heating program. In this context, the technique is usually used in the study of hydraulic binders to evaluate the amount of water released to the ambient, and it can also distinguish between the adsorbed water and the one chemically bonded to the material by using the releasing temperatures. Nevertheless, TGA can be used to program the drying protocol of refractory castables [74, 75].

2.5 Drying of refractory castables

Vaporization is the extraction of a liquid from a material. It depends on the pressure, the concentration of liquid in the ambient and the temperature. However, if the liquid is water, the process is called drying [76]. This process can be divided into three steps:

1. the water present in the surface of the castable is removed, depending on the temperature and relative air humidity for constant pressure;
2. capillarity forces promote the transportation of water from the center of the material to its surface, which is constant while the amount of water in the material and in the ambient do not achieve an equilibrium [75];
3. with the increase of temperature, the water passes from liquid to steam at $\approx$ 100 ℃.

If there is no open channels for the steam to diffuse, the pressure inside the material can increase drastically and, if the mechanical strength is surpassed, the phenomenon of spalling can be triggered.

Some strategies are applied to increase the heating rate during the drying (decreasing the time and production costs), for example, polymeric fibers are inserted in the castables or the microstructure is projected to generate open pores for releasing steam, preventing severe damage to the material. The polymers used in the first example are polypropylene and polyethylene terephthalate that decomposes at temperatures between 120 and 170 ℃ and at 200 and 270 ℃, respectively [77, 78].

2.6 Magnesia hydration in refractory castables

The addition of MgO particles is a challenge [79] because its easy hydration produces brucite ($Mg(OH)_2$):

$$MgO + H_2O \rightarrow Mg(OH)_2. \tag{2.3}$$

Usually the magnesia content is restricted to 10 wt.% and the aggregates must have a size of about 40 µm to reduce the reaction rate [41].

Brucite ($Mg(OH)_2$) is a crystalline phase with a specific volume of ≈ 0.42 cm^3g^{-1}, which is larger than the specific volume of its predecessor MgO ≈ 0.28 cm^3g^{-1}, resulting in a volumetric expansion of ≈ 50% [3]. If the localized deformation caused by the hydration induces a stress state that surpasses the strength of the material, cracks are generated during the curing and drying. However, the deformation (*i.e.,* the hydration of MgO) is a result of many factors, such as: the MgO source; its interaction with other components as fibers and binders; and the voids content capable of accommodating the localized expansion [3]. Besides the crack formation, the fraction of MgO also affects the rheology of the castable, because more water is needed, and the time of service is reduced. In fact, MgO is very hygroscopic, *i.e.,* readily adsorbs water from the ambient, promoting the generation of brucite during the curing and drying [3]. Even with the mentioned adversities, if the hydration reactions can be controlled to provide only the expansion necessary to close the voids, without initiating damage, the brucite formation could be used as a binder. In this context, Salomão *et al.* [80] studied the effect of the water content in the hydration of MgO and observed that the formulation with less water and, consequently, fewer pores, presented an Apparent Volumetric Expansion (AVE) greater than the formulation with more water. Nevertheless, it was also shown in [80] that the hydration closes the pores, and the overall expansion can be measured after that. Another example of the search for the hydration control is the study carried out using different MgO particles sources. It was observed that more reactive particles (*i.e.,* nanometric Calcinated Magnesia) generate initially better mechanical properties as quantified by the increase in the Young's modulus (E), followed by an abrupt decrease due to damage. On the other hand, the less reactive particles (*i.e.,* Dead Burnt Magnesia) showed a moderate and stable increase of E [7].

The hydration mechanism has different effects for monocrystalline and polycrystalline MgO. When the former is in contact with water, molecules are ad-

sorbed on the crystal surface and react with the oxide, generating a homogeneous layer of brucite. This layer diminishes the reaction propagation [81]. The reaction causes a conformational change in the crystal, transforming the cubic structure of MgO to the hexagonal structure of $Mg(OH)_2$. In this process, a localized expansion is generated and microcracks can be formed in the brucite layer. This damage allows other water molecules to react with the MgO fraction inside the monocrystal and re-starts the hydration reaction [3]. The commercial grades of MgO are polycrystalline, *i.e.,* aggregates made by many monocrystals. The hydration reaction starts in the grain boundaries because these regions have low atomic packing and high free energy. Therefore, the expansion due to hydration occurs among the grains and separates them. After total separation the reaction follows as described for the monocrystals (Figure 2.3) [3].

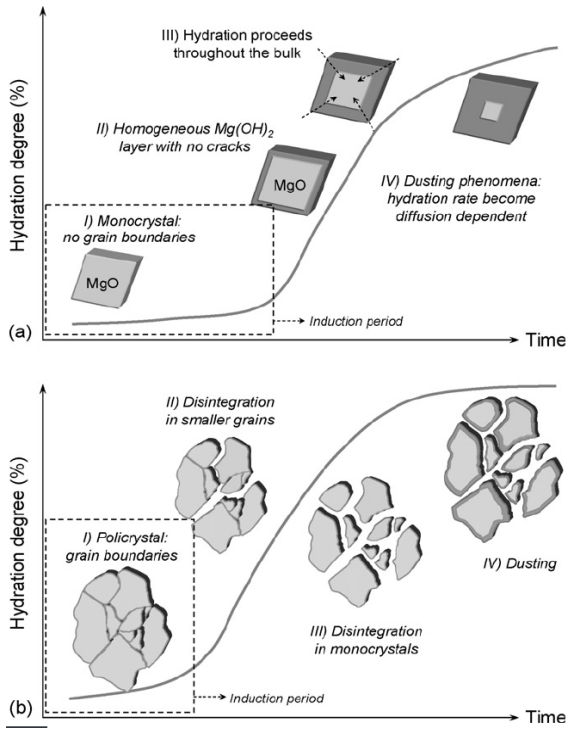

Figure 2.3: Schematics of the MgO hydration and its consequences for a) monocrystals e b) polycrystals. Extracted from Salomão *et al.* [3]

Birchal *et al.* [82] suggested a semi-empirical model to describe the transformation of MgO into $Mg(OH)_2$ at temperatures between 35 and 90 °C. In the model, the conversion rate increases proportionally with temperature as can be

seen in Figure 2.4.

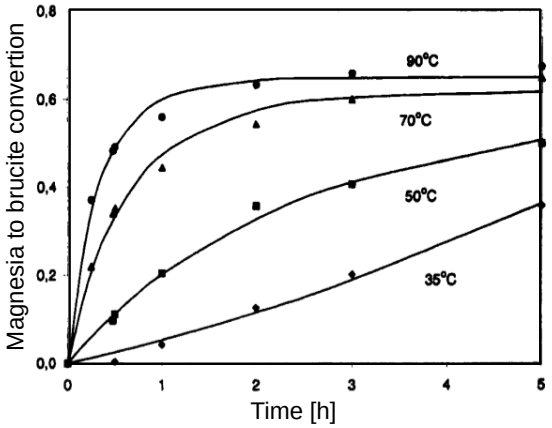

Figure 2.4: MgO hydration kinectis at different temperatures. The dots are experimental data and lines were obtained by applying the model proposed by Birchal *et al.* [82]. Extracted from Birchal *et al.* [82]

Not only external conditions but features of MgO aggregates also directly affect the hydration. MgO can be obtained by the calcination of magnesite, a mineral that contains ≈ 47.6 wt.% of MgO. However, the type of MgO aggregates depends on the calcination temperature [83]:

- from 900 to 1300 ℃, Caustic Magnesia (CM) is formed;
- from 1500 to 1800 ℃, Dead Burnt Magnesia (DBM) is formed;
- above 1800 ℃, Electrically Fused Magnesia is formed.

Higher temperatures generate larger and less reactive particles. The high reactivity of CM is adequate to form the spinel phase at lower temperatures [4]. However, this feature also promotes hydration, which can cause severe damage to the material during processing. In contrast, the electrically fused magnesia reactivity is low and compromises the spinel formation, and this type is not usually used for this purpose. The DBM has moderate reactivity [84].

At the beginning of curing, the castable is fluid enough to accommodate the localized expansion due to the hydration. However, after the binding mechanism ceases, there are few pores remaining to accomplish this function, and

new expansion generates stress that may damage the material [85]. To illustrate that, Souza *et al.* [7] applied the Bar Resonance (BR) technique to evaluate the changes in E during the curing of alumina castables containing MgO and Calcium Aluminate Cements (CAC), because the later increases the green mechanical strength. Four formulations were tested, two of them without CAC but using DBM or CM, and the other two with 6 wt.% CAC and one of the magnesia types. They produced bar-shaped specimens (25×25×150 mm^3) for the BR and cylinders (40×40 mm^2) for splitting compression test (also called Brazilian test [86]) to evaluate the mechanical strength by the rupture limit (σ_f). The results are shown in Figure 2.5.

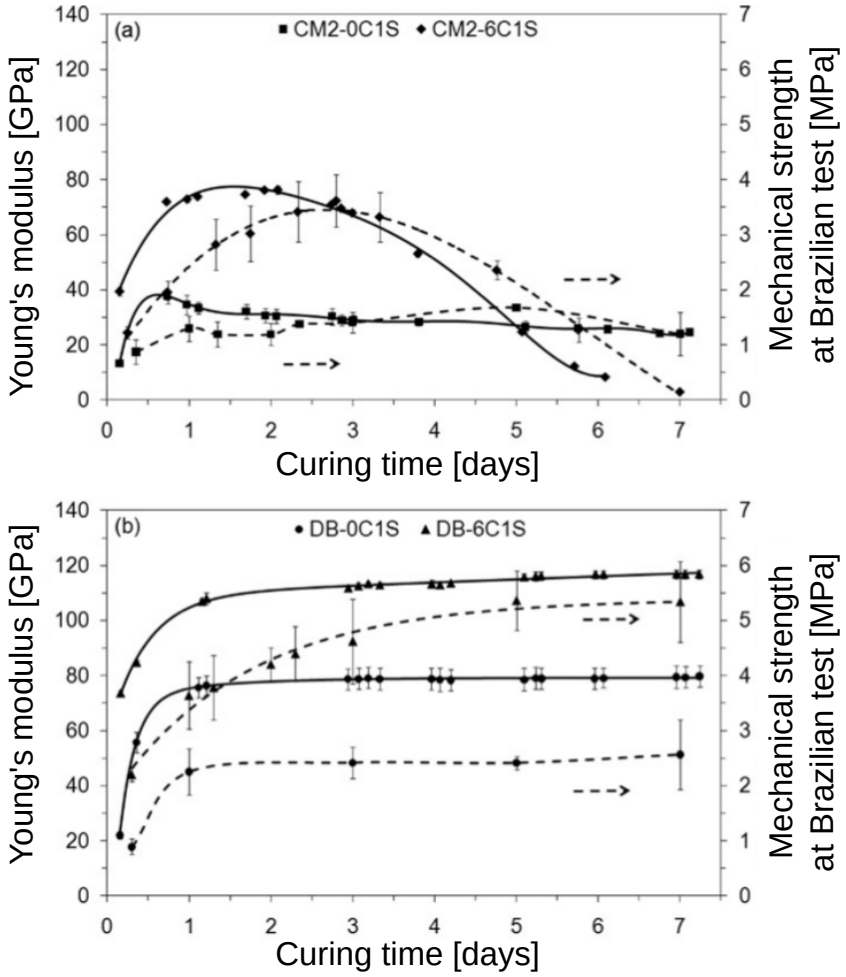

Figure 2.5: Young's modulus obtained by BR and mechanical strangth during Brazilian tests for different formulations: a) CM with and without CAC and b) DBM with and without CAC. Adapted from Souza *et al.* [7]

One can notice a peak in E for formulations containing CM. It is caused by the reactivity of this magnesia type promoting the expansion that closes voids in the early stages (E increases) but also damages the material due to the mentioned excess (E decreases). On the contrary, no damage was detected for the formulation with DBM (low reactivity). The presence of CAC retarded the onset of damage (CM containing formulation), which was related to the improvement of mechanical properties generated by the cement. By comparing the techniques, the authors pointed out that BR is more accurate than the Brazilian test because the former is a nondestructive technique [7].

Salomão *et al.* [3] presented a creative new approach to evaluate the expansion due to hydration of high alumina MgO-containing refractory castables. The batch was cast into thin wall molds with cylindrical shape (70×70 mm^2) made by a special polymer to avoid adhesion of the castable. Also, a thin cut was made in the wall of the mold to reduce displacement constraints (Figure 2.6). The height and diameter of the specimens were measured during 7 days of curing in an environment saturated by vapor, and each specimen was submitted to a different temperature (8, 30, 50, and 80 ℃). The measurements composed what was called Apparent Volumetric Expansion (AVE) expressed by:

$$V_i = \frac{H_i \cdot \pi \cdot (D_i - 2tick)^2}{4} \tag{2.4}$$

$$AVE = 100 \cdot \frac{V_E - V_0}{V_0} \tag{2.5}$$

where, for a given volume V_i, H is the height of the specimen, D is the diameter of the mold and $tick$ is the thickness of the mold wall. V_0 is the initial volume of the specimen and V_E is its volume after expansion. Evidently, the AVE is a global measurement of the specimen volumetric expansion. The authors used high alumina refractory castables containing 6 wt.% of DBM and 5.5 wt.% of water. The mixture was cast under vibration. They also produced cylinders for Brazilian tests (40×40 mm^2) to measure the fracture stress [3]. The results are depicted in Figure 2.7.

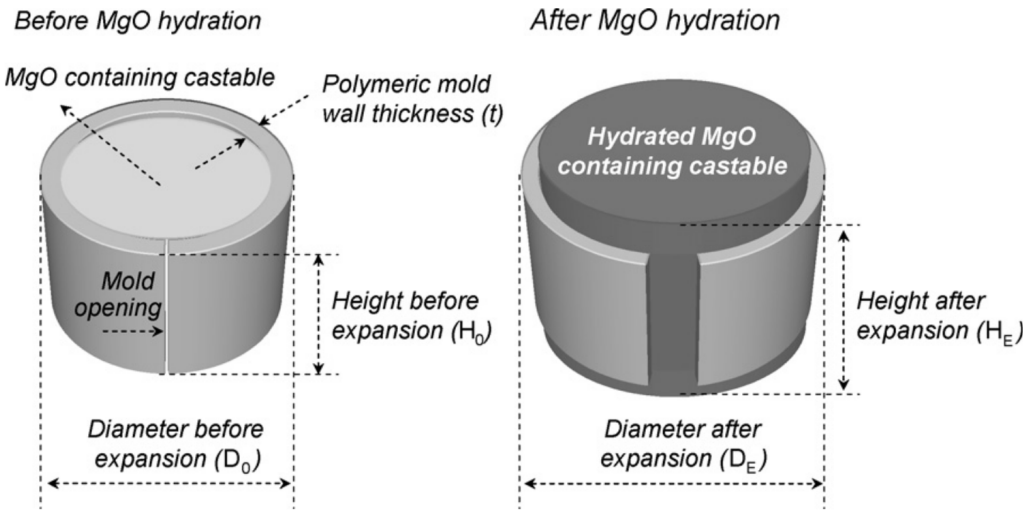

Figure 2.6: Schematics of the experimental procedure to evaluate AVE. Adapted from Salomão *et al.* [3]

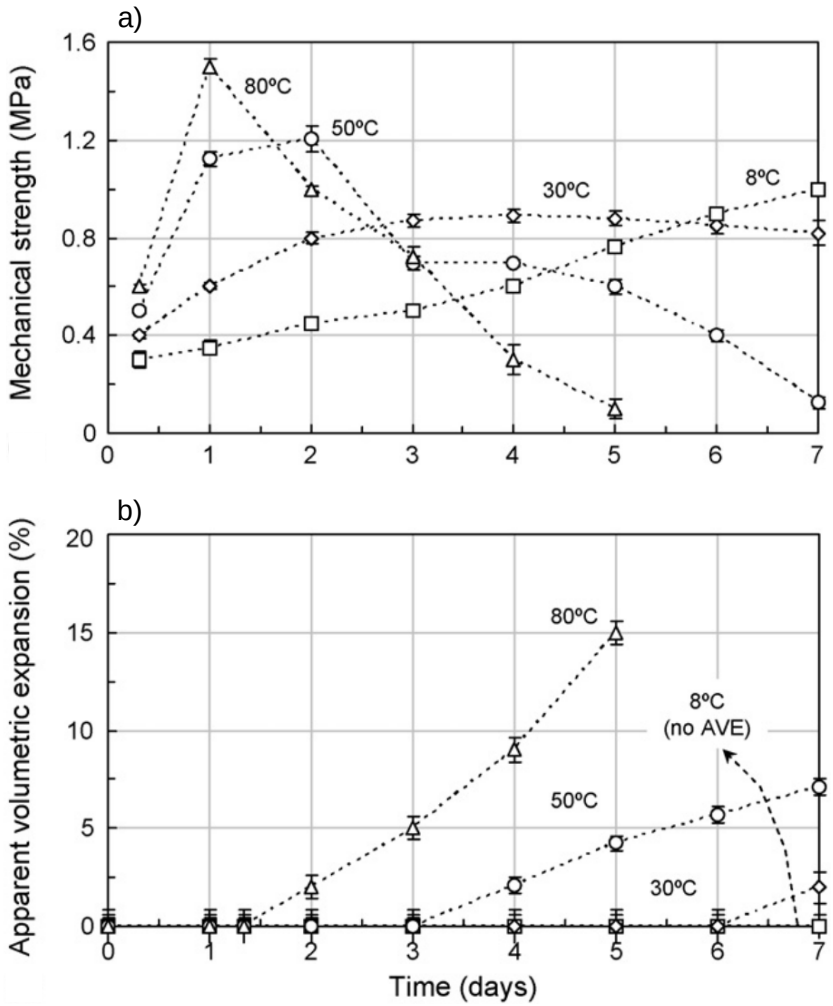

Figure 2.7: MgO hydration effects on the high-alumina refractory castables during the curing: a) AVE and b) Mechanical strength during Brazilian test. Extracted from Salomão *et al.* [3]

The results for tests carried out at 50 and 80 ℃ show that there is a match between the increase of AVE and the decrease in the fracture stress values, indicating that the damage was caused by the expansion (or hydration). For the test at 8 ℃, there was no AVE registered and a slow increase of fracture stress, which points out that the expansion was closing voids during the period of measurement. Also, the test carried out at 30 ℃ showed a slight decrease in σ_f and a moderate increase of AVE [3]. This methodology to measure the global expansion (represented by AVE) could be brought to the light of full-field analysis by using DIC, that allows access to localized phenomena (e.g. cracks) and to better comprehend the fracture mechanisms and kinetics.

2.7 Digital Image Corrrelation (DIC)

DIC is a full-field technique used to measure displacements that can be applied to images scaled from nanometers to kilometers for the pixel size. This range only depends on the device used to acquire the images [16]. The displacement fields between material points are measured on the surface of interest, and they can be used to calculate strain fields. The gathered amount of information is larger than that obtained by traditional extensometry [87]. In the context of this thesis, the technique has been applied to analyze the development of crack networks [17, 32, 88–91].

The material points present relative displacements when the specimen is submitted to mechanical loads [92], or when physicochemical reactions promote deformations, as in the context of this thesis. A reference image f acquired before loading is compared with another of the specimen in a deformed state g. Both images are represented by a matrix of gray levels. DIC is based on the assumption that the gray levels of every pixel at position $\mathbf{x}$ in the reference image f are identical in the image g, but displaced by $\mathbf{u}$

$$f(\mathbf{x}) = g(\mathbf{x} + \mathbf{u}(\mathbf{x})). \tag{2.6}$$

The area of interest Ω is the part of the image where the displacement field is

sought. Applying the L2-norm to estimate the difference between images yields

$$\phi_c^2 = \sum_{\Omega} \left[f(\mathbf{x}) - g(\mathbf{x} + \mathbf{u}(\mathbf{x})) \right]^2 . \tag{2.7}$$

where ϕ_c^2 is the overall gray level residual. By using this methodology, the measured displacements are obtained as

$$\{\boldsymbol{v}_{\text{DIC}}\} = \arg\min_{\{\boldsymbol{v}\}} \phi^2(\{\boldsymbol{v}\}). \tag{2.8}$$

Different pixels can assume the same gray level, meaning that many solutions for the above system are possible. It can be classified as an ill-posed problem [93]. Two methodologies can be used to improve the conditioning of the system, namely, local and global approaches. Dealing with noisy images, the former is not as efficient as the latter [94]. Another advantage of global DIC is the possibility to integrate DIC with numerical simulations and analytical solutions [32, 34, 95]. Hereafter, these differences are highlighted.

Local DIC

In local DIC, the ROI is partitioned into small subgroups of pixels called Zones of Interest (ZOI), and the displacement $\mathbf{u}$ is measured at the center of each ZOI by, for instance, the maximization of the cross-correlation product to reduce the gray level differences [96–99]

$$\mathbf{u}_{\text{DIC}} = \arg\max_{\mathbf{v}} C[\mathbf{v}] \tag{2.9}$$

with

$$C(\mathbf{v}) = \sum_{ZOI} f(\mathbf{x}) g(\mathbf{x} + \mathbf{v}). \tag{2.10}$$

In this local analysis, the mean displacement is the only quantity that is kept [99]. The latter has the least uncertainty of any displacement interpolation within the ZOI [94].

The Zero-Normalized Cross-Correlation (ZNCC) is a way to overcome local

brightness and contrast variations [100]. The images are normalized by subtracting the mean brightness of the considered ZOI, and dividing by the corresponding standard deviation

$$\overline{f}(\mathbf{x}) = \frac{f(\mathbf{x}) - \langle f \rangle_{\mathrm{ZOI}}}{\sqrt{\langle (f - \langle f \rangle_{\mathrm{ZOI}})^2 \rangle_{\mathrm{ZOI}}}}. \tag{2.11}$$

The same correction is performed on g. To summarize, this correction considers $f \approx \overline{f}(\mathbf{x})$ and $g \approx \overline{g}(\mathbf{x})$ in Equation (2.10).

Global DIC

Global DIC consists in performing the analysis over the whole ROI (and not subdividing it into small interrogation windows). The first propositions were based upon spectral decompositions of the displacement field [101, 102]. Then, FE discretizations were considered [87, 103, 104]. The sought displacement field is written as

$$\mathbf{v}(\mathbf{x}) = \sum_i \upsilon_i \mathbf{\Psi}_i(\mathbf{x}), \tag{2.12}$$

where $\mathbf{\Psi}_i(\mathbf{x})$ are FE shape functions, and υ_i nodal displacements. In this thesis, 3-noded triangular element meshes were used to carry out DIC analyses [105].

The deformed image corrected by such displacement fields becomes

$$\widetilde{g}_{\{\upsilon\}}(\mathbf{x}) = g(\mathbf{x} + \sum_i \upsilon_i \mathbf{\Psi}_i(\mathbf{x})) \tag{2.13}$$

where the column vector $\{\boldsymbol{\upsilon}\}$ gathers all nodal displacements υ_i. In global DIC, the gray level differences are globally minimized over the ROI, that is

$$T_g(\{\boldsymbol{\upsilon}\}) = \|\widetilde{g}_{\{\boldsymbol{\upsilon}\}}(\mathbf{x}) - f(\mathbf{x})\|^2_{\mathrm{ROI}} \tag{2.14}$$

such that the sought displacement is the argument that minimizes $T_g(\{\boldsymbol{\upsilon}\})$

$$\{\boldsymbol{\upsilon}\}_{\mathrm{DIC}} = \arg\min_{\{\boldsymbol{\upsilon}\}} T(\{\boldsymbol{\upsilon}\}). \tag{2.15}$$

Equation (2.15) corresponds to a nonlinear least squares minimization. For instance, a Gauss-Newton scheme can be selected. Let us then consider small

amplitudes of nodal displacement corrections δv_i, and a 1^{st} order Taylor expansion of $\widetilde{g}$ with respect to the current estimate of the nodal displacements $\{\boldsymbol{v}\}$

$$\begin{aligned} \tilde{g}_{\{v\}}(\mathbf{x}+\delta v_i \boldsymbol{\Psi}_i(\mathbf{x})) &= \tilde{g}_{\{v\}}(\mathbf{x}) + \boldsymbol{\nabla}\tilde{g}_{\{v\}}(\mathbf{x})\cdot\boldsymbol{\Psi}_i(\mathbf{x})\delta v_i \qquad (2.16)\\ &\approx \tilde{g}_{\{v\}}(\mathbf{x}) + \boldsymbol{\nabla} f(\mathbf{x})\cdot\boldsymbol{\Psi}_i(\mathbf{x})\delta v_i \qquad (2.17)\end{aligned}$$

where the additional assumption $\boldsymbol{\nabla}\tilde{g}_{\{v\}}(\mathbf{x}) \approx \boldsymbol{\nabla} f(\mathbf{x})$ was used to perform this calculation once for all and not at each iteration. With such linearization, the approximated least squares functional is quadratic in terms of displacement corrections. Its minimization then leads to a linear system

$$[\mathbf{M}]\{\delta v\} = \{\mathbf{F}\}, \qquad (2.18)$$

where $[\mathbf{M}]$ is the (symmetric semi-definite positive) Hessian, and $\{\mathbf{F}\}$ the right-hand side term, whose components read

$$\begin{aligned} M_{ij} &= \sum_{\mathrm{ROI}} \left(\nabla f(\mathbf{x})\cdot\boldsymbol{\Psi}_i(\mathbf{x})\right)\left(\nabla f(\mathbf{x})\cdot\boldsymbol{\Psi}_j(\mathbf{x})\right),\\ F_i &= \sum_{\mathrm{ROI}} \left(\nabla f(\mathbf{x})\cdot\boldsymbol{\Psi}_i(\mathbf{x})\right)\ \rho_{\{v\}}(\mathbf{x}), \qquad (2.19)\end{aligned}$$

with

$$\rho_{\{v\}}(\mathbf{x}) = f(\mathbf{x}) - \tilde{g}_{\{v\}}(\mathbf{x}). \qquad (2.20)$$

the gray level residuals associated with the current estimate of the nodal displacements $\{\boldsymbol{v}\}$.

When iteratively solving system of equations (2.18), the nodal displacements and the corrected image are updated. The procedure continues until a convergence criterion is reached, namely, when the maximum amplitude of the nodal displacement corrections becomes less than a selected threshold (*i.e.,* 10^{-4} px in the present cases).

DIC is not restricted to traditional FE discretization. It is also possible to disconnect nodes of the mesh on the crack path, if it is known (*e.g.,* using the

gray level residuals [106]), enrich the kinematics [107], or employ analytical solutions [108], whose amplitudes v_i are replaced by a group of parameters that describes a constitutive model [32, 91, 108]. Numerical simulations can also be used instead [109, 110]. DIC can also be regularized by a mechanical model via so-called Mechanical Regularization (MR) [111, 112]). This procedure provides a more refined discretization with no increase of measurement uncertainties [109, 111, 112]. For instance, elastic regularization highlights cracks since they are not accounted for in the model [39].

DIC has already been used by Saracura [17, 113] to study the damage caused by MgO hydration, without MR or other procedures to overcome experimental challenges that are described in this thesis. Saracura used specimens with dimensions $25 \times 25 \times 150$ mm^3 to apply the BR method and DIC. The author compared the results of both techniques showing that the decrease in Young's modulus E (BR) coincided with the increase in the superficial crack density (determined via DIC) [17, 113]. However, the selected dimensions did not result in a Representative Volume Element (RVE) (*i.e.,* the smallest edge should be at least 10 times the size of larger heterogeneities) facing the size of the larger aggregates (*i.e.,* 6 mm).

2.8 Mechanical Regularization (MR)

One of the many advantages of using FE-DIC is the possibility to apply the equilibrium gap method as a way to enforce mechanical admissibility [112, 114]. Let us assume that the linear elastic law applies to the system being evaluated. Then, the equilibrium equations are

$$[\mathbf{K}]\{\mathbf{u}\} = \{\mathbf{f}\}, \tag{2.21}$$

where [**K**] is the stiffness matrix, and $\{\mathbf{f}\}$ the vector of nodal forces. If the displacement field $\mathbf{u}$ does not satisfy equilibrium, force residuals $\{\mathbf{f_r}\}$ arise

$$\{\mathbf{f_r}\} = [\mathbf{K}]\{\mathbf{u}\} - \{\mathbf{f}\}. \tag{2.22}$$

In the absence of body forces, the nodal forces of inner nodes must vanish, which makes the goal of the equilibrium gap approach the minimization of

$$\phi_m^2 = \{\mathbf{u}\}^\intercal[\mathbf{K}]^\intercal[\mathbf{K}]\{\mathbf{u}\}, \tag{2.23}$$

where $^\intercal$ is the transpose operator, and ϕ_m^2 the summation of the L2-norm of all equilibrium gaps of the inner nodes.

To minimize simultaneously the correlation residuals ϕ_c^2 and the equilibrium gap ϕ_m^2, a total cost function is written

$$(1+\omega_m)\phi_t^2 = \tilde{\phi_c^2} + \omega_m\tilde{\phi_m^2}, \tag{2.24}$$

where ω_m is the weight that defines the scale associated with the equilibrium gap, ϕ_t^2 the total residual, $\tilde{\phi_c^2}$ and $\tilde{\phi_m^2}$ normalized residuals. The importance of normalization is to convert the residuals into dimensionless quantities [115]. It is carried out by considering a trial displacement field in the form of a plane wave $\mathbf{v}(\mathbf{x}) = \mathbf{v_0}\exp(i\mathbf{k}\cdot\mathbf{x})$, where $\mathbf{v_0}$ is the amplitude and $\mathbf{k}$ the wave vector. The normalized residuals become

$$\tilde{\phi_c^2} = \frac{\phi_c^2}{\{\mathbf{v}\}^\intercal[\mathbf{M}]\{\mathbf{v}\}} \quad , \quad \tilde{\phi_m^2} = \frac{\phi_c^2}{\{\mathbf{v}\}^\intercal[\mathbf{K}]^\intercal[\mathbf{K}]\{\mathbf{v}\}}. \tag{2.25}$$

The wavelength dependence of $\{\mathbf{v}\}^\intercal[\mathbf{K}]^\intercal[\mathbf{K}]\{\mathbf{v}\}$ is of the fourth-order, and the quantity $\{\mathbf{v}\}^\intercal[\mathbf{M}]\{\mathbf{v}\}$ is independent of $\mathbf{k}$. Tomičević *et al.* [112] defined the weight as

$$\omega_m = (2\pi|\mathbf{k}|\ell_m)^4 \tag{2.26}$$

where ℓ_m is the regularization length for ϕ_m^2. Therefore, the weight put on the MR cost function is higher as ℓ_m raised to the power 4. The value chosen for ℓ_m should be small enough to fit in small ROIs but large enough to avoid discretization artifacts [115]. Specifically for this doctorate, whose objective is to monitor cracks, the value of ℓ_m needs to be as small as possible, otherwise displacement jumps in the crack path are spread over adjacent elements.

2.9 Brightness and Contrast Correction (BCC)

Many phenomena can disturb the optical flow (*i.e.,* changes in gray levels of pixels due to motions). They may be related to lighting of the experiment [93, 99], drifts of electron beams in SEMs [116, 117], and variations of the refractive index caused by temperature gradients between the imaging device and the sample [118]. Various gray level correction procedures have been reported in the literature for local DIC approaches [99]. The (ZNCC) criterion is one of the most popular corrections [100]. For instance, this type of correction was used to investigate crack propagation in rocks [119]. Another known correction is a gray level average to minimize high temperature effects [120]. Gray level corrections were also introduced in global DIC via brightness and contrast *field* changes [93]. Some specific cases used the gray level corrections, for example, DIC analyses of infrared pictures [121, 122], and distortion corrections of infrared lenses [123]. Tests performed at temperatures up to 1860 ℃, for which gray level inversions occurred, can also be monitored via global DIC [124] (Figure 2.8).

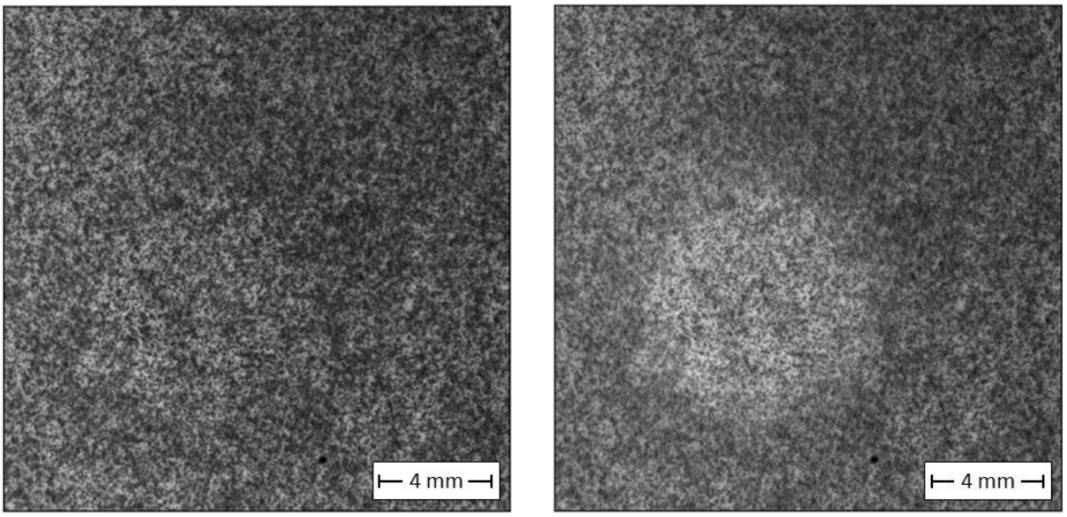

(a) Reference image (b) Image after heating step

Figure 2.8: Change in gray levels due to heating. Adapted from [124]

In the experimental set up utilized in this doctorate, the conservation of gray levels is disturbed by temperature and air humidity (processing conditions) because they alter the refractive index of air [125].

In the above-described procedure, gray level conservation was assumed during optical flow. If such hypothesis is no longer satisfied, the previous residuals $\phi_{c\{v\}}(\mathbf{x})$ can still be lowered in a second step by considering brightness and contrast corrections (with no changes in displacements)

$$\phi_{bcc}(\mathbf{x}) = \phi_{c\{v\}}(\mathbf{x}) + q(\mathbf{x}, f), \tag{2.27}$$

where q(**x**,f) is the gray level correction field that depends on the position $\mathbf{x}$, and the gray levels of f. Polynomial expansions can be considered (*e.g.,* as used for displacement estimations [93, 123]). In this thesis, the first two terms are selected

$$q(\mathbf{x}, f) \approx b(\mathbf{x}) + c(\mathbf{x}) f(\mathbf{x}) \tag{2.28}$$

and correspond to the brightness correction field b, and the contrast correction field c. As for the displacement field, the two correction fields are written as

$$b(\mathbf{x}) = \sum_k b_k \theta_k(\mathbf{x}) \quad \text{and} \quad c(\mathbf{x}) = \sum_k c_k \theta_k(\mathbf{x}), \tag{2.29}$$

where $\theta_k(\mathbf{x})$ are (scalar) FE shape functions, b_k nodal brightness and c_k nodal contrast corrections. The latter ones are obtained by minimizing the L2-norm of ϕ_{bcc} with respect to the column vector $\{\varsigma\}$ gathering all corrections b_k and c_k. In the present case, a standard least squares minimization is performed (*i.e.,* no iterations are needed). From these estimates, a corrected reference image $\hat{f}$ is computed

$$\hat{f}(\mathbf{x}) = b(\mathbf{x}) + (1 + c(\mathbf{x})) f(\mathbf{x}), \tag{2.30}$$

and instead of using f in the first DIC step, the corrected reference image $\hat{f}$ is considered. Therefore, a staggered algorithm is used to minimize $\phi_{bcc}(\mathbf{x})$, namely, first minimizing $\phi_{\{\boldsymbol{v}\}}(\mathbf{x})$ for given gray level corrections, and then $\phi_{bcc}(\mathbf{x})$ at fixed nodal displacements $\phi_{\{\boldsymbol{v}\}}(\mathbf{x})$. These two steps are repeated until final convergence [126].

2.10 Principal Component Analysis (PCA) applied to DIC results

The Singular Value Decomposition (SVD), usually the first step of Principal Component Analysis, is a model order reduction technique. It has been used in modal analysis for dynamic systems [127] and for image denoising [128]. Trebuňa *et al.* [129] applied SVD to displacements obtained by stereo-DIC to find the vibration modes of a piece of paper in front of a speaker. The authors showed a potential methodology to study dynamic systems via DIC and two fast cameras. Grama and Subramanian [130] applied PCAs to horizontal and vertical displacement fields to compute the strain fields from DIC results using synthesized pairs of images to recreate different analytical cases. They proposed the PCA as a tool to reduce dimentionality of the displacement data and mitigate noise. The effectiveness of PCA on noise reduction for DIC displacement fields was also evaluated by Hao *et al.* [131]. The authors used PCA to reduce spurious fluctuations in high-temperature DIC results. The procedure was applied to displacement fields for a synthetic set of images and another using images from a tensile test at high temperature. The displacement fields obtained directly by DIC were compared to the other obtained after the PCA procedure, whose effectiveness was proven.

Passieux and Périé [132] presented a new approach to DIC procedure based on PGD. During PGD, SVD is applied to obtain the modes, and then the correlation problem is solved by summing the best-ranked ones, in each iteration, improving the candidate displacement fields. The results were displacement fields at the pixel scale without the use of a super fine mesh that would be required for traditional FE based DIC (*i.e.,* only 12 points in the vertical and 12 in the horizontal directions were used).

Spacetime DIC registrations of infrared images were conducted with a reduced set of modes constructed via numerical thermomechanical simulations of laser shocks on stainless steal plate [133]. The previous model order reductions were performed a posteriori to extract meaningful modes. An alternative route consists in performing such procedures on the fly corresponding a PGD strategy.

2.11 Adaptive meshing

The design of the mesh is crucial for the Finite Element Method. The application target can be a numerical simulation problem, or FE-DIC described above. In both cases, the user has to base their choices about mesh designing on their experience [134]. To overcome this issue, Babuška and Rheinboldt [134] developed *a-posteriori* error estimate procedures for FE analyses, which give the error in terms of localized quantities. This feature permitted the authors to develop an adaptive optimization of the FE mesh. The objective of an adaptive meshing is to gain control of the discretization error by increasing the number of DOFs in regions where the initial mesh is not adequate [135]. The adaptive refinement of the mesh can be divided into three strategies:

1. h-refinement that subdivides the elements;

2. p-refinement that increases the order of the approximation (*i.e.,* the shape functions);

3. hp-refinement that is a combination of both.

The p-refinement is easier to implement since it does not affect the mesh connectivity. This procedure has already been used for DIC [136], increasing the resolution without reducing the element size. Kleinendorst *et al.* [137] also implemented p-refined DIC using special shape functions called Non Uniform Rational Basis Spline (NURBS). NURBS permit that nodes have different connectivities, thereby forming what is called T-joints [138]. Further, NURBS need less iterations than the Legendre polynomials to perform well [137].

During a localized h-refinement, some nodes located in the middle of an edge between two elements (*e.g.,* one subdivide and others not), can present different numbers of connectivities. To illustrate it, let us consider a structured mesh with 2 triangular elements (Figure 2.9(a)).

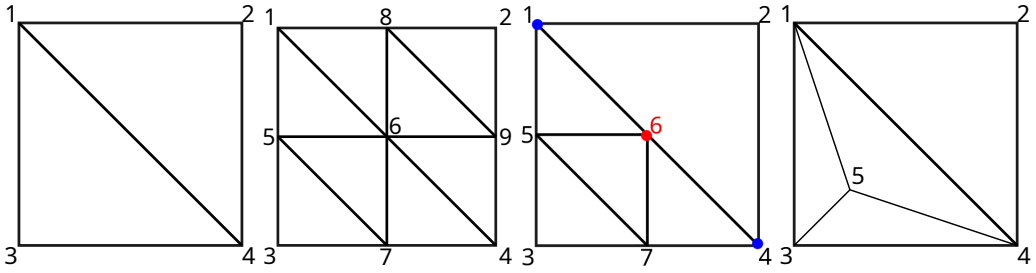

(a) original mesh (b) global h-refinement (c) localized h-refinement non-conformal mesh (d) localized h-refinement conformal mesh

Figure 2.9: Examples of mesh refinement of type h.

If each element is divided into 4 new elements of the same size, the result is shown in Figure 2.9(b). However, if only the element 143 is subdivided into 4 new ones, it will generate one hanging node (node 6 in Figure 2.9(c)), which does not have the correct number of connectivities. For localized h-refinement, at least one node is created on the edge that separates the subdivided domain and the initial one. The presence of hanging nodes makes the mesh non-conformal, which may induce numerical artifacts (especially in DIC).

An apparent easy alternative to overcome the hanging nodes is to divide the elements creating a new node in the centroid and connecting it to the element vertices (Figure 2.9(c)). However, this approach generates slender elements that compromise the calculations [139]. To overcome this drawback, Baldi and Bertolino [139] reconstructed the mesh. Although this strategy goes against the goal of mesh refinement that tries to increase the Degrees of Freedom (DOFs) and increasing as less as possible the computational cost. An alternative solution is proposed in this thesis, which uses Lagrange multipliers to prescribe the displacement of hanging nodes based on the displacement of the adjacent (also called parent) nodes [140].

3 MATERIALS AND METHODS

3.1 Materials

The studied material is a high-alumina refractory castables containing 6 wt.% of caustic magnesia (98 wt.% MgO, $d_{90} < 33$ µm, RHI-Magnesita, Brazil), and high specific surface area, were formulated following the Alfred packing model with q = 0.26 using tabular (Almatis, Germany) and reactive (CL370 and CT3000SG) aluminas as raw materials. A polycarboxylate ether-based dispersing agent was added (Castament® FS60, BASF, Germany), and water was adjusted to provide 80% of initial flow under vibration [141]. The Al_2O_3-MgO castable formulation used in this study is summarized in Table 3.1.

Table 3.1: Composition of the studied Al_2O_3-MgO based castables

Raw materials	[wt.%]
Tabular alumina ($d \leq$ 6 mm)	81
Tabular alumina ($d < 45$ µm)	6
Reactive alumina (CL370)	2
Reactive alumina (CT3000SG)	5
Caustic magnesia (SA = 24.57 m^2g^{-1})	6

Water 5.1 wt.% and dispersant 0.2 wt% of the total weight.

3.2 Specimen production

The composition was prepared in a castable rheometer and homogenized for 10 min. The resulting mix was cast under vibration into silicone molds with internal dimensions of 150 × 25 × 25 mm^3 (Figure 3.1(a)), a typical size for IET specimens, and 70 × 70 × 70 mm^3 for the cubic samples (Figure 3.1(b)). The edge size of the cubes (70 mm) was chosen because it is more than ten times the average diameter of the largest aggregates (≈ 6 mm) to provide a representative volume element (RVE). The flexibility of the silicone helps the demolding process without the need of a release agent. After casting, the specimens and the mold were stored in an in-house developed climatic chamber (see Section 4.1 on page 49), where the image acquisitions were carried out. The specimens were demolded

after three hours at 50 ℃ and 50% relative air humidity. They were subsequently prepared to provide a wide variety of gray levels for the DIC procedure, namely, two perpendicular faces of the cubic specimens and one face of the bar-shaped samples were speckled with black paint as the castable has a light and mat hue.

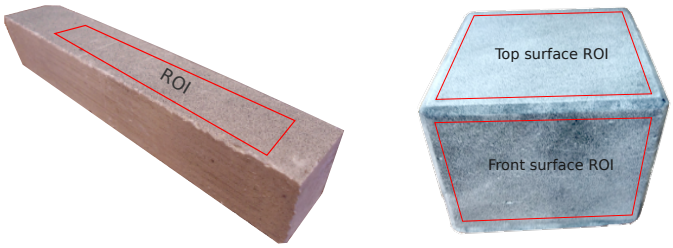

(a) (b)

Figure 3.1: Photographs of the two main types of specimens.(a) 25 × 25 × 150 mm^3 bar (designation: 50 T1b) for IET and (b) 70 × 70 × 70 mm^3 cube (designation: 50 T1c). The Regions of Interest (ROIs) used in the DIC analyses are depicted in red, sized ≈ 14 × 144 mm^2 and ≈ 60 × 60 mm^2, respectively.

The experiments using the bar-shaped specimens were carried out in an environment with 50% relative air humidity and 50 ℃. Similarly, the experiments using the cube-shaped specimens were conducted at the same relative air humidity and two different temperature levels, namely, 50 and 70 ℃ and were duplicated. The results of each imaged surface are presented and named by F (for the front surface), and T (for the top), see Figure 3.1, followed by the specimen shape and a number to distinguish duplicates. For example, the results of the second experiment carried out analyzing the front surface of the cube tested at 70 ℃ and 70% of relative air humidity are designated as T70-H70-F2c (*i.e.,* (temperature)-(relative air humidity)-(surface + specimen number + specimen shape)). All the studied conditions are summarized in Table 3.2.

Table 3.2: Studied conditions and their designated code.

Code	Temperature [℃]	Humidity [%]	Surface	Repetition	Shape
T50-H50-F1c	50	50	Front	1	cube
T50-H50-T1c	50	50	Top	1	cube
T50-H50-F2c	50	50	Front	2	cube
T50-H50-T2c	50	50	Top	2	cube
T50-H70-F1c	50	70	Front	1	cube
T50-H70-T1c	50	70	Top	1	cube
T50-H70-F2c	50	70	Front	2	cube
T50-H70-T2c	50	70	Top	2	cube
T70-H50-F1c	70	50	Front	1	cube
T70-H50-T1c	70	50	Top	1	cube
T70-H50-F2c	70	50	Front	2	cube
T70-H50-T2c	70	50	Top	2	cube
T70-H70-F1c	70	70	Front	1	cube
T70-H70-T1c	70	70	Top	1	cube
T50-H50-T1b	50	50	Top	1	bar
T50-H50-T2b	50	50	Top	2	bar
T50-H50-3b*	50	50	*	3	bar
T50-H50-4b*	50	50	*	4	bar

* specimens used in the IET tests. Therefore there is no photographed surface

An equilateral cylinder with 50 mm height was fabricated following the same procedure as the cubes and the bars (Figure 3.2). It was used in tomographic scans to make sure that cracks begin on the surface and propagate toward the specimen center. The chosen cylindrical shape improves the quality of the volumes acquired because the X-rays transverse approximately the same length of the material medium during the rotation, which does not happen for a cubic specimen, for example.

Figure 3.2: Photographs of the cylinder specimen

3.3 X-ray tomography

The specimen was kept at room temperature (≈ 25 °C) and room humidity (*i.e.,* 40-50%) for 14 days. Acquisitions were carried out with the help of the X50-CT+ scanner (North Star Imaging, USA) located at LMT (ENS Paris-Saclay). The X-ray tube equipped with a W target was set to 200 kV with a current of 360 µA, resulting in a power of 62 W. A 0.3 mm thick copper filter was used to limit beam hardening. The volume of the specimen was reconstructed using 1,200 radiographs that were acquired over one 360° revolution. Each radiograph was obtained as the average of 30 frames to reduce acquisition noise. The result was a 3D image with 1,000 × 1,000 × 1,000 voxel definition and a resolution of ≈ 60 µm per voxel.

3.4 Image acquisition and DIC parameters

The hardware parameters of the optical setup are reported in Table 3.3. An exposure time of 3.2 s was chosen to perform a physical average of the intensity acquired by each pixel [142]. LED lights were put inside the climatic chamber for lighting purposes.

Table 3.3: Image acquisition hardware parameters

Camera	CANON T5 Rebel
Definition	3529 × 5296 pixels (Bayer pixels)
Color filter	Bayer
Gray Levels amplitude	16 bits
Lens	CANON 100 mm macro
Aperture	f/22
Field of view	65 × 65 mm^2
Scale	50 µm/pixel
Stand-off distance	102 cm
Rate	360 fph (set #1); 2 fph (set #2)
Exposure time	3.2 s
Patterning technique	sprayed black paint
Pattern feature size♯	4 pixels (B/W)

♯evaluated as full width at half maximum of auto-correlation function

The images were acquired as RAW files and then converted to gray scale

TIFF images using the Bayer filter [143]. The latter is an assembly of RGB filters arranged as a mosaic with a proportion of 25% red, 50% green, and 25% blue on the camera sensor. The conversion from RAW to TIFF was performed as the average of one red, two green, and one blue levels, which reduces the image definition by a factor 2 $\times$ 2. The images were classified into two sets. For set #1, the time interval between acquisitions was 10 s, and this set was used to study the changes in the gray values caused by lighting variations. After the set #1, the images of set #2 were acquired at intervals of 30 min. The set #2 was used to monitor the cracks, evaluate the effect of MR and BCC on the cracks, and also apply the SVD and Adaptive meshing.

3.5 Impulse Excitation Technique (IET)

The Impulse Excitation Technique (IET) was used following the ASTM E1876 standard [13] to estimate the Young's modulus E and, indirectly, the damage level caused by magnesia hydration. Two bar specimens were extracted from and repositioned into the climatic chamber in intervals of $\approx$ 1 h to measure their Young's moduli, while the other two bars were kept in the climatic chamber for image acquisition. The RFDA Professional device (IMCE Genk, Belgium) was used for this procedure. The excitation mode was defined as flexure. The bar specimens, specifically the region of harmonic nodes, were placed on polymeric wires. A microphone was positioned above and a pneumatic actuator below the bar, at the middle of its length. At least three pulses were captured before computing the value of the Young's modulus and the final value was obtained by the average of the results.

3.6 Mechanical Regularization in DIC

The strain field dependence on the element size makes it a crucial parameter for monitoring cracks. The elements should be small enough to contain only one crack inside, otherwise, the MCOD is inaccurate. However, small elements have fewer pixels inside, which makes them more sensitive to lighting variations, acquisition noise, and the convergence of the algorithm is compromised.

The Mechanical Regularization (MR) restricts the number of possible solutions to the system, improving its conditioning, which helps its convergence. However, the MR also smooths the displacement jumps caused by crack initiation, reducing the resolution of crack representation. In this thesis, meshes with five different element sizes were tested, using no MR or three different lengths. As mentioned in Section 2.8 (page 23), the regularization length raised to the power 4 is proportional to the weight of the MR. The results for one image of T70-H70-T1c are shown in Section 4.3 (page 52). The bulk type of MR was used because there are no external loads to create Neumann's boundary conditions, neither prescribed displacement to create Dirichlet's ones, which would call for additional MR treatments [126].

3.7 Brightness and Contrast Correction in DIC

In this thesis, three different types of gray level corrections were used, namely only brightness correction (B), only contrast correction (C), and brightness and contrast (BC) corrections. Two discretizations were applied herein. The first consisted of one 8-noded quadrilateral element (Q8) with the same size of the ROI. This Q8 element was used to perform gray level corrections taking into account the variations of brightness and contrast over the entire surface (*i.e.,* with eight DOF per corrected component). The second was a fine mesh (FM) composed of 3-noded triangular elements (T3) with an average size of 6 px ($\approx$ 40,000 nodes). This second mesh was also utilized for the discretization of the displacement fields (*i.e.,* DIC + BCCs) and for the analyses with no correction (*i.e.,* standard DIC).

The FM can be seen in a zoomed zone shown in Figure 3.3. Such mesh covers the whole ROI (Figure 3.3) but the elements are too small to be displayed in the reference image with no zoom. The results were designated by a tag as standard DIC (*i.e.,* no applied correction), and the mesh used in the correction followed by the type of correction. For example, Q8 B means only brightness correction using the 8-noded quadrilateral element.

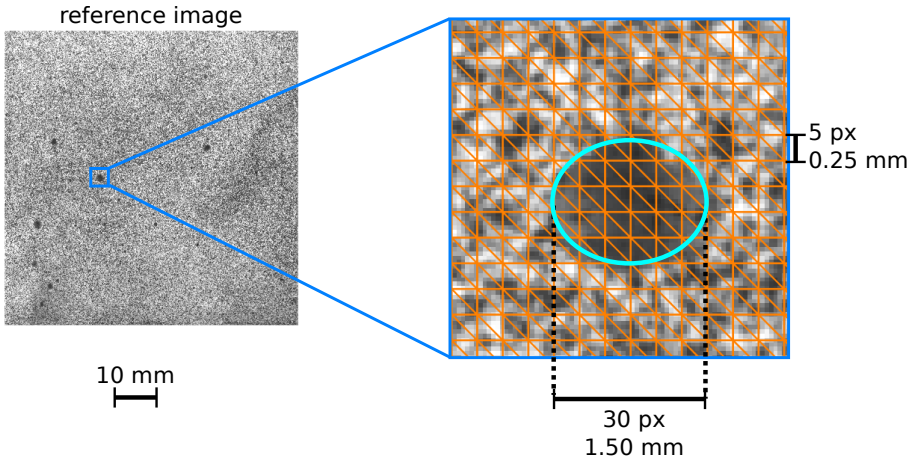

Figure 3.3: Reference image used in the DIC analyses with an indication of the Region of Interest (ROI) and a zoom of an area containing one open pore.

The images were processed using Correli 3.0 in which BCCs were implemented, and the used parameters are shown in Table 3.4.

Table 3.4: DIC analysis parameters for BCCs analyses

DIC software	Correli 3.0 [18]
Image filtering	none
Element length	6 pixels
Shape functions	linear (T3)
Mesh	regular (see Figure 3.3)
Matching criterion	see text
Interpolant	cubic
Displacement noise-floor	see Table 4.1 (page 63)
Strain calculation	derivative of shape functions
Strain noise-floor	see Table 4.1 (page 63)

3.8 DIC-based quantification of crack networks

The results provided by DIC that are reported in this thesis are the Mean Crack Opening Displacement (MCOD) per element and the Superficial Crack Density (SCD). The former was calculated from the mean strain tensor estimated for each element (e) covering a domain Ω_e. In the presence of cracks, the mean strain tensor can be expressed as [144]

$$\bar{\boldsymbol{\epsilon}} = \frac{1}{|\Omega_e|}\int_{\Omega_e} \boldsymbol{\epsilon}(\mathbf{x})\mathrm{d}\mathbf{x} + \frac{1}{|\Omega_e|}\int_{\Gamma_e} [\![\mathbf{u}(\mathbf{x})]\!] \boxtimes \mathbf{n}(\mathbf{x})\ \mathrm{d}\mathbf{s}, \tag{3.1}$$

where $[\![\mathbf{u}]\!]$ denotes the displacement jump, $\mathbf{n}$ the normal to the cracked surface Γ_e, $\boxtimes$ the symmetrized tensorial product, $\boldsymbol{\epsilon}$ the strain tensor of the uncracked matrix, and s the curvilinear abscissa along the crack path. In the following, it is assumed that the strain levels due to curing and drying are negligible with respect to the singular share provided by cracks. Consequently, the mean strain tensor becomes,

$$\overline{\boldsymbol{\epsilon}} \approx \frac{1}{|\Omega_e|} \int_{\Gamma_e} [\![\mathbf{u}(\mathbf{x})]\!] \boxtimes \mathbf{n}(\mathbf{x}) \, \mathrm{ds}. \tag{3.2}$$

The MCOD $\overline{[\![\mathbf{u}]\!]}$ per FE is defined as,

$$\overline{[\![\mathbf{u}]\!]} \boxtimes \overline{\mathbf{n}} = \frac{1}{|\Gamma_e|} \int_{\Gamma_e} [\![\mathbf{u}]\!] \boxtimes \mathbf{n} \, \mathrm{ds}, \tag{3.3}$$

where $\overline{\mathbf{n}}$ is the mean crack normal. Further, it is assumed that the main opening share is associated with the mode I regime

$$\overline{[\![\mathbf{u}]\!]} = [\![u]\!] \, \overline{\mathbf{n}} \tag{3.4}$$

such that $\overline{\mathbf{n}}$ then corresponds to the eigen direction associated with the average maximum principal strain $\overline{\epsilon}_1$. The latter is then related to the MCOD $\overline{[\![u]\!]}$ by

$$|\Omega_e| \, \overline{\epsilon}_1 = |\Gamma_e| \, \overline{[\![u]\!]} \tag{3.5}$$

It is worth noting that $|\Omega_e|/|\Gamma_e|$ scales with the element size ℓ, provided only one crack is present in each element. This is likely to be true for small element sizes. Consequently, the MCOD is approximated by

$$\overline{[\![u]\!]} = \ell \, \overline{\epsilon}_1. \tag{3.6}$$

The SCD was estimated by the ratio of the number of damaged elements to the total number of elements. To define damaged elements, an eigen strain threshold ϵ_1^* was defined. The latter is obtained by evaluating the standard deviation of the average maximum principal strain $\sigma(\overline{\epsilon}_1)$ for the first ten images, which

were captured at the very beginning of the experiment with a time interval of 10 s. As the images were recorded before crack initiation, $\sigma(\bar{\epsilon}_1)$ is associated to the experimental setup (*i.e.,* fluctuations in lighting and acquisition noise of the camera sensors). $\sigma(\bar{\epsilon}_1)$ was then multiplied by a factor A to account for the strains induced by the expansion during the brucite formation before the initiation of cracks.

In order to choose an appropriate constant A, different values were tested and the effects on SCD data at the very beginning of the experiments were investigated. Because SCD should be close to zero before crack initiation, it was chosen as the smallest factor that resulted in a mean SCD less than 1% for the 10 initial images. For reducing the user's influence on selecting A, additional research should be carried out. As the level of ϵ_1^* was set (for each experiment), the elements whose average maximum principal strain $\bar{\epsilon}_1$ was greater than ϵ_1^* were classified as damaged. The number of damaged elements $D_e(t)$ was then obtained as a function of time t, and then the superficial crack density (SCD) was calculated by the equation below,

$$SCD(t) = \frac{D_e(t)}{N_{el}}, \tag{3.7}$$

where N_{el} is the total number of elements in the mesh.

For the analyses comparing cubic and bar-shaped samples, and different test conditions (*e.g.,* temperature and relative air humidity) the element size was $\approx$ 800 µm (or 16 pixels).

3.9 Principal Component Analyses applied to DIC

The Principal Component Analyses (PCA) was used to decompose the displacement fields (horizontal and vertical components) over time, which was used as a denoising procedure and as a tool to analyze separately the most relevant modes. The matrix $[\mathbf{U}]$ was constructed with the displacements of each node

disposed in each line, for example

$$\begin{bmatrix} u_{1x}^1 \\ u_{2x}^1 \\ \vdots \\ u_{mx}^1 \\ u_{1y}^1 \\ u_{2y}^1 \\ \vdots \\ u_{my}^1 \end{bmatrix}$$

where the first subscript is the node label, and the other one is the direction of the displacement. Therefore, each column contained the displacements of one analyzed image pair. One given row contained the displacement evolution of one node represented by the superscript ranging from 1 to n

$$\begin{bmatrix} u_{1x}^1 & u_{1x}^2 & \cdots & u_{1x}^n \end{bmatrix}$$

where n is the number of analyzed images. The complete matrix $[\mathbf{U}]$ becomes

$$\begin{bmatrix} u_{1x}^1 & u_{1x}^2 & \cdots & & u_{1y}^n \\ u_{2x}^1 & & & & \\ \vdots & & & & \\ u_{mx}^1 & & \ddots & & \\ u_{1y}^1 & & & & \\ u_{2y}^1 & & & & \\ \vdots & & & & \\ u_{my}^1 & & & & u_{mx}^n \end{bmatrix}$$

The input matrix, as was constructed, makes the modal matrix $[\mathbf{V}]$ be composed of spatial modes, whereas the matrix $[\mathbf{T}]$ contains the temporal ones. The Singular Value Decomposition SVD deals with rectangular matrices $[\mathbf{U}]_{m \times n}$, be-

ing $m > n$ in this case. The product $[\mathbf{U}][\mathbf{U}]^\top$ provides a square matrix. The eigen decomposition of the product result is carried out to define the eigen values λ from the polynomial ρ:

$$\rho(\lambda) = \det([\mathbf{U}][\mathbf{U}]^\top - \lambda[\mathbf{I}]) = 0 \ , \tag{3.8}$$

The singular values are the square root of the previous eigen values ($s_i = \sqrt{\lambda_i}$). SVD results in three matrices, namely, the singular values $[\mathbf{S}]_{m\times n}$ diagonal matrix with the singular values s_i ordered by importance ($s_1 \geqslant s_2 \geqslant s_3 \geqslant ...s_n$), and the modal matrices $[\mathbf{V}]_{m\times m}$ and $[\mathbf{T}]_{n\times n}$, which permit matrix $[\mathbf{U}]$ to be recovered,

$$[\mathbf{U}] = [\mathbf{V}][\mathbf{S}][\mathbf{T}]^\top, \tag{3.9}$$

Since the DIC displacement fields were placed in a space/time arrangement in $[\mathbf{U}]$ (*i.e.,* space information in columns and time information in rows), the matrix $[\mathbf{V}]$ is composed of spatial modes (SM), whereas the matrix $[\mathbf{T}]$ contains the temporal modes (TM). In the following analyses, SVD was carried out using the algorithm implemented in Matlab (*i.e.,* `[V,S,T] = svd(U,'econ')` The 'econ'option considerably reduces the amount of RAM needed depending on the mesh size and number of frames. For example, in cases where the number of nodes are larger than the number of frames (*i.e.,* $[\mathbf{U}]_{m\times n}$ with $m > n$) the algorithm carries out n operations, avoiding $m - n$ repeated zero results. It considerably reduces the amount of RAM needed. In this thesis, for example a studied case consists of a mesh with 40,000 nodes (with two DOFs per node) and 200 images were analyzed. Therefore a $80,000 \times 200$ $[\mathbf{U}]$ matrix was created, and the result is a singular values matrix $[\mathbf{S}_{\mathbf{200\times 200}}]$ instead of a $[\mathbf{S}_{\mathbf{8000\times 8000}}]$.

The $[\mathbf{S}]$ matrix is a direct indicator that some modes are orders of magnitude more relevant than others because of their ranking, from higher variation to lower. The Principal Component Analysis (PCA) truncates the $[\mathbf{U}]$ to obtain the

approximation $[\mathbf{U}_k]$ with the first k modes.

$$[\mathbf{U}_k] = [\mathbf{V}_k][\mathbf{S_k}][\mathbf{T_k}]^\top, \tag{3.10}$$

where $[\mathbf{S}_k]$ contains the first k singular values (*i.e.,* diagonal matrix of dimension $k \times k$), and $[\mathbf{V}_k]$ and $[\mathbf{T}_k]$ are the corresponding reduced modal matrices of dimension $m \times k$ and $n \times k$, respectively. The same PCA was applied to maximum eigen strain ϵ_1 fields that were also separated in space and time to form rectangular matrices $[\mathbf{E}]_{p \times n}$, where p is the number of elements. It is worth noting that the strains are uniform over each element and only one value was kept for each element. The interest of considering strain fields in addition to displacement fields is that they are insensitive to rigid body motions, which are noise sources as addressed in the Results chapter.

The price of reducing data by truncation is an error that raises from the discarded modes. The truncation error will be compared to the uncertainty level of the considered quantity.

3.10 Adaptive meshing

It is proposed to start off with a coarse mesh and to use the criterion to refine the 'damaged' elements (*i.e.,* $\overline{[\![u]\!]} \geq [\![u^*]\!](L)$), which will better capture the kinematics and morphology of the crack locations while possibly remaining with low computational cost. The complete procedure consists of the following steps:

1. perform a DIC analysis using a coarse uniform mesh (UM);
2. choose an image pair with the highest displacement jump ($[\![u]\!]$) for crack evaluation;
3. list the damaged elements for this image pair and considered discretization;
4. execute one subdivision in the damaged elements (*i.e.,* each selected element generates four new ones);

5. identify the hanging nodes and respective parent nodes;

6. construct the Lagrange matrix and perform DIC analyses for this image pair using the locally refined mesh;

7. repeat items 3 to 6 until the smallest elements achieve the size desired by the user;

8. perform a DIC analysis for all the images using the optimized mesh.

This approach was implemented here within the Correli 3.0 framework [18] and is described in the flowchart of Figure 3.4. The end of the adaptive procedure at the present implementation is a user decision based in the size of the smallest element after division as a stop criterion. For example, the smallest element size may be guided by the highest measured MCOD using UMs. If even smaller elements were envisaged (down to one pixel size), damage could be used along with the mechanical regularization [39].

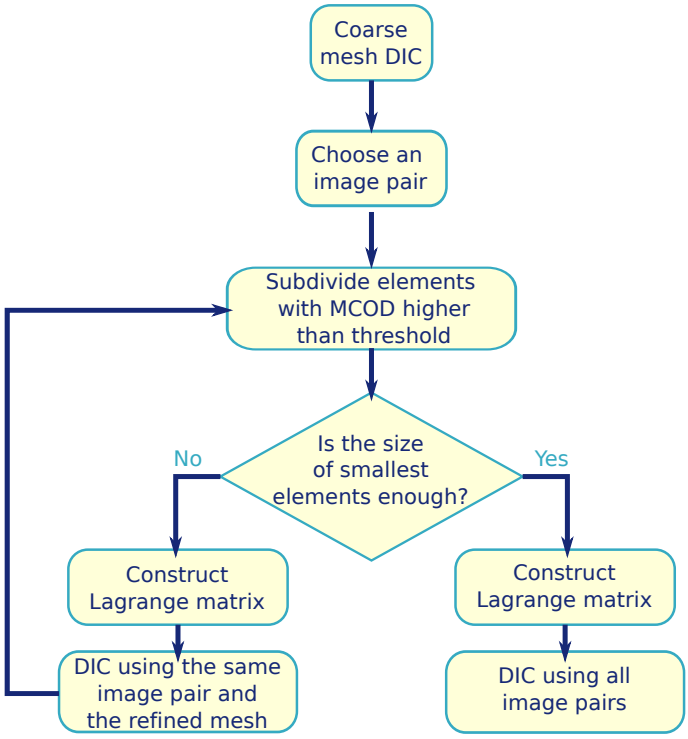

Figure 3.4: Flowchart of the AM procedure applied to DIC, using MCOD as division criterion

It is worth noting that the end of the adaptive meshing is a user decision. As a perspective, the algorithm could be improved to use gray level residuals to inform the user about the best mesh among the refinement iterations, and / or use the PCA to chose the division and stop criteria.

3.11 Lagrange multipliers

Lagrange multipliers may be employed to enforce additional constraints to a system of equations. In the present case, the displacements of a given hanging node need to be the average of the displacement of its parent nodes. The average was used because the edges were always split in the middle and the shape functions are linear (otherwise, weights related to the distance from the hanging node to each parent node should be considered). Such an approach can be easily implemented in a DIC algorithm, and does not require the DIC Hessian to be changed, because only an auxiliary matrix $[\mathbf{L}]$ is added. Each column accounts for one constraint, namely, the parent DOFs $p1i$ and $p2i$, the hanging node hi, where i is the hanging node label. The constraint is written as

$$v_{p1i} + v_{p2i} - 2v_{hi} = 0 \tag{3.11}$$

To avoid degrading the conditioning of the full system, the matrix $[\mathbf{L}]$ is pre-multiplied by the ratio of Frobenius norms of $[\mathbf{M}]$ and $[\mathbf{L}]$, which is called ζ. Once all the desired constraints are accounted for, the augmented Hessian $[\mathbf{H}]$ becomes

$$[\mathbf{H}] = \left[\begin{array}{c|c} [\mathbf{M}] & \zeta[\mathbf{L}]^\top \\ \hline \zeta[\mathbf{L}] & [\mathbf{0}] \end{array}\right] \tag{3.12}$$

The vector of unknowns $\{\beta\}$ gathers all nodal displacements $\{\boldsymbol{v}\}$ and Lagrange multipliers $\{\boldsymbol{\lambda}\}$, and the residual vector $\{\mathbf{h}\}$ reads

$$\{\mathbf{h}\}^\top = \{\{\mathbf{F}\}^\top \{\mathbf{0}\}^\top\} \tag{3.13}$$

resulting in a system to solve

$$[\mathbf{H}]\{\delta\beta\} = \{\mathbf{h}\} \tag{3.14}$$

In experimental cases, defining which elements need to be divided is not straightforward. There are several choices, among them the maximum eigen strains [39, 145, 146] and the gray level residuals [39, 147–152]. It is worth noting that the eigen strains are computed as the average over each element. Conversely, the gray level residuals $\rho(\mathbf{x}) = f(\mathbf{x}) - g(\mathbf{x} + \upsilon_p^m \mathbf{\Psi}_\mathbf{p}(\mathbf{x}))$, where υ_p^m are the measured nodal displacements (*i.e.,* at convergence of the DIC code), are defined at the pixel scale. In both cases, a user-defined threshold will be required.

Refinement Criterion

It is proposed a *explicitly* refinement criterion that accounts for displacement jumps and their associated measurement uncertainty. The displacement jumps represent cracks in the displacement fields, which the detection and quantification are sought in this thesis.

In the presence of cracks, the mean strain tensor in each element is expressed as [144]

$$\overline{\boldsymbol{\epsilon}} = \frac{1}{|\Omega_e|}\int_{\Omega_e} \boldsymbol{\epsilon}(\mathbf{x})\mathrm{d}\mathbf{x} + \frac{1}{|\Omega_e|}\int_{\Gamma_e} [\![\mathbf{u}(\mathbf{x})]\!] \boxtimes \mathbf{n}(\mathbf{x})\ \mathrm{ds} \tag{3.15}$$

where $[\![\mathbf{u}]\!]$ denotes the displacement jump, $\mathbf{n}$ the normal to the cracked surface Γ_e, $\boxtimes$ the symmetrized tensorial product, $\boldsymbol{\epsilon}$ the strain tensor of the uncracked matrix, and s the curvilinear abscissa along the crack path. In the following, it is assumed that the elastic strain levels are negligible with respect to the singular contribution provided by cracks. Consequently, the mean strain tensor reduces to

$$\overline{\boldsymbol{\epsilon}} \approx \frac{1}{|\Omega_e|}\int_{\Gamma_e} [\![\mathbf{u}(\mathbf{x})]\!] \boxtimes \mathbf{n}(\mathbf{x})\ \mathrm{ds} \tag{3.16}$$

The mean crack opening displacement $\overline{[\![\mathbf{u}]\!]}$ per element is defined as

$$\overline{[\![\mathbf{u}]\!]} \boxtimes \overline{\mathbf{n}} = \frac{1}{|\Gamma_e|} \int_{\Gamma_e} [\![\mathbf{u}]\!] \boxtimes \mathbf{n} \, \mathrm{d}\mathbf{s} \tag{3.17}$$

where $\overline{\mathbf{n}}$ denotes the mean crack normal. Further, it is assumed that the main opening contribution is associated with the mode I regime (opening).

$$\overline{[\![\mathbf{u}]\!]} = \overline{[\![u]\!]} \, \overline{\mathbf{n}} \tag{3.18}$$

such that $\overline{\mathbf{n}}$ then corresponds to the eigen direction associated with the average maximum eigen strain ϵ_1. The latter is then related to the mean crack opening displacement $\overline{[\![u]\!]}$ by

$$|\Omega_e| \, \epsilon_1 = |\Gamma_e| \, \overline{[\![u]\!]} \tag{3.19}$$

It is worth noting that $|\Omega_e|/|\Gamma_e|$ scales with the element size ℓ, provided only one crack is present in each element. This hypothesis is likely to be true for small element sizes, which also reinforces the refinement. Consequently, the mean crack opening displacement is approximated by $\overline{[\![u]\!]} = \ell \, \overline{\epsilon}_1$ ((3.6) on page 38). The mean crack opening displacement threshold $[\![u^*]\!]$ will be set to classify elements as damaged (*i.e.,* $\overline{[\![u]\!]} \geq [\![u^*]\!]$). It is proposed to relate $[\![u^*]\!]$ to its measurement uncertainty (*i.e.,* typically 5 times or more its standard uncertainty $\sigma(\overline{[\![u]\!]})$). According to Equation (3.6), the uncertainty $\sigma(\overline{[\![u]\!]})$ is related to the standard strain uncertainty $\sigma(\epsilon_1)$ by $\sigma(\overline{[\![u]\!]}) = \ell\sigma(\epsilon_1)$. Further, the strain uncertainty $\sigma(\epsilon_1)$ is dependent on the element size

$$\sigma(\epsilon_1) = N\ell^{\alpha} \tag{3.20}$$

and characterizes the compromise to be carried out between the uncertainty and the discretization level (*i.e.,* increasing the spatial resolution by creating new elements). Typical values of the power α ranges between -1 and -2 (*i.e.,* when the measurement uncertainties are random and controlled by white Gaussian noise [94]). The constant N is dependent on the contrast in the picture and the noise level [153]. The standard deviations $\sigma(\epsilon_1)$ (and therefore $\sigma(\overline{[\![u]\!]})$) are obtained by performing uncertainty quantifications prior to each analyzed test.

Consequently, the threshold $[\![u^*]\!]$ becomes

$$[\![u^*]\!](\ell) = kN\ell^{\alpha+1} \tag{3.21}$$

where k is a proportionality constant between the standard uncertainties. Thus, the threshold $[\![u^*]\!]$ explicitly depends on the discretization level. This observation means that the threshold $[\![u^*]\!]$ has to be changed for each refinement step to account for the reduction of element size, or equivalently to capture elements that crack opening displacement is greater than $[\![u^*]\!]$. During the analysis the elements were divided by two and the threshold is multiplied by 2 (α range between -1 and -2) in each refinement step. Also, this influence is compared to a constant $[\![u^*]\!]$ in the Results chapter.

By using Equation (3.6), a strain threshold $\epsilon^*(\ell) = [\![u^*]\!](\ell)/\ell$ can also be defined. With the previous proposition, it is concluded that ϵ^* is also length dependent. This proposition departs from the use of a unique strain threshold [145, 146, 151] when multiple refinement steps are to be performed. Both thresholds (*i.e.,* $\epsilon_1^*(\ell)$ and $[\![u^*]\!](\ell)$) introduced herein relate to the measurement uncertainties of the associated quantities (*i.e.,* ϵ_1 and $\overline{[\![u]\!]}$). Throughout this work the discussion will be focused on the usage of $[\![u^*]\!](\ell)$.

4 RESULTS AND DISCUSSION

4.1 Climatic Chamber

The in-house climatic chamber was equipped with temperature and relative air humidity controllers, tempered glass windows, and high definition digital cameras to carry out acquisitions during the whole stages of curing and drying of refractory castables. A detailed sketch is shown in Figure 4.1.

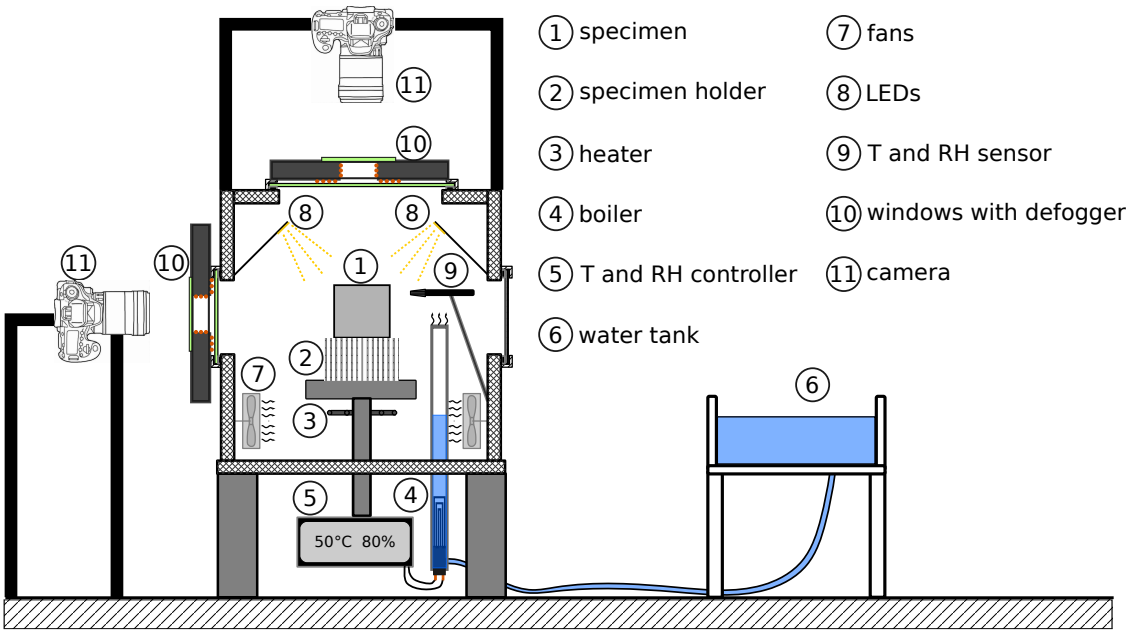

Figure 4.1: Schematic view of the experimental setup of the in-house made climatic chamber for monitoring MgO hydration via DIC analyses

Inside the chamber, the specimen ① was placed on the tip of thin metal rods ② to reduce specimen displacement constraints and ensure that all surfaces were in contact with moist air. A N322RHT device (Novus, Brazil), which is specific for confined environments and comprising a sensor ⑨ and a controller ⑤, was used to prescribe the temperature and relative air humidity inside the chamber. This controller was connected to a heater (electric resistance wire ③) and a boiler ④. The former heats up the air and the latter boils the water used as moisture source. A tank ⑥ supplied the water to the boiler. Four fans ⑦ located at the bottom of the climatic chamber generated forced airflow that increases

the temperature and humidity homogeneity inside the chamber. Glass windows were added to enable pictures of two of the specimen surfaces to be acquired, and LED lights (8) provided proper illumination. To avoid water vapor condensation on the windows, two defoggers (10) were inserted to heat them to temperatures five degrees Celsius above that inside the chamber. Two high definition (18 color Mpixel) Canon T5 digital cameras (11) equipped with Canon macro 100 mm lenses (Canon Inc., Japan) were used. The images were recorded every 10 s for the first 10 images, and every 30 min thereafter, with a $f/22$ aperture and exposure time of 3.2 s. The large exposure time was used to make a physical average of the changes in gray levels to mitigate heat haze effects [142].

Figure 4.2(a) shows a picture of the in-house climatic chamber from the outside, one can see the top camera and one of the defoggers; Figure 4.2(b) shows its inside with four bar-shaped specimens on the top of the metal rods, the lighting for the specimens front images, the heater and one of the four fans; Figure 4.2(c) shows the view of the specimens on the specimen holder from the top window.

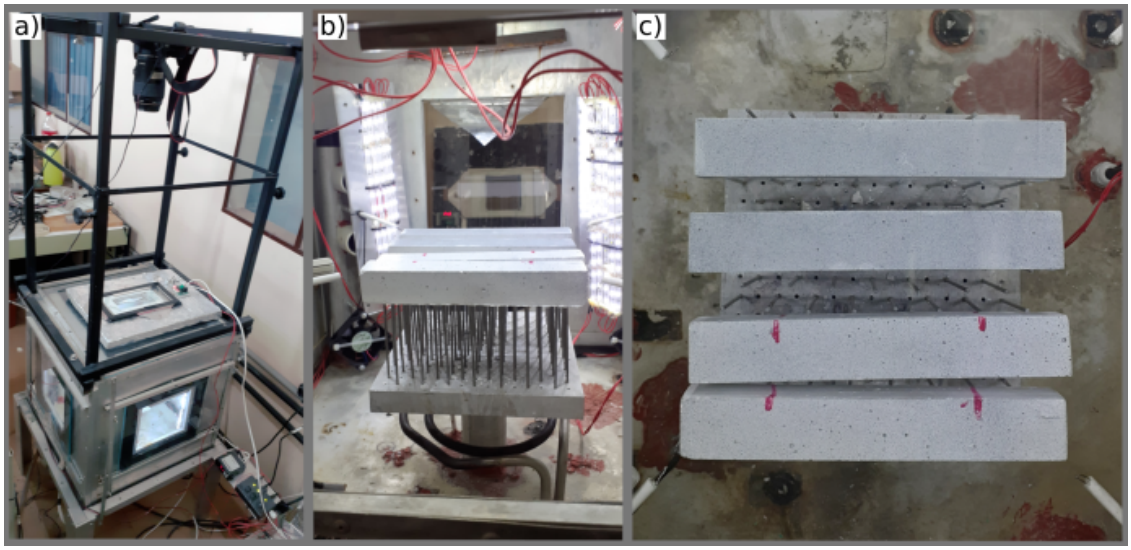

Figure 4.2: Pictures of the in-house climatic chamber: a) the outside of the chamber, b) its inside with four bar-shaped specimens and c) the view from the top window

4.2 Tomography scans

A slice of the reconstructed volume extracted at the middle height of a cylindrical specimen is shown in Figure 4.3. It is possible to distinguish the constituents of the microstructure by their respective density, which is represented by different colors, *i.e.,* the voids and cracks are black, the matrix is gray and the alumina aggregates are white. The propagation of two cracks is observed *ex situ* for the specimen kept at room-temperature and at room relative air humidity during 14 days after casting.

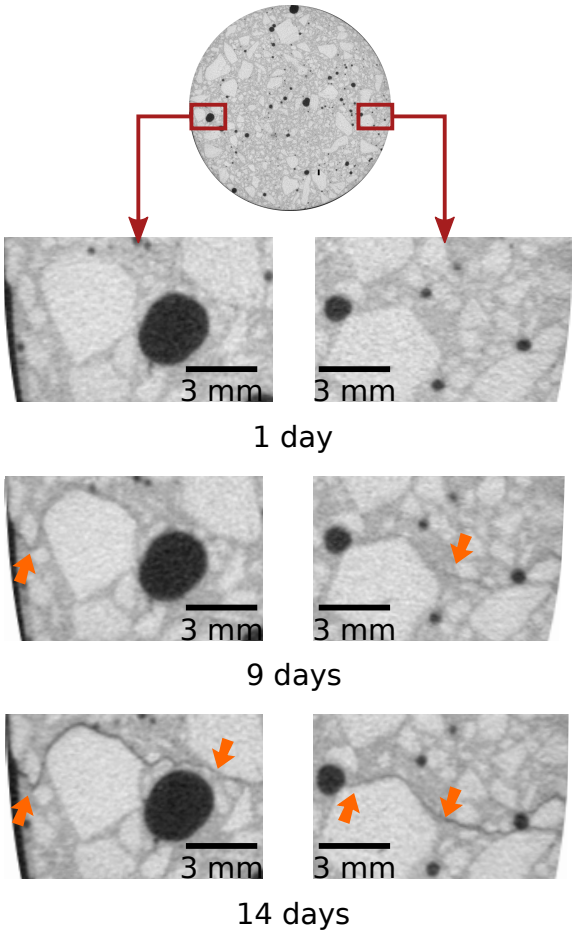

Figure 4.3: Middle height slice of the reconstructed volume of a cylindrical specimen made of refractory castable kept at room-temperature (≈ 24 ℃) and at room relative air humidity for 14 days. The constituents of the microstructure are distinguishable by their respective density represented by colors, *i.e.,* the voids and cracks are black, the matrix is gray and the alumina aggregates are white. The orange arrows indicate the crack front. The cracks initiate on the cylinder surface and propagate toward the center

The cracks depicted in the slices (Figure 4.3) initiated on the cylinder surface,

and both propagated toward the center axis. This observation validates using DIC (*i.e.,* a technique based on surface images) to study the damage caused by MgO hydration. Digital Volume Correlation (DVC) [39] may also be applied to study the damage initiated on the surface and its propagation within the bulk of the specimen, although such analyses are beyond the scope of the present thesis. Another important piece of information obtained by observing the volume is that the cracks propagated in the castable matrix. They do not start inside aggregates or cross them, which means that the DIC results may show regions with high maximum principal strains (*i.e.,* cracks) among others with virtually zero strains (*i.e.,* aggregates). This observation sheds some light on the likely relationship of the distribution of aggregates and crack networks.

4.3 Effect of Element size and Mechanical Regularization Length

DIC analyses were carried out for the specimen T70-H70-T1c using element sizes ℓ_e of 102, 51, 26, 13, and 6 px. These values were obtained by the square root of the mean area of the triangular elements. The MR lengths (ℓ_m) were 0, 10, 25, and 100 px. One frame was chosen such that the crack network was fully developed to evaluate the effect of these parameters on the residuals and the maximum principal strain field. The Root Mean Square (RMS) of gray level residuals normalized by the dynamic range of the reference picture are shown in Figure 4.4 for each tested condition.

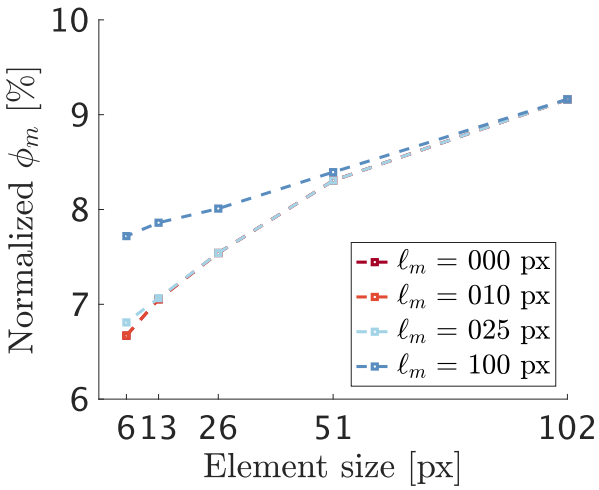

Figure 4.4: Normalized RMS ϕ_m for different element sizes ℓ_e and MR lengths for test T70-H70-T1c

The residuals decrease with the decrease of element size because more kinematic details are captured. In the aggregates, the strain is virtually equal to zero, and the displacements are mainly small rigid body motions. This is an example where local h-refinement is useful, because large elements represent well the kinematics of the aggregates but do not capture the crack network. Comparing the MR lengths for the analysis with an element size of 6 px, the RMS residuals increase with ℓ_m because the cracks are discontinuities in the displacement field that are not considered by the linear elastic model. The effect of MR on the strain field was evaluated by the RMS and the standard deviation (STD) of ϵ_1 fields, which are reported in Figure 4.5. MR spreads the displacement jumps in the crack path to the adjacent elements, thereby reducing the values of ϵ_1.

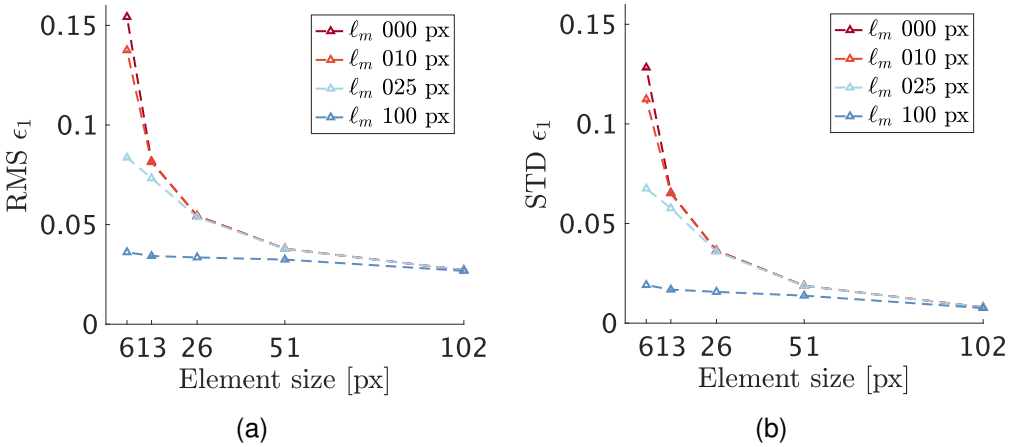

Figure 4.5: Effect of element size and ℓ_m in the maximum principal strain for test T70-H70-T1c

The RMS of ϵ_1 increases as the element size decreases (Figure 4.5(a)). It happens because the displacement due to crack opening is computed for smaller elements. For the analysis with $\ell_m = 100$ px, there is a slight increase in RMS and STD of ϵ_1 because the MR is very severe in this case. Figure 4.5(b) shows a similar trend for STD of ϵ_1 that is due to a better distribution of elements on the aggregate regions (zero strain) and crack paths (high strain). It makes the strain distribution larger, which is represented by the STD increase.

To illustrate the above discussion, the strain fields are plotted in Figure 4.6 for $\ell_m = 10$ px and different element sizes ℓ_e. The crack network resolution increases for smaller values of ℓ_e. It is worth noting that the color bar scales are different for each field in Figure 4.6 because the displacement jumps are averaged over larger sizes. The strain field for the mesh with $\ell_e = 6$ px is noisier due to measurement uncertainties (*i.e.,* isolated elements with high ϵ_1 among cracks). The principal causes of noise in this experiment are changes in lighting due to vapor streams. In the following section, methodologies to correct this effect (Section 4.4) or to filter it (Section 4.8) are presented.

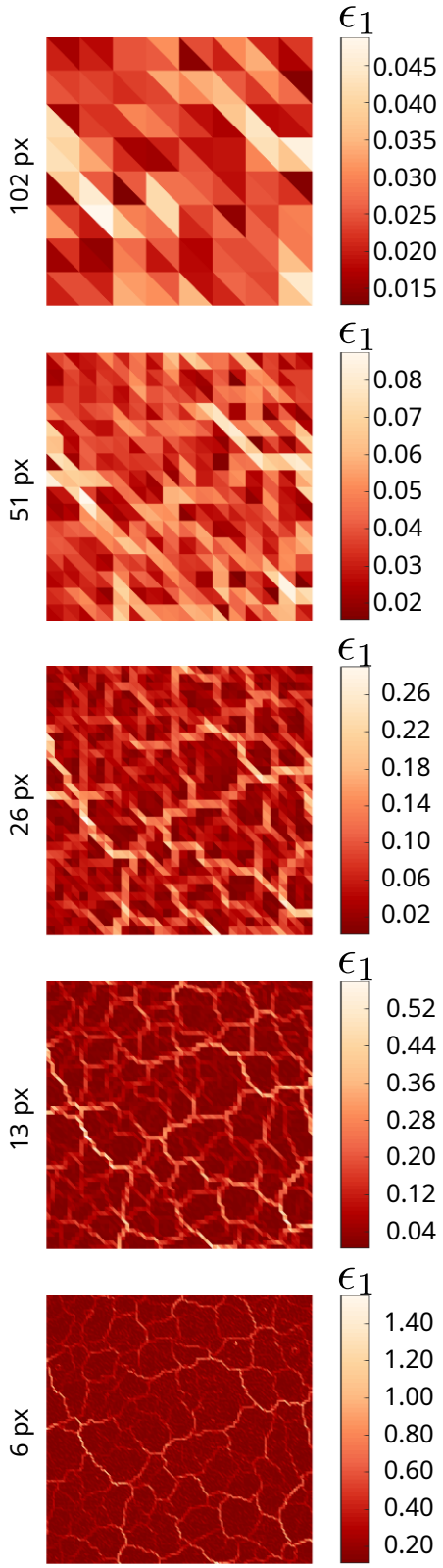

Figure 4.6: Maximum principal strain fields using different element sizes ($\ell_e = 102, 51, 26, 13, 6$ px) for the T70-H70-T1c test and $\ell_m = 10$ px. The color bar range is different for each mesh for better visualization

The effect of MR in the ϵ_1 field for the mesh (ℓ_e = 6 px) is evaluated by comparing the result of DIC analyses using ℓ_m = $100, 25, 10, 0$ px, and shown in Figure 4.7.

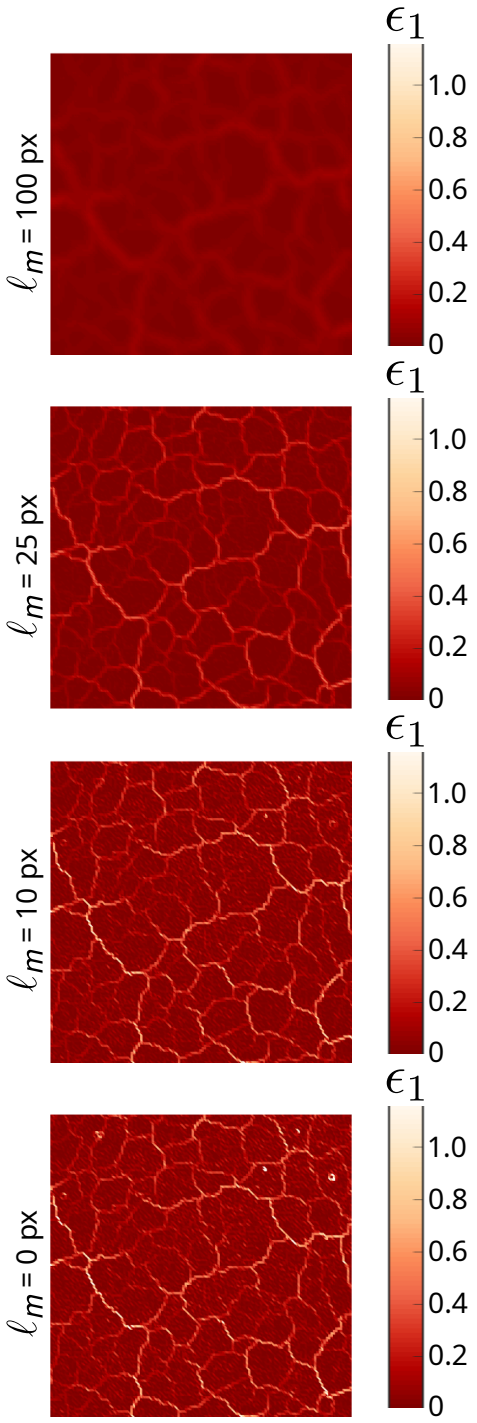

Figure 4.7: Comparison of ϵ_1 fields for the mesh with ℓ_e = 6 px for DIC analysis using ℓ_m = 100, 25, 10, and 0 (no MR) for test T70-H70-T1C

In Figure 4.7, the color bars were kept identical for all strain fields to highlight

the effect of MR. The resulting field for $\ell_m = 100$ px has wide cracks and small values of ϵ_1, a typical result of too high MR. The MR length of 25 px shows a good result with defined cracks and no visible noise. However, smaller cracks are difficult to detect. The analyses carried out with $\ell_m = 10$ px result in a field with a clear network but with a small noise effects. Last, the analyses with no MR show a field very similar to the previous one. However, there are some spots with high values of ϵ_1 (see lower right corner) that can be related to the difference in RMS and STD of ϵ_1 for these analyses, and the one with $\ell_m = 10$ px. For a better comparison of the fields, a histogram of each one of them is shown in Figure 4.8.

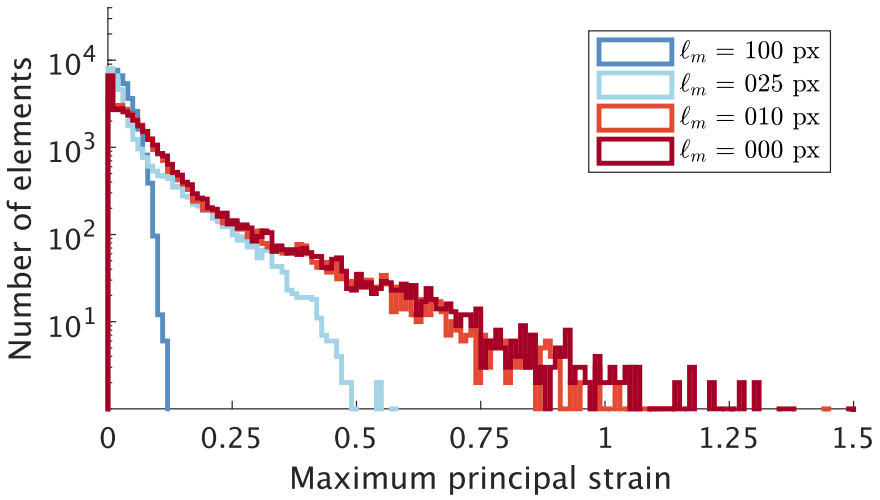

Figure 4.8: Histograms of ϵ_1 fields for the mesh with $\ell_e = 6$ px and DIC analyse using $\ell_m = 100, 25, 10, 0$ px for test T70-H70-T1c. The vertical axis is in logarithm scale to help the visualization of the number of elements with high strain values (*i.e.,* localized in the crack path) and the bin width is 10^{-3}

The histograms for $\ell_m = 10$ and 0 px are very close, which corroborates the statement that $\ell_m = 10$ px has a small effect on ϵ_1 levels. For the DIC analyses with no MR, there are elements with ϵ_1 values around 1.25 that are the bright spots in the lower right corner of the field. Consequently, the DIC analysis will be run hereafter using a mesh with $\ell_e = 6$ px, and MR with $\ell_m = 10$ px.

4.4 Brightness and Contrast Corrections

BCC results are shown for the experiment T50-H50-F1c to choose the best procedure that is applied in the subsequent sections for all the experiments.

4.4.1 Uncertainty quantification

The effect of the set-up in terms of gray level fluctuations and corresponding measurement uncertainties was analyzed using the image set #1. Each image was used as one reference, while the other nine were used as "deformed" pictures. This permutation resulted in 81 pairs analyzed by applying the three corrections, each one using the two discretizations (Q8 and FM) as described in Section 3.7.

In the following, the RMS of gray level residuals is reported. They correspond to the RMS of the gray level residuals $\phi_{\{\boldsymbol{v}\}}$ of pixels around each node of the FE mesh used in the kinematic discretization. They were subsequently normalized by the dynamic range of the reference image for standard DIC and compared to their counter-parts provided by DIC + BCC (*i.e.,* ϕ_{bcc}) when the Q8 discretization is used (Figure 4.9(a)), or when the FM discretization is selected (Figure 4.9(b)). If there is no effect using the BCC procedure, then the data should lie on the 45° line. Further, the values of ϕ_{bcc} resulting from the two discretizations used in the BCCs are compared in Figure 4.9(c).

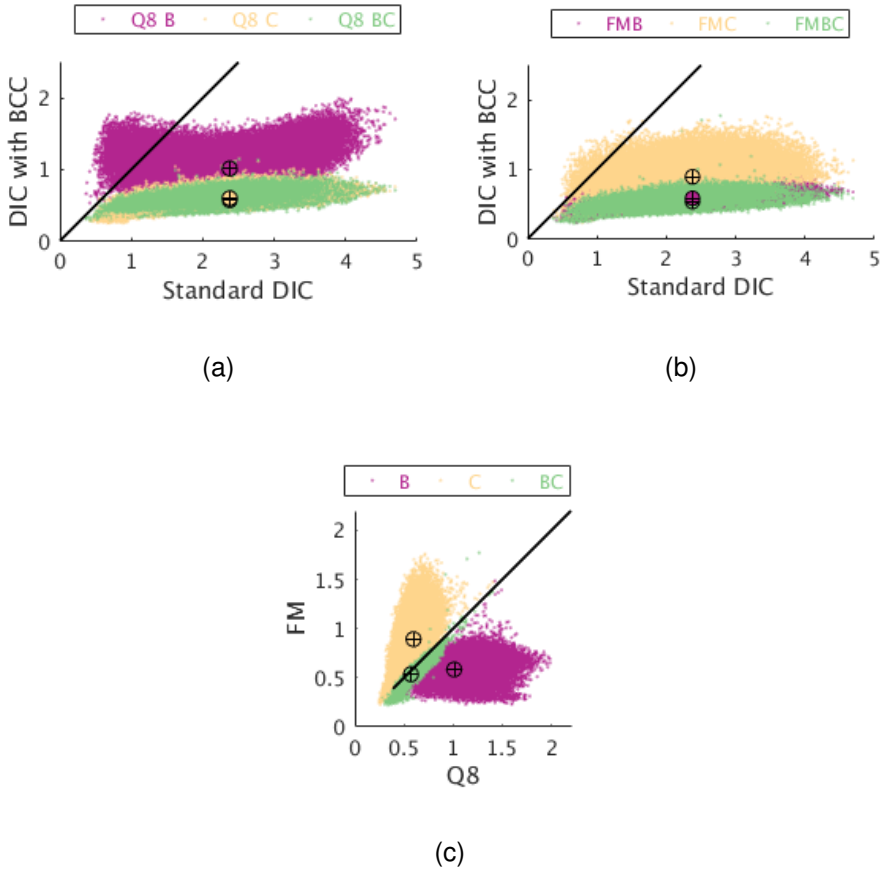

Figure 4.9: Normalized nodal residuals associated with ϕ_{bcc} (expressed in % of the dynamic range) for each type of correction: brightness (B), contrast (C), brightness and contrast (BC) compared with standard DIC residuals (computed from $\phi_{\{\boldsymbol{v}\}}$). Two different discretizations were considered in the corrections. (a) Effect of BCCs using the Q8 element, and (b) the fine mesh (FM). (c) Comparison between the results obtained with both discretizations. The circled crosses depict the mean level of each case

The results for ϕ_{bcc} with the three corrections and the two discretizations mostly lie below the 45° line, thereby proving that the BCCs reduced the overall gray level residuals. This result shows that the BCC procedure is beneficial to the reported DIC analyses. For the Q8 element, C and BC corrections achieved lower levels in comparison to B corrections (Figure 4.9(a)). For the FM mesh, the analyses using B or BC corrections led to lower residuals than that using C correction only (Figure 4.9(b)). This difference in general trend is confirmed in Figure 4.9(c). Because more degrees of freedom are available for BC corrections with respect to B or C corrections, the residuals could be reduced more significantly. However,

the results for BC corrections are very close irrespective of the number of degrees of freedom.

In Figure 4.9(c) the residuals obtained with both discretizations used for the BCCs are compared. The results are close to the 45° line. The FM discretization performs better when applied with correction B than with C in which the results lie above the 45° line. It can be a consequence of the coupling between C corrections and the underlying kinematics because the same mesh is used for both of them. Besides, BC corrections performed equally well with the 2 discretizations. The fact that the residuals remain close allows the global BCC correction with a single Q8 element to be validated in addition to the FM discretization.

The same comparison procedure and permutation of images of set #1 was used to study the standard displacement uncertainties, which are reported in Figure 4.10. The horizontal component of the nodal displacements will only be reported since the same levels were found for the vertical component. The small level is a result of acquiring the images at the very beginning of the experiment, before crack network initiation (*i.e.,* it allows for an estimation of the noise-floor levels). Further, the short time intervals (*i.e.,* 10 s) between acquisitions reduce the amount of drift that may occur. Thus, in addition to acquisition noise, brightness differences (due to illumination variations) are the main source of displacement fluctuations for image set #1. The standard deviation of nodal displacements was computed thanks to the 81 analyses, and then averaged over all considered nodes for various corrections.

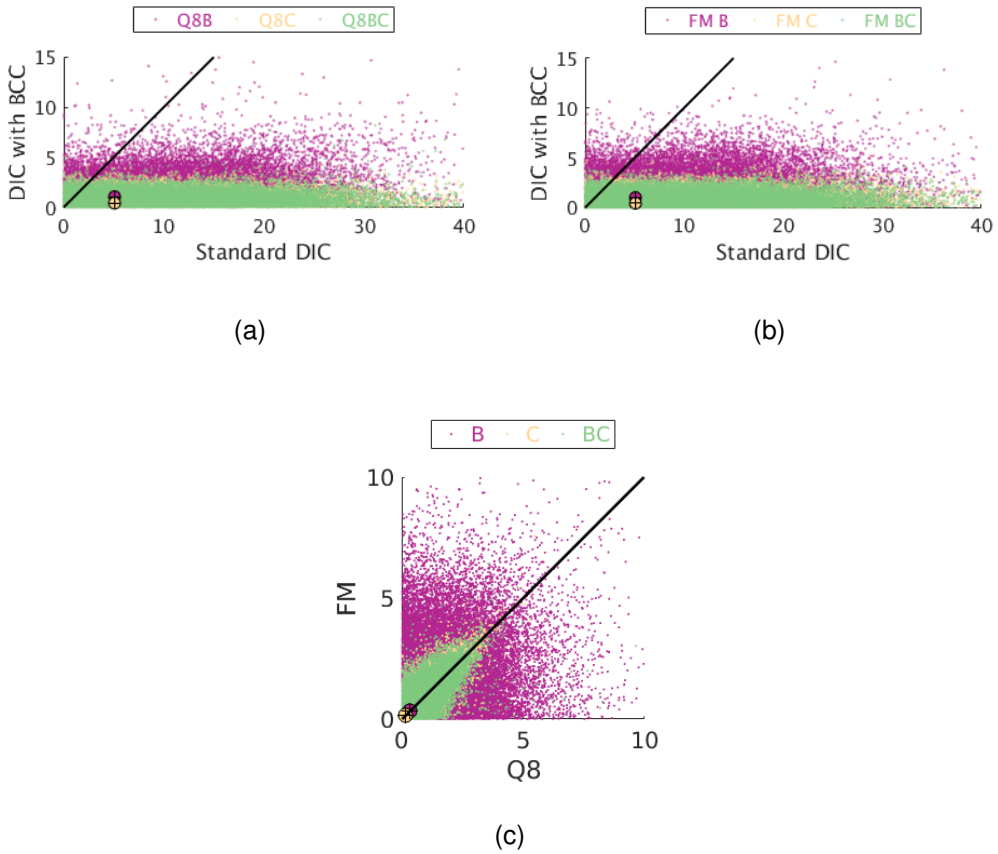

Figure 4.10: Standard nodal displacement uncertainty (expressed in cpx) for each correction: brightness (B), contrast (C), as well as brightness and contrast (BC). The corrections were applied using different discretizations: (a) Q8 element, (b) fine mesh (FM). (c) Comparison between the two discretizations. The circled crosses depict the mean level of each case

Figures 4.10(a-b) show that there is a significant reduction (*i.e.,* one order of magnitude) in standard displacement uncertainty for any of the applied corrections and the two discretizations in comparison to standard DIC. In the present case, the C and BC corrections are more effective than B corrections (Figure 4.10(c)). Such observations apply to both discretizations. The fact that the gray level residuals could be reduced in addition to achieving lower displacement uncertainties validates the BCC procedures in the present experimental configuration.

The case study discussed herein consists of monitoring and quantifying cracks induced by curing and drying. Therefore, the maximum principal strain field is

one of the essential quantities to analyze since it can be related to the crack opening displacement [17, 154]. With the selected (*i.e.,* T3) elements, the strains are uniform over each element. These values are considered with no filtering, and the in-plane principal strains are computed, of which the maximum level is selected since cracks will be detected with this quantity [39].

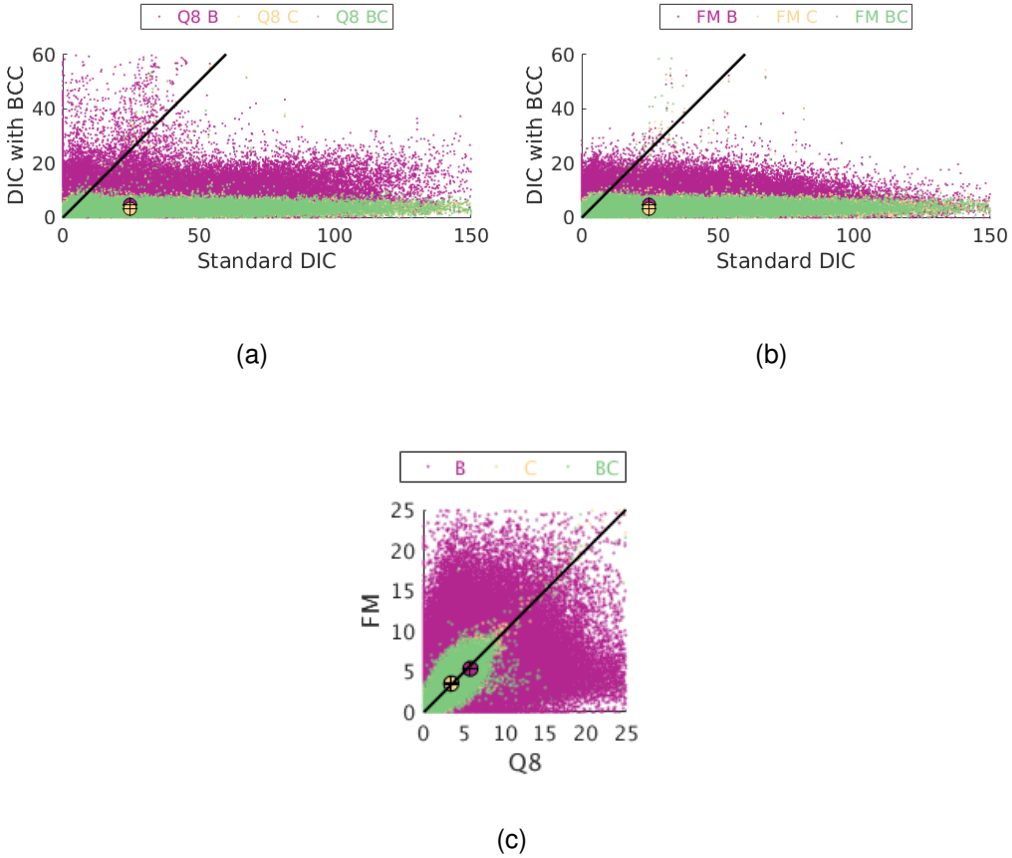

Figure 4.11: Standard deviation of the maximum principal strain (expressed in ‰) for each correction type: brightness (B), contrast (C), brightness and contrast (BC). The corrections were applied using different meshes: a) Q8, b) FM, and c) comparison between the two discretizations. The circled crosses depict the mean level of each case

The general trends are very close to those observed with displacement data (Figure 4.10) since strain uncertainties are proportional to displacement uncertainties [94].

The previous results are summarized in Table 4.1. For both discretization

studied herein, the BC correction leads to the lowest gray level residuals. For the displacement and strain uncertainties, the coarse discretization provides slightly lower levels. This observation means that, in the present case, the increase in degrees of freedom (FM) is irrelevant for the gray level variations, which uniformly affect the surface of interest, and the Q8 discretization is sufficient. The latter has a scale separation with the kinematic basis that will avoid couplings between the two steps of the registration procedure.

Table 4.1: Normalized root mean average of gray level residuals (ϕ), standard displacement (u_x) uncertainty, and corresponding levels for the maximum principal strain (ϵ_1)

DIC Analyses	RMS(ϕ) [%]	std(u_x) [cpx]	std(ϵ_1) [‰]
Standard	2.4	5.1	30.6
Q8 B	1.0	1.1	5.8
Q8 C	0.6	0.4	3.4
Q8 BC	0.6	0.4	3.4
FM B	0.6	1.0	5.4
FM C	0.9	0.5	3.5
FM BC	0.5	0.4	3.6

4.4.2 Applying BCC to curing and drying experiment

The BCC procedure was applied to image set #2 during curing and drying of the refractory cube (T50-H50-F1c) . The meshes and the DIC parameters were the same as those used in set #1 (Table 3.4 and Figure 3.3). The gray level residual $\phi_{\{\boldsymbol{v}\}}$ and maximum principal strain fields obtained with standard DIC (*i.e.,* no BCC) are shown in Figure 4.12 for the last acquired image of the experiment (*i.e.,* when the crack network is the most developed). Both fields show the presence of cracks. They appear as high absolute gray levels in the residual field because they do not satisfy displacement continuity and new gray levels are created by their opening. The elements located on the cracks lead to a high value of maximum principal strain (Section 4.3). Both fields are grainy, which indicates the presence of “noise” affecting them.

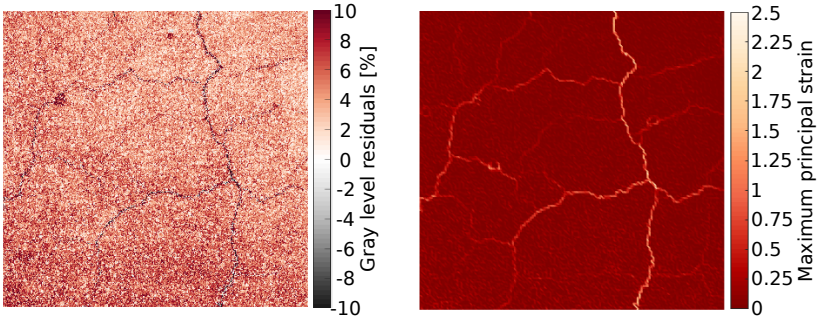

(a) Standard DIC residuals (b) Standard DIC ϵ_1

Figure 4.12: Gray level residuals (a) and maximum principal strain (b) fields for the last image acquired during curing and drying of the refractory cube using standard DIC

Figure 4.13 shows the gray level residual fields ϕ_{bcc} when BCCs are applied. The use of B and BC corrections for Q8 and FM discretizations significantly reduced the "noise" of the residual field, when the BCCs results are compared to the standard DIC one (see Figure 4.12). Also, the regions without cracks presented very low levels $\approx$ 0.05% (Figures 4.13(a, b, e, and f)). When only C corrections were applied, both Q8 and FM results induced gray level residual fields similar to that provided by standard DIC. These fields are very grainy, which makes the larger cracks barely distinguishable (Figures 4.13(c and d)) for both discretizations.

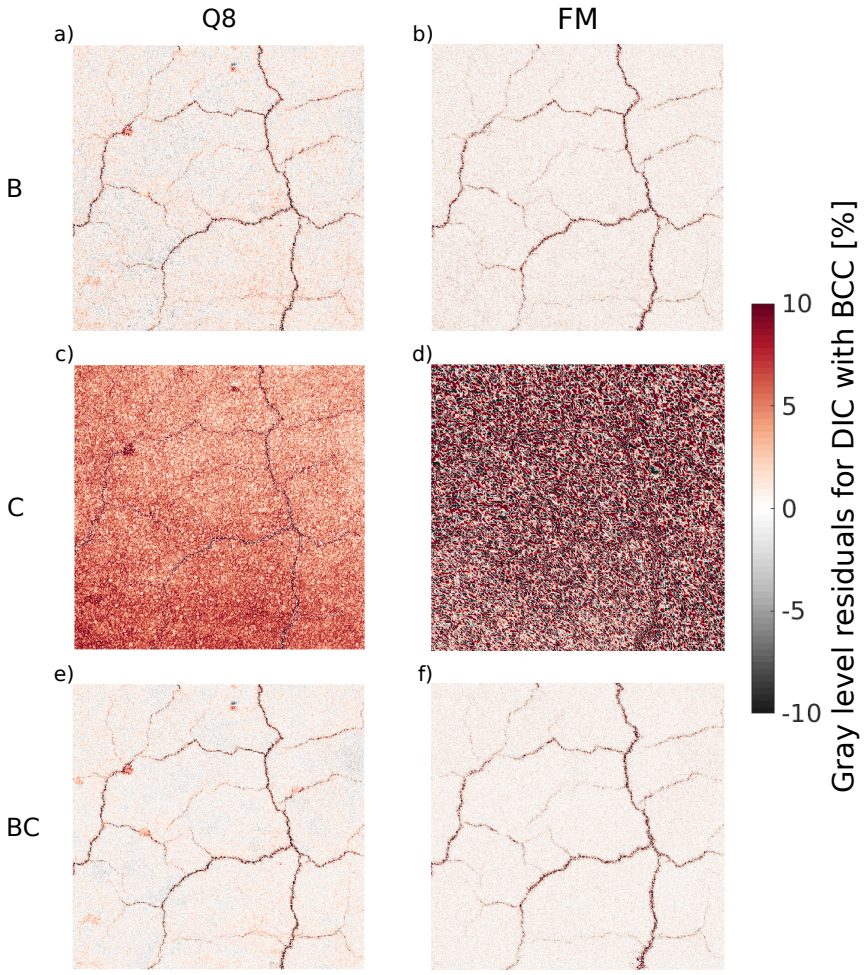

Figure 4.13: Normalized gray level residuals for the last image captured during curing and drying when three corrections: brightness (B), contrast (C), brightness and contrast (BC) were carried out with two discretizations (Q8 and FM)

Pores are areas with low contrast, *i.e.,* regions with uniform dark gray pixels due to the shadow formed by the depth of these artifacts (Figure 3.3), which may be considered as defects and corrected by the BCC procedures. Besides, the cracks create new gray levels during their opening, as mentioned herein, which makes them an additional source of gray level variation. However, the cracks caused by MgO hydration and their quantification are the main objective for the present case study. If the corrections affect the detection of cracks, it is important to check the effect of BCCs on their representation. One can notice that the Q8 discretization shows high values of gray level residuals in porous regions (*i.e.,* $\approx$ 5%), for B or BC corrections. However, the residuals are low for the same regions in the FM results ($\approx$ 0.5%), which means that the FM can correct such

effect thanks to the high number of nodes, and the element size close to the pore one (Figure 3.3), *i.e.,* enough degrees of freedom (80,000 for FM BC). Conversely, the FM correction spreads the gray level residuals in the cracked regions. It may compromise the evaluation of the crack positions. The effect of smeared residuals around cracks is reduced in the Q8 results because of the minimal number of degrees of freedom (16 for Q8 BC) that ignores the effect of the pores, and also reduces the issue in crack detection.

The results obtained by different BCCs are further compared using histograms of gray level residuals (Figure 4.14). The histograms for C corrections using both discretizations are close to the standard DIC result. The FM C case increased the range of gray level residuals by $\approx$ 30%, thereby showing a lower quality of the results. Such effect is due to the coupling of contrast correction and the kinematic, which should be avoided [93]. The other corrections (*i.e.,* B and BC) resulted in distributions centered about zero for both discretizations, which are significantly lower for the FM one. This shape is expected for the standard acquisition noise, which usually is white and Gaussian as a first approximation [93]. Further, there are many pixels close to zero gray level residuals that correspond to regions without cracks (clusters of aggregates). Comparing B and BC results for both discretizations, B resulted in slightly wider distributions because it uses two times fewer degrees of freedom.

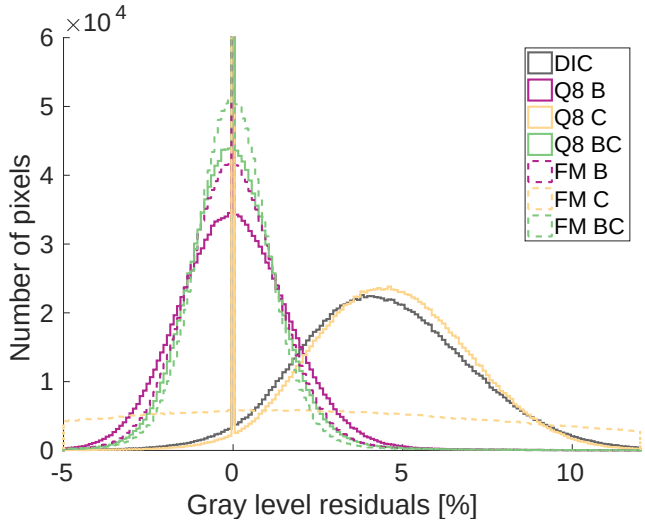

Figure 4.14: Histograms of gray level residuals for all BCC procedures tested herein using the last image of the experiment ('DIC' refers to standard DIC)

The frame-wise RMS of the gray level residuals is reported for the image set #2 (entire experiment) in Figure 4.15. The standard DIC result is related to various sources of gray level changes such as lighting and vapor stream. The C correction performed poorly compared to B and BC. Further, the FM C analysis randomly increased the fluctuations in different frames. In the present case, such corrections should not be used. Conversely, the RMS residuals were significantly reduced with B and BC corrections, from an average RMS of 5% for standard DIC to 1.5% for B and BC corrections. Last, the RMS levels start to increase after 18 hours for all corrections. This trend is related to the opening of numerous cracks (*i.e.,* they are one source of gray level residuals even when corrections with many degrees of freedom –FM B and FM BC– are used).

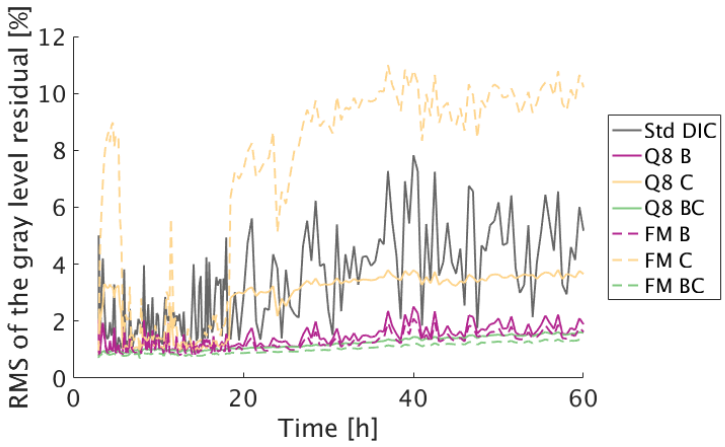

(a) All analyses

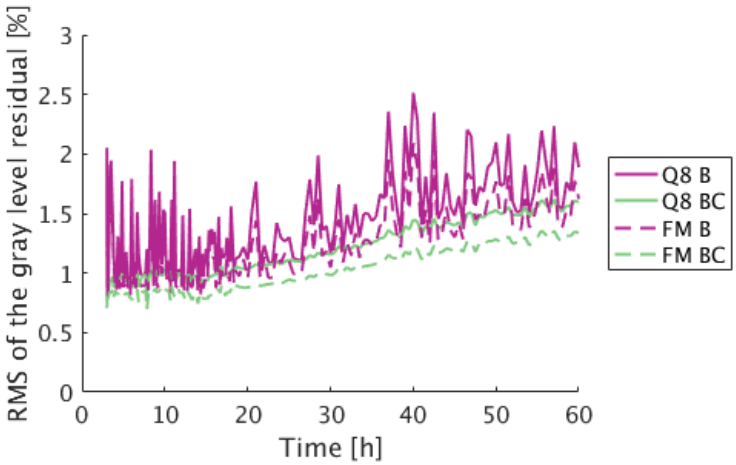

(b) Detail of the sets of parameters with smallest RMS residuals

Figure 4.15: RMS residuals for the six BCC analyses. The BCC using coarse or fine discretizations reduce the residual levels when compared to standard DIC

In Figure 4.15(b), the three cases with higher RMS of residuals (*i.e.,* standard DIC and C corrections with both discretizations) are excluded to make easier the comparison between B and BC results. The BC correction for Q8 and FM reduced the residuals, and increased the difference between the results of the two discretizations for B, which indicates that BC is more sensitive to the mesh type than B. However, the mean difference of RMS residuals between B and BC corrections remains small (*i.e.,* $\approx$ 0.5% of the dynamic range).

The maximum principal strain ϵ_1 fields for the last image of the experiment were obtained using all BCC procedures (Figure 4.16). The levels of ϵ_1 are uniform, mainly for B and BC corrections and close to zero in cluster regions, which is different for the grainy fields obtained using standard DIC (see Figure 4.12(b)). The zero strain regions are expected because the MgO hydration is a heterogeneous expansion that occurs in the matrix of the castable [155]. The B and BC corrections allowed small cracks to be detected (*i.e.,* elements with low ϵ_1 levels), which were more difficult to spot in standard DIC results. Further, the effect of the pores mentioned in the gray level residuals is not observed in the strain fields for the cases using the FM discretization. The latter erases spurious gray level variations caused by the pores. However, they may lead to higher strain level, which would be considered as cracks in some analyses, such as the crack density 4.5.1, and thereby reduce the accuracy of the damage evaluation.

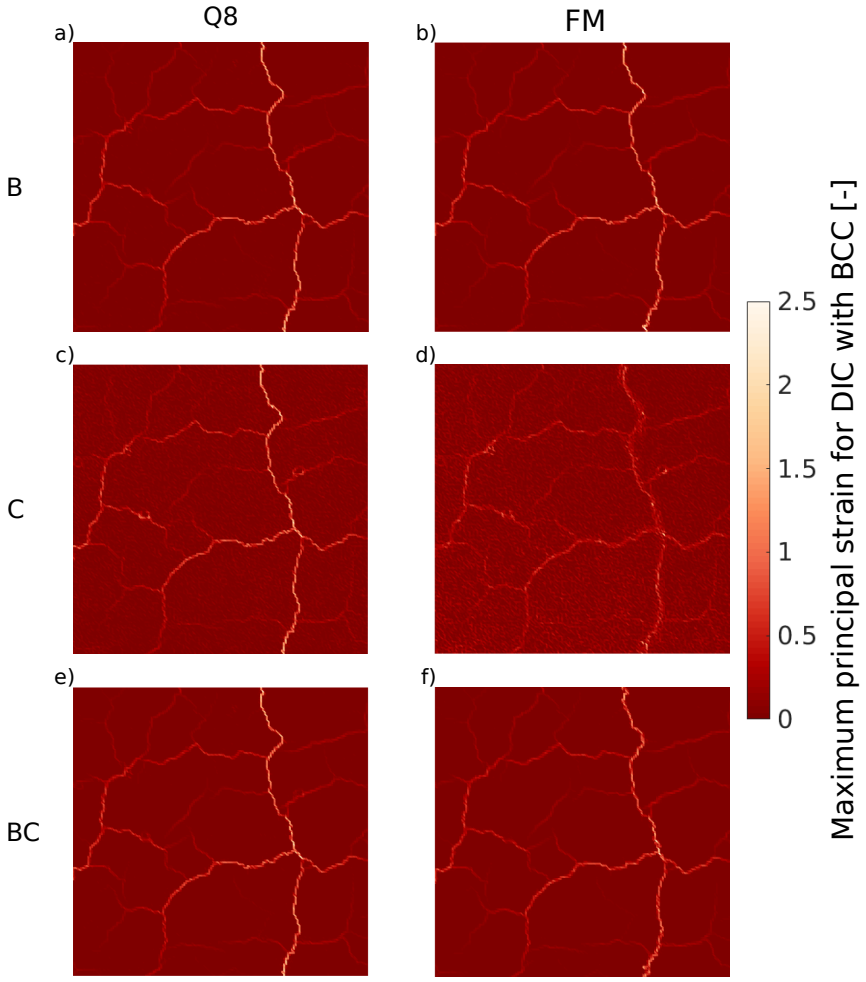

Figure 4.16: Maximum principal strain field for the last image acquired during the experiment using the corrections: brightness (B), contrast (C), brightness and contrast (BC), carried out with two discretizations (Q8 and FM)

The BCCs reduced not only the effect of the pores but also that one of the cracks, which are localized sources of gray level changes. This phenomenon causes the appearance of elements with very small ϵ_1 in the crack path as if the BCCs tried to close the cracks. It is mainly relevant for corrections using FM because this discretization has more degrees of freedom that enable BCCs to act in localized segments of the surface of interest. FM C corrections resulted in a grainy field caused by their coupling with the underlying kinematics. The FM B and FM BC routes led to similar ϵ_1 fields, except for the apparent wider cracks in FM BC and their levels smaller than the FM B results. To make the comparison easier between the fields of a pair of BCCs, their differences $\Delta\epsilon_1$ are reported in Figure 4.17.

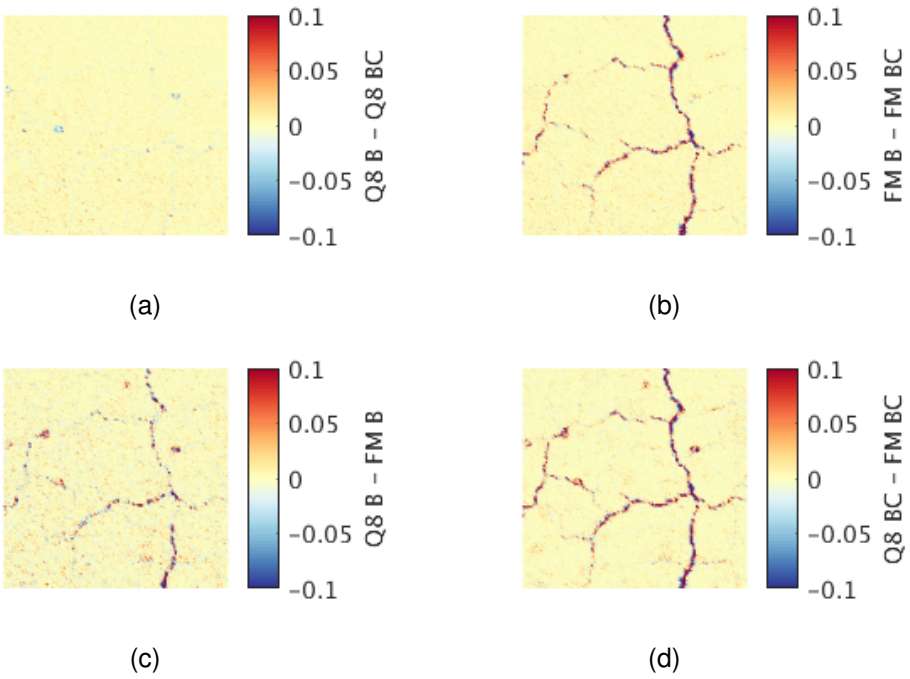

Figure 4.17: Difference of maximum principal strain fields $\Delta\epsilon_1$ between: (a) Q8 B and Q8 BC, (b) FM B and FM BC, (c) Q8 B and FM B, and (d) Q8 BC and FM BC to show how different corrections affect the cracks. The range of the color map was reduced to improve the contrast

As the case study discussed in this section concerns the monitoring of open cracks, it means that the maximum principal strain ϵ_1 is always positive. This feature is useful to distinguish the effect of each BCC by the level in the $\Delta\epsilon_1$ fields of Figure 4.17. For example, in Q8 B - Q8BC $\Delta\epsilon_1$ (Figure 4.17(a)) the blue artifacts are due to Q8 BC, because it represents negative values in the color map. These artifacts are pore effects that were better corrected by Q8 B than Q8 BC. In the strain difference FM B - FM BC, no pore effect is observed in Figure 4.17(b). However, they can be seen in red in Figures 4.17(c-d), and are attributed to Q8 B and Q8 BC, respectively. These results confirm the hypothesis that the FM procedures correct the pore effects, but the Q8 ones do not. Such feature of the FM procedures is due to the localized effect of the corrections provided by the higher number of degrees of freedom (*i.e.,* 40,000 for B and 80,000 for BC corrections).

The effect of the BCCs on the crack opening (or equivalently on the strain fields) is analyzed in the sequel. In Figure 4.17(b), a red crack path due to FM

B is mostly surrounded by blue levels provided by FM BC corrections. Red crack paths (Figures 4.17(c-d)) are due to Q8 corrections, which do not have a localized effect, as observed for correcting the pore effects. The paths are surrounded by the same blue artifacts, which are due to FM B and FM BC corrections that spread the gray level residuals and, consequently, reduce the ϵ_1 levels in the main paths and increase it in some adjacent elements.

Histograms are also used to compare different distributions for the maximum principal strain fields (Figure 4.18). The vertical axis is represented in logarithmic scale to make possible the visualization of the number of elements with a high ϵ_1 level. Similar to the histograms obtained for the gray level residuals, the C corrections, mainly the FM C, are not efficient since they are close to the strain distributions of standard DIC. The other corrections led to distributions with a higher number of elements in low and high strains than the standard DIC, *i.e.,* there is a clear separation of cluster zones ($\epsilon_1 \approx 0$) and cracks (high ϵ_1). Moreover, the distributions are very similar for B and BC corrections using both discretizations. Large crack openings led to deviations, mainly for the FM BC, which showed fewer elements in high ϵ_1 because this procedure has a strong localized effect and corrects the increase in gray level residuals due to cracks.

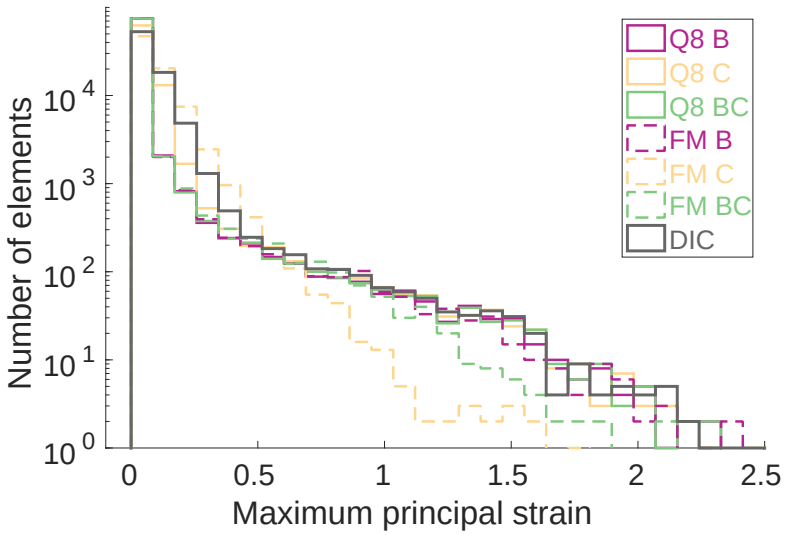

Figure 4.18: Histograms of maximum principal strain for all BCC procedures using the last image of the experiment

The mean and standard deviation of maximum principal strains are plotted as a function of time (Figure 4.19). As expected from the previous analyses, the C corrections are very close to standard DIC throughout the whole history. They are fluctuating in time a lot more than the other corrections, which are consistent for both reported quantities. The differences between the various corrections are more important on the mean levels of ϵ_1 than on its standard deviation. This observation proves that when the corrections are not optimal, the mean ϵ_1 is over-estimated.

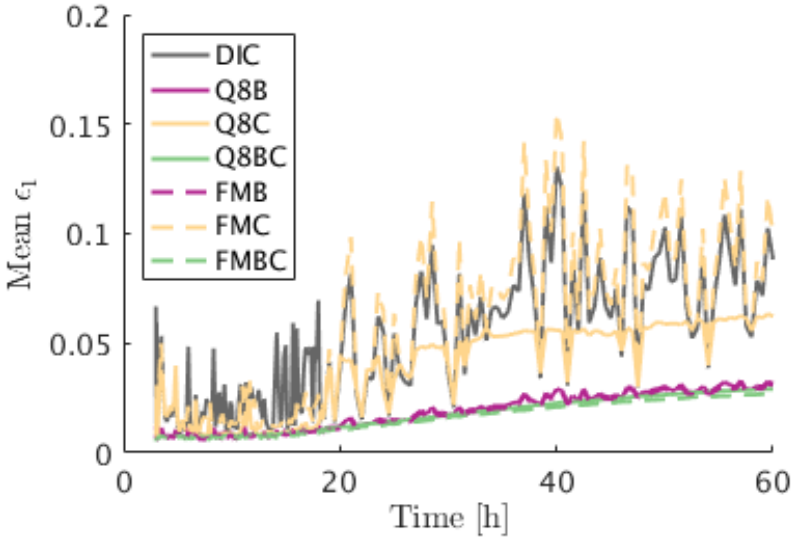

(a)

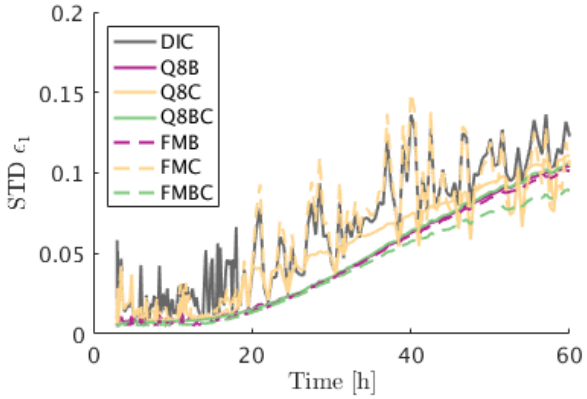

(b)

Figure 4.19: Evolution of mean (a) and standard deviation (b) of maximum principal strain during 60 h of curing and drying

By considering all the previous results, it is concluded that only the contrast correction is not advisable as it led to results very close to those with no correction at all (*i.e.,* standard DIC). The brightness and contrast correction is the best type (as it lowers the residuals the most) even though the brightness correction alone also gave good results. The small number of DOF required with one Q8 element makes it a good choice for the discretization influence.

4.5 Evaluation of damage caused by MgO hydration using MCOD

DIC monitoring does not require any physical contact as for IET, which makes it likely to be *in situ* applied. As mentioned, one benefit of DIC analyses is the increase in the amount of gathered data related to damage effects on the surface of the analyzed samples, exemplified by the mean crack opening displacement (MCOD) fields shown in Figure 4.20.

The MCOD fields are localized, which indicates crack networks, with no sign of a predominant crack (Figure 4.20). This result implies that there are no significant boundary effects, and the assumption of an RVE for the cube-shaped specimens is valid. Further, one can notice a good match between the top and front faces cracking for the same specimen, in particular for the common edge between the two surfaces. For an illustration and validation of the MCOD procedure, see Section 4.6.

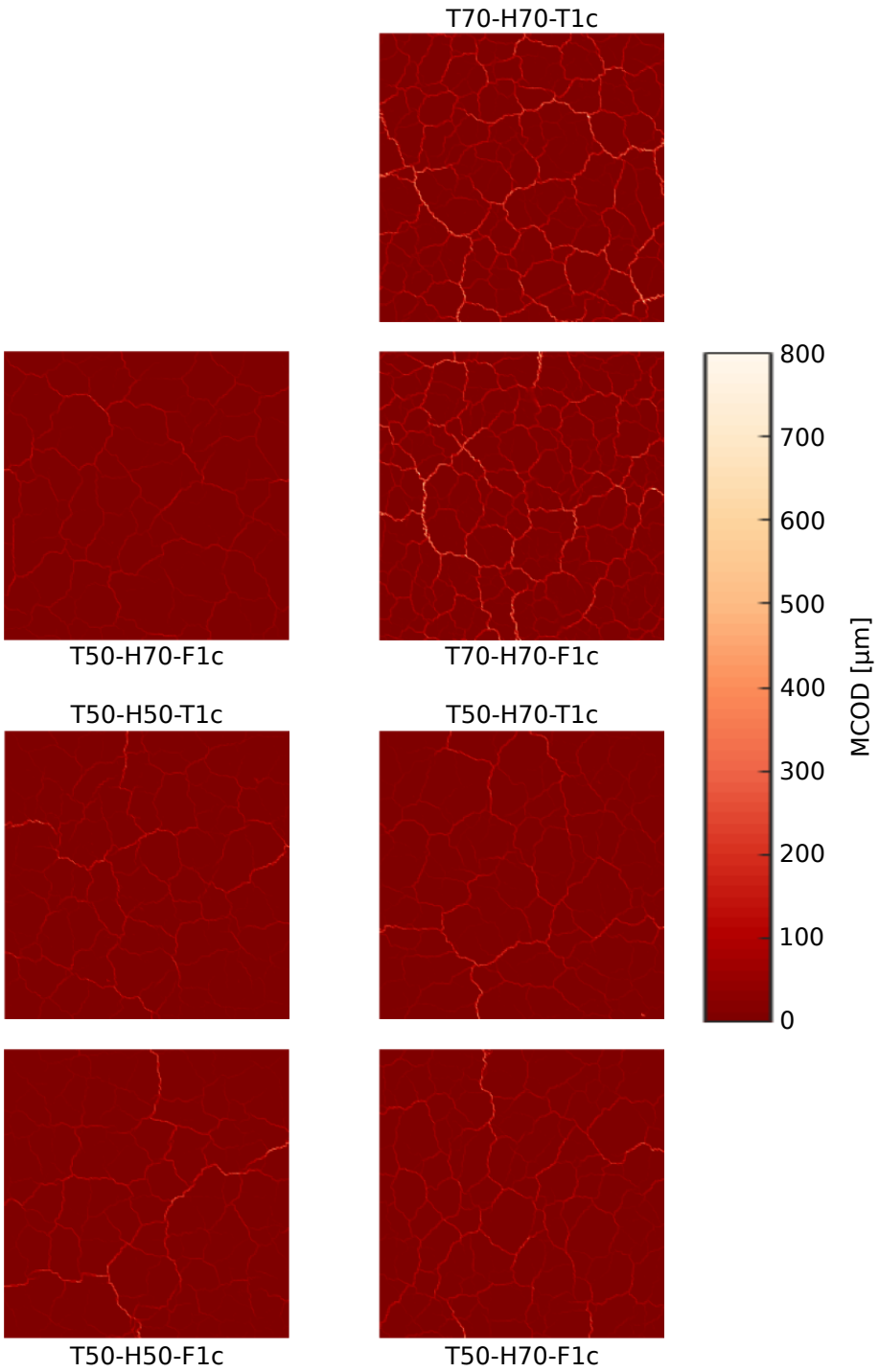

Figure 4.20: Mean crack opening displacement (MCOD) fields for top and front surfaces for four cubes tested at combinations of parameters, such as 50 and 70 ℃, and 50% and 70% of relative air humidity. The fields were obtained for the 60-hour (*i.e.,* last) frame using a ROI of $\approx 60 \times 60$ mm^2. Technical issues hindered the evaluation of T50-H70-T1c fields

Figures 4.21 ($T = 50$ ℃) and 4.22 ($T = 70$ ℃) show the histograms and associated cumulative frequencies for the last acquired image (after 60 h) for all ana-

lyzed tests. Overall, there is a good reproducibility among different experiments at the same temperature and among face features for the same experiment.

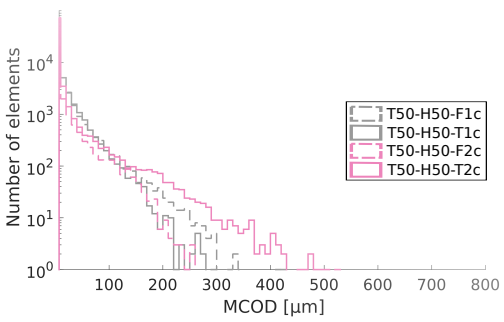

(a) Histograms (T = 50 ℃ H = 50%)

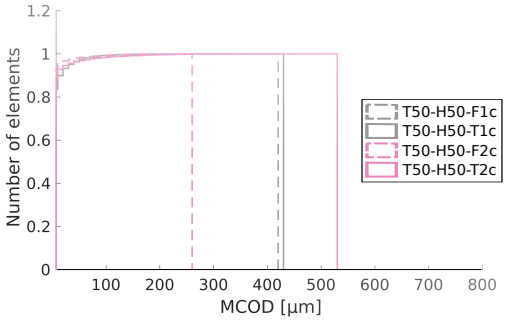

(b) Cumulative frequency (T = 50 ℃ H = 50%)

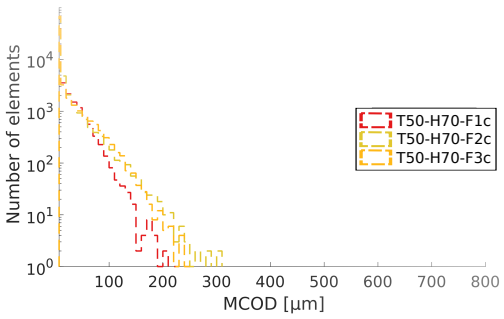

(c) Histograms (T = 50 ℃ H = 70%)

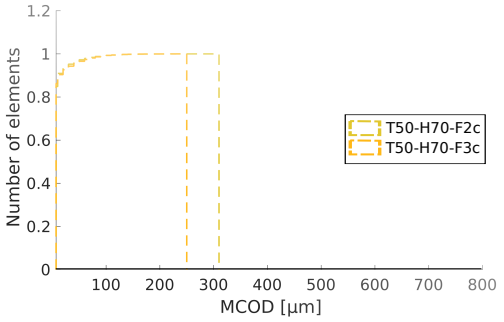

(d) Cumulative frequency (T = 50 ℃ H = 70%)

Figure 4.21: Histograms of the MCOD (a and c) and their corresponding cumulative frequencies (b and d) for 50 ℃ and different humidity values.

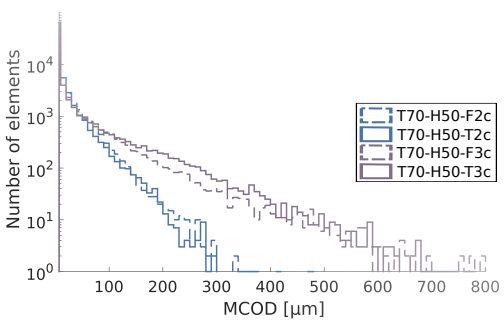

(a) Histograms (T = 70 ℃ H = 50%)

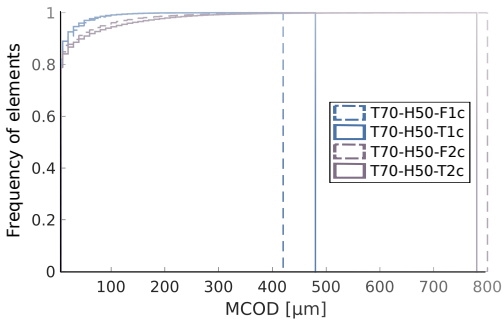

(b) Cumulative frequency (T = 70 ℃ H = 50%)

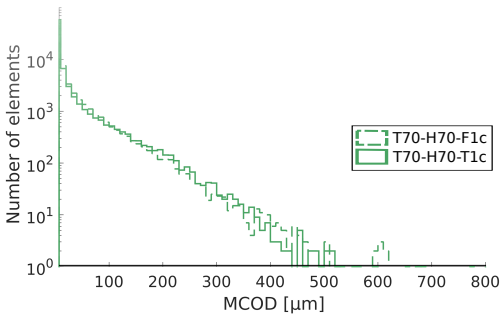

(c) Histograms (T = 70 ℃ H = 70%)

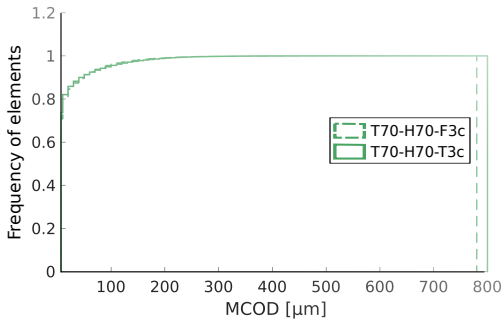

(d) Cumulative frequency (T = 70 ℃ H = 70%)

Figure 4.22: Histograms of the MCOD (a and c) and their corresponding cumulative frequencies (b and d) for 70 ℃ and different humidity values

The average MCOD and corresponding standard deviations after 60 h are reported in Table 4.2. The fluctuations are very high (when compared to the mean levels), which is a further indication of a very wide distribution of MCODs. Further, the rise of temperature increases the average and the STD of MCOD.

Table 4.2: Average MCOD values and STD for the final frame after 60 h of experiments

Specimen designation	Average MCOD [μm]	Standard Deviation (STD) [μm]
T50-H50-F1c	8.3	20.8
T50-H50-T1c	8.3	17.6
T50-H50-F2c	4.5	15.0
T50-H50-T2c	8.6	26.3
T50-H70-F1c	6.6	14.5
T50-H70-F2c	8.1	18.2
T50-H70-F3c	7.9	18.9
T70-H50-F1c	10.0	21.5
T70-H50-T1c	9.1	19.8
T70-H50-F2c	16.8	46.9
T70-H50-T2c	19.7	53.4
T70-H70-F1c	18.4	39.8
T70-H70-T1c	18.3	41.1

Aiming at studying frame by frame the development of damage during curing and drying of the studied castable, the STD and the average of MCOD are shown in Figure 4.23. The first remarkable difference is that damage increase is higher at 70℃ when compared to 50℃ , in which no saturation is observed after 60 h. The role of temperature mentioned above is confirmed by the curves of average MCOD. The effect of increasing the relative air humidity is inconclusive and more tests are needed. Second, all average MCODs are less than 1 pixel (50 µm), which shows that the sub-pixel resolution of DIC was crucial to properly quantify damage in such materials in which crack openings remain very small. Both average MCOD and STD show that there are differences for two faces of some experiments, and for different temperatures. This can be due to microstructural effects, *e.g.,* different large and small aggregate ratio, and inhomogeneities in the surface temperatures.

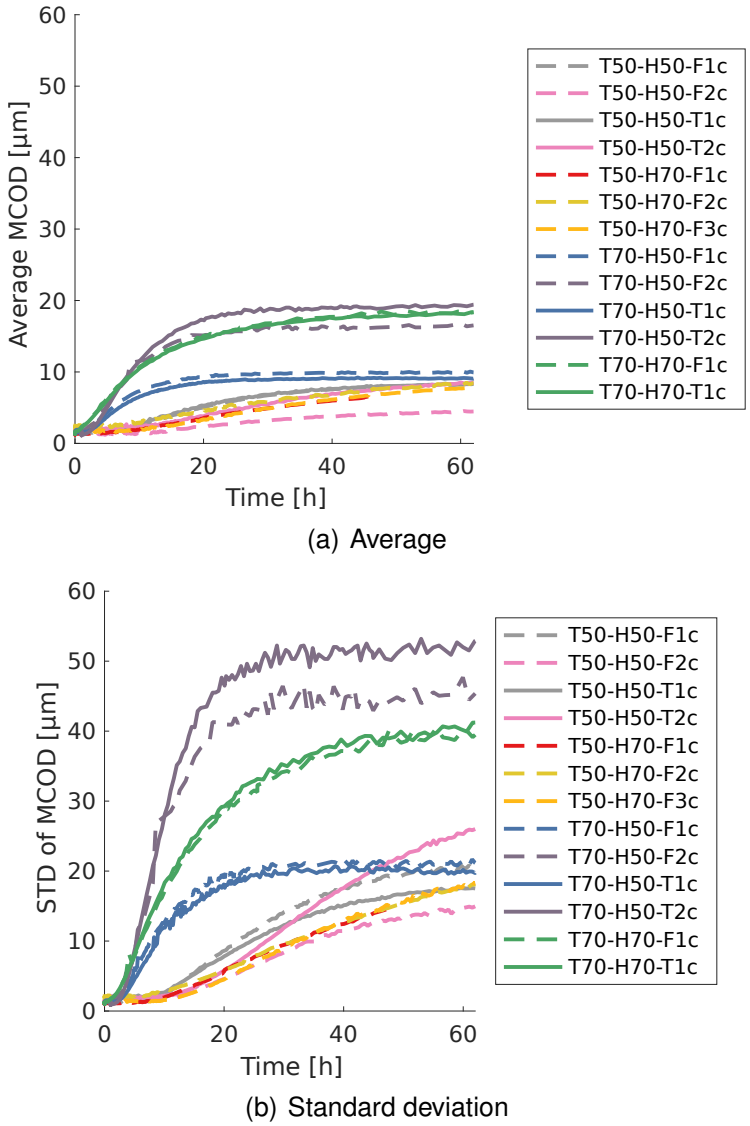

(a) Average

(b) Standard deviation

Figure 4.23: Average (a) and STD (b) of MCOD for the cubic specimens at different temperatures and relative air humidity.

4.5.1 SCD to evaluate damage growth

DIC results obtained for cube-shaped specimens at different temperatures for an 300 µm (*i.e.,* 6 px) element size, are compared. The first step to compute the Surface Crack Density (SCD) is to exclude the strains caused by hydration expansion, for example, defining a strain threshold ϵ_1^*. For this step, ten images taken at the very beginning of each experiment (set #1) were used to obtain the average of all STDs of the maximum principal strain $\sigma(\bar{\epsilon}_1)$, which is a quantity that is computed at the scale of the elements. The standard uncertainties are shown in Table 4.3

Table 4.3: STDs of the maximum principal strain $\sigma(\bar{\epsilon}_1)$, values of ϵ_1^* and the referent MCOD for each experimental condition. Values averaged over surfaces and experiments repetition

Experimental condition	$\sigma(\bar{\epsilon}_1)$ [1×10^{-3}]	A	ϵ_1^* [1×10^{-3}]	MCOD [μm]
T50-H50	5.4	5	27	8.1
T50-H70	4.4	5	22	6.6
T70-H50	3.7	5	18	5.4
T70-H70	4.0	5	20	6.0

The average ϵ_1^* was 2.2×10^{-2} (*i.e.,* MCOD = 6.6 µm) with a standard deviation of 3.9×10^{-3} (*i.e.,* MCOD = 1.2 µm). The fluctuations among experimental conditions can be considered small since this is a ceramic system. This observation indicates that ϵ_1^* depends on the material not on the temperature and relative air humidity, which is expected because damage initiation occurs after stresses generated by the formation of brucite surpass the mechanical strength of the material, and the external variables dictate the velocity in which this condition will be achieved.

The second step is to include in ϵ_1^* the strains related to the expansion of the MgO containing phases before damage inception. Such inclusion is made using a factor A defined by the user. The effect of different values of A (varying from three to seven) on the SCD is shown in Figure 4.24(a).

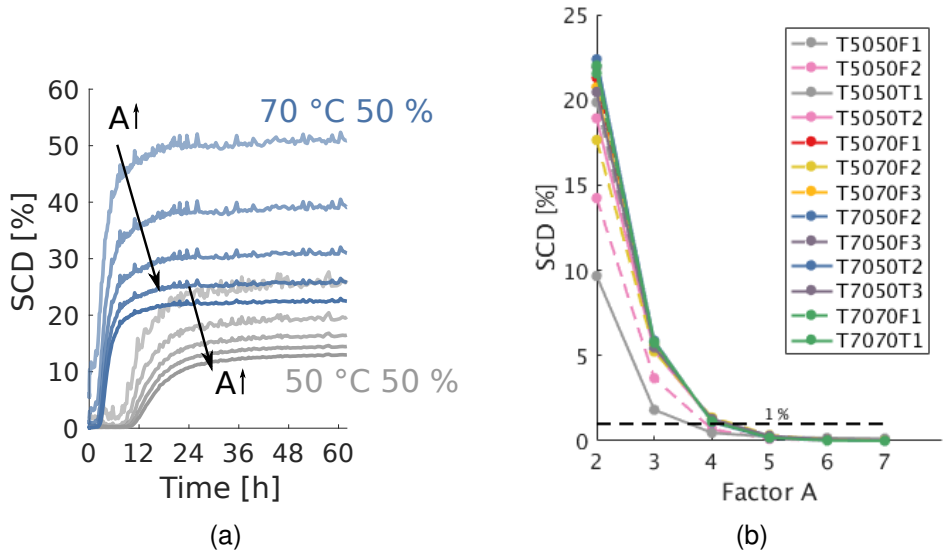

Figure 4.24: Surface crack density histories as functions of parameter A (see (b) for sample color code). (a) SCDs for the top surface of cubes tested at 50℃ and 70℃ (humidity 50%) using different values of A to estimate the ϵ_1^* threshold (samples T50-H50-T1c and T70-H50-T2c). (b) Mean value of SCD for the 10 initial images of each experiment to estimate A. The black dashed line indicates the selected level

Small A values result in an initial crack density at the beginning of the experiments before actual crack initiation (Figure 4.24(a)). Conversely, high A values lead to a decrease of the SCD, mainly at the end of experiments. It is not possible to estimate a specific level for damage at the end of the tests because it depends on A. However, one can state that the damage level for the castable tested at 70℃ is higher than at 50℃ (50% of humidity) for all considered A values (Figure 4.24(a)). The mean SCD for the initial 10 images of each experiment was computed to help to choose the most suitable A parameter (Figure 4.24(b)). A high A factor can flatten the curve profile, which is a pointless condition of no elements being considered damaged and for that reason, the first value of A that resulted in mean SCD values less than 1% for the set #1 images was selected, *i.e.,* $A = 5$ (Figure 4.24(b)).

The thresholds ϵ_1^* and the corresponding MCODs are shown in Table 4.3. The SCD for the surfaces of the cubes evaluated at all experimental conditions are shown in Figure 4.25. The change of the SCD follows a logistic curve (sigmoidal shape), similar to those for the MgO hydration kinetics obtained by other tech-

niques [3, 82, 155], *cf.* Figures 2.3 (page 14) and 2.4 (page 15). The increase in temperature speeds up the hydration kinetics, the SCD onset, and the final damage levels are achieved earlier and are higher for the experiments carried out at higher temperatures. The increase in relative air humidity has a tenuous effect in the sense of speed up the reaction, which becomes more relevant for higher temperatures. The reproducibility of the results for analogous surfaces is very good and validates the experimental protocol.

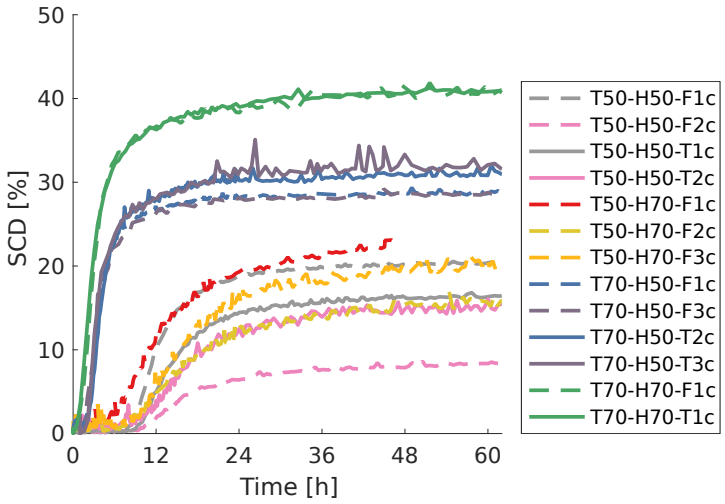

Figure 4.25: Surface crack density obtained by DIC during brucite formation in cube-shaped specimens. the experimental conditions are depicted in the legend

The overall trends of Figures 4.23 and 4.25 are similar, namely, after an initial incubation time, all quantities start to increase rather fast and then tend to saturate. However, the characteristic times associated with such phenomena are different for SCD and MCOD data. The former saturates faster than the latter. This observation shows that many cracks are generated at the beginning of the damage process, growing fast on the surface, and then saturating in terms of their number. However, this situation does not mean that the damage process ceased. The fact that MCOD data still increase means that the crack openings augment as well, which may indicates that in-depth propagation still occurs, leading to larger crack openings on the surface. This observation is confirmed by the results in Figure 4.3 that show gradual in-depth propagation. Further, the number of generated cracks may be related to the temperature since the SCD

values for specimens tested at T70-H50 are very close and saturated at ≈ 30%, whereas for others tested at T50-H50 there is a higher variation of SCD data and the saturation can be estimated at ≈ 15%. The effect of relative air humidity at the saturation SCD is weak for 50 °C and stronger at 70 °C with a saturation SCD of ≈ 40%. However, the temperature is related to the onset of SCD, namely, ≈ 12 h for tested carried out at 50 °C and ≈ 3 h for the others carried out at 70 °C.

4.5.2 Comparison between IET and DIC

The bar-shaped specimens used for DIC analyses are designated as T50-H50-T1b and T50-H50-T2b, and those for IET, T50-H50-3b and T50-H50-4b. The four samples were produced from the same batch, only cast in different cavities of the silicone mold. The four bars were placed inside the climatic chamber at 50 °C and 50% air humidity. Specimens T50-H50-T1b and T50-H50-T2b were kept there for image acquisition. Samples T50-H50-T3b and T50-H50-T4b were frequently withdrawn from the climatic chamber for carring out IET measuring, which lasted ≈ 30 minutes, and they were kept in the chamber between measurements. The mean element size for these analysis using bar-shaped specimens were ≈ 20 px (≈ 1 mm).

The damage caused by magnesia hydration affects both the Young's modulus (E) measured by IET, as well as the MCOD and SCD obtained by DIC analyses (Figure 4.26). The solid gray line indicates that the onset for Young's modulus decrease matches that of SCD increase, yet the onset of MCOD is more gradual. Conversely, the saturation of MCOD and Young's modulus are very close, whereas that of SCD occurs earlier. The causes of such phenomena are detailed in the discussion of Figure 4.27 hereafter. The reader's attention is directed to the fact that DIC results captured distinct parts of the Young's modulus changes (*i.e.,* fast SCD increase and saturation while MCOD was still increasing), which was not distinguishable by IET. This aspect reinforces the fact that DIC allows further insight into the hydration kinetics and mechanisms.

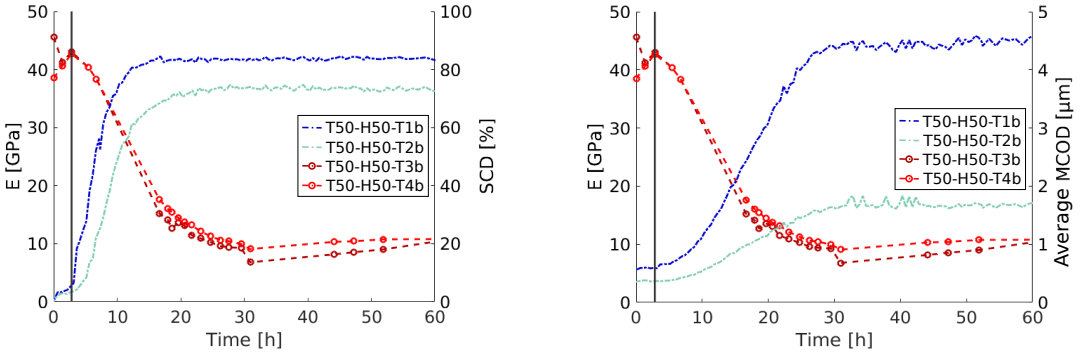

Figure 4.26: SCD (a) and MCOD (b) (specimen designation:T50-H50-T1b and T50-H50-T2b) compared to IET data (specimen designation: T50-H50-T3b and T50-H50-T4b) during the curing and drying of the castable at 50℃ and 50% humidity.

IET and DIC results were compared by plotting the SCD and average MCOD as functions of the macroscopic estimation of damage [156], namely, $D = 1 - E/E_{max}$ were E_{max} is the maximum Young's modulus, as shown in Figure 4.27. For samples T50-H50-T3b and T50-H50-T4b, the Young's modulus changes were very close, as stated in Figure 4.26, and the average value of each measurement was used to compute the macroscopic damage variable D. Conversely, the DIC results (samples T50-H50-T1b and T50-H50-T2b) are plotted separately. In Figure 4.26 the SCD values saturate while the damage parameter continues to increase, which means that the damage growth keeps increasing due to additional crack openings for the same network (*i.e.,* the same number of damaged elements). This result shows that in the present case, macroscopic damage is due to a combined effect of multiple cracking events (characterized by the crack density), and the fact that cracks open more evenly as the network was saturated in terms of crack density. This additional opening displacement is due to in-depth propagation (Figure 4.3).

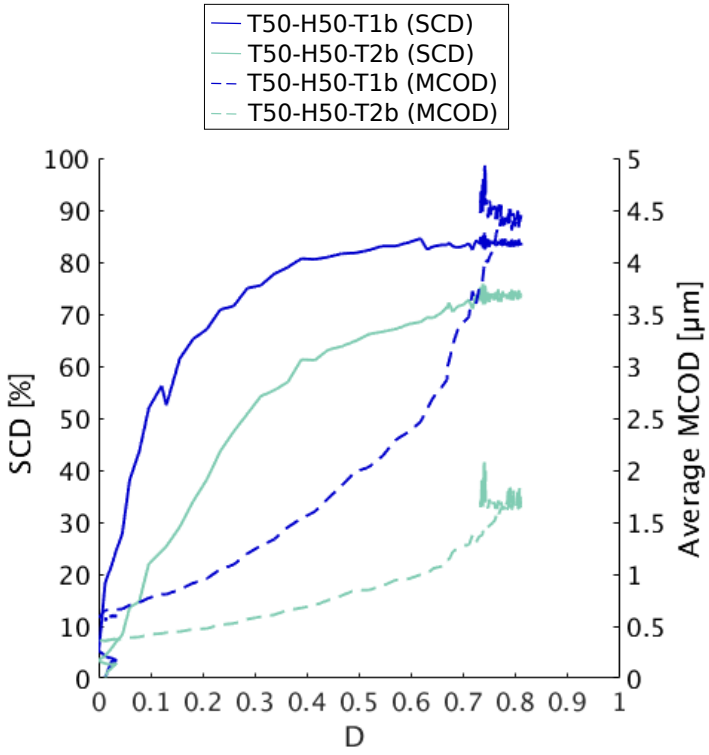

Figure 4.27: SCD and average MCOD for the bar-shaped specimens (T50-H50-T1b and T50-H50-T2b) versus the macroscopic damage D (evaluated from samples (T50-H50-3b and T50-H50-4b).

4.5.3 DIC results for different specimen geometries

In this section, a qualitative comparison between DIC results obtained for both sample geometries is presented. Figure 4.28 shows the MCOD fields for one face of a cubic-specimen (T50-H50-T1c) and one bar-shaped sample (T50-H50-T1b). The mean element size for this analysis using bar-shaped and cubic specimens were ≈ 20 px (≈ 1 mm), which was the best element size for the tests with bars. For the bar-shaped specimen, in agreement with Ref. [17], the main crack was usually generated parallel to its most extended edges (Figure 4.28(a)), which is most likely related to the slender shape of the bars required by IET. This observation does not apply for cube-shaped samples (Figures 4.28(b) and 4.20).

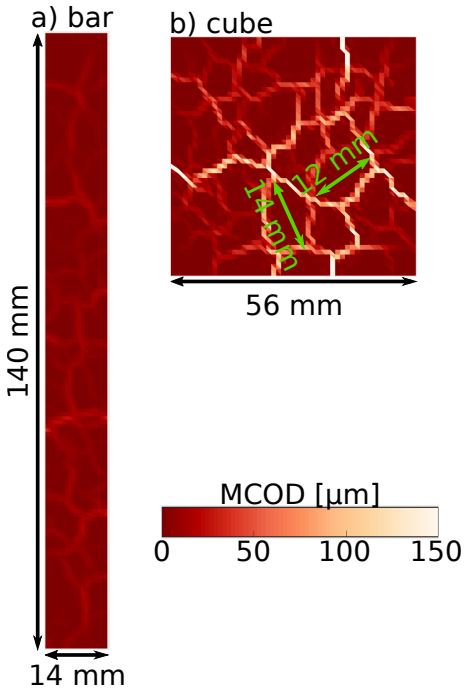

Figure 4.28: MCOD fields for T50-H50-T1b (a) and T50-H50-T1c (b) samples after 60 h in the climatic chamber at 50℃ and 50% air humidity. The color map range was truncated (up to 150 µm) to make the crack openings in the bar-specimen visible

Additionally, the cubic sample displayed higher MCOD levels than the bar-shaped one, which may be related to room available for cracks to growth towards the center of the cube. The size of large clusters presenting MCODs values close to zero on the cube surface, such as those marked with green arrows (12 mm and 14 mm length), have almost the same size as the bar width, which makes the hypothesis of an RVE questionable for bars containing big aggregates (≈ 6 mm).

There is also a clear difference between the average MCOD and SCD profiles when the bar-shaped specimen and the cubic ones (T50-H50 set of samples) are compared under the same environmental conditions (Figure 4.29). MCOD values are significantly smaller for the bar than cubes, whereas the SCD levels are higher for the bar than the cubes. This difference may be attributed to the fact that the bar-shaped specimen is not yet a RVE. Consequently, it is advised to use sample sizes greater than typical RVE ones, which means at least ten times the size of the largest aggregates, to study refractory castable. This observation is an example of the benefits in gathering DIC information.

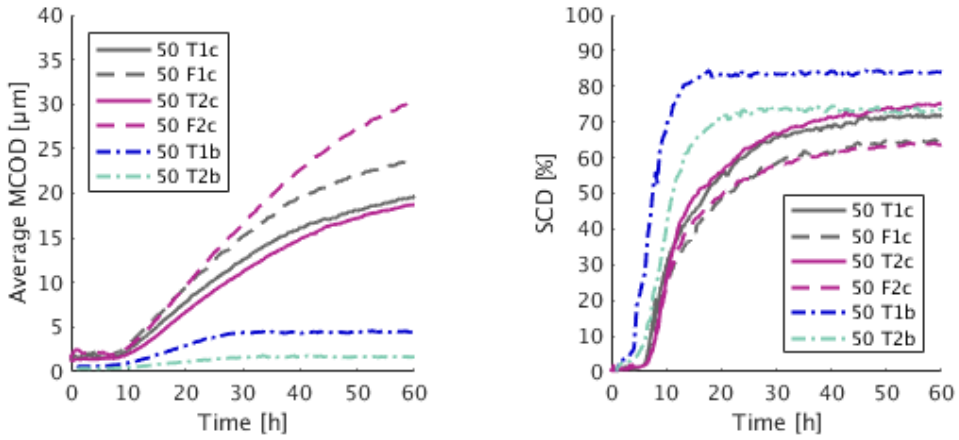

(a) (b)

Figure 4.29: MCOD (a) and SCD (b) profiles for cubic specimens (T50-H50-T1c, T50-H50-F1c,T50-H50-T2c and T50-H50-F2c) and bar-shaped ones (T50-H50-T1b and T50-H50-T2b) at 50℃ and 50% relative air humidity

4.6 Illustration and validation of MCOD evaluation

To illustrate and validate the MCOD results, the deformed mesh amplified 20 times is shown in Figure 4.30(a). The corresponding nodal displacement vectors of the upper right corner are reported in Figure 4.30(b) and the manual measurements of crack opening displacement in Figure 4.30(c) for the same region, is also shown. The deformed elements in Figure 4.30(a) follow the crack path, and there are virtually undeformed elements in adjacent positions to the crack path. There are regions in Figure 4.30(b) with different displacement directions among them; in fact, such regions are apart from each other, as illustrated by the vector field. This characteristic behavior is a consequence of cracking, which makes these regions delimited by the crack network. Further, the undeformed mesh in the selected area shows that no more than one crack is present in one element, which is pre-requested for the MCOD to be approximated by Equation (3.6).

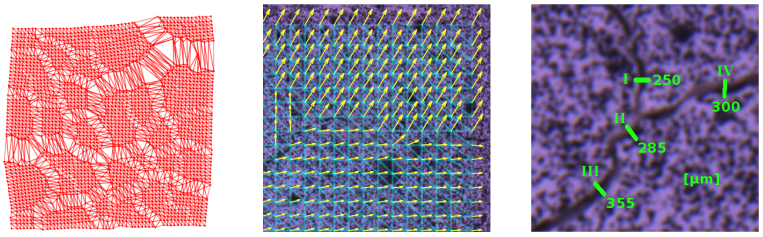

(a) (b) (c)

Figure 4.30: (a) Deformed mesh amplified 20 times for the entire surface of T50-H50-F2c sample. (b) Details of the undeformed mesh and nodal displacement vectors for the upper right corner laid over the deformed image. (c) Manual measurement of crack opening displacements in the deformed image to be compared to MCOD values reported in Figure 4.20

Some manual evaluations of crack opening displacements using the GNU Image Manipulation Program (GIMP) are reported in Figure 4.30(c) for the upper right corner of sample T50-H50-F2c (see Figure 4.20 for the corresponding MCOD field). The values are close to those found in MCODs, as shown in Table 4.4, which validates the methodology. It is worth noting that the boundaries of the crack are difficult to pinpoint very precisely, and only normal openings can be assessed in such manual measurements. The MCOD analysis easily overcomes these challenges for cases in which the assumption of one crack per element is valid. The RMS difference between the two types of estimates is less than 60 µm (*i.e.,* 1.2 pixel), which is considered very satisfactory, given the fact that the manual evaluation is based on pixel-data. Conversely, as the standard MCOD uncertainty is close to 1.3 µm (*i.e.,* 0.025 pixel), it indicates that DIC is more accurate at the scale of the displacement discretization.

Table 4.4: Crack opening displacement obtained by direct measurement (using GIMP) and MCOD data via DIC

Measurement	GIMP [µm]	DIC [µm]
I	355	252
II	285	233
III	300	326
IV	250	298

4.7 Effect of water droplet on MCOD fields

Some images were discarded from the DIC analysis because they were acquired with water droplets in the window. Water had condensed on the walls inside the climatic chamber and dropped on the glass window. The defogger keeps the window warm but not enough to dry out quickly the droplets, which act as lenses changing the optical path of the pixels behind them. This effect results in localized “optical” strains, which consequently generated false MCOD values (Figure 4.31).

Figure 4.31 shows the images prior to the water droplets, when they were present, after the evaporation, and their artifactual effect on MCOD fields. It is interesting to note that as soon as the droplets disappeared, their deleterious effect vanished as well. Gray level correction procedures [16] may be implemented to mitigate such effects.

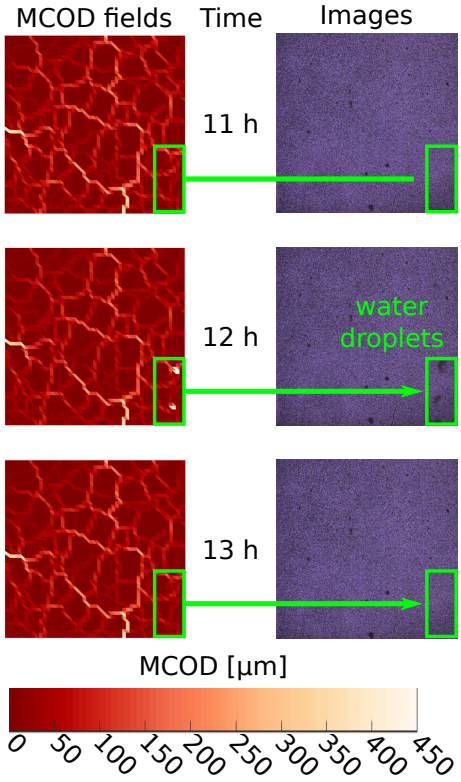

Figure 4.31: MCOD fields for T70-H50-F2c sample. The images analyzed (ROI size $\approx 60 \times 60$ mm^2) show the artifactual effect on MCOD fields caused by water droplets on the window of the climatic chamber. The color-map range of the field was limited to 450 µm because the MCOD resulted by the droplets is very high, which masks the cracks

4.8 Principal Component Analysis

The displacement fields of each frame $[\mathbf{u^{tot}}]$ (horizontal and vertical components as computed by DIC) were vectorized in columns of the $[\mathbf{U}]$ matrix, as illustrated in Equation (3.9), thereby generating an 80,000 $\times$ 200 matrix. Each row represents the displacement component of one node in one direction (*i.e.,* DOF) over time, and each column contains the displacements of all DOFs for a given frame. One image representation of the $[\mathbf{U}]$ matrix for specimen T50-H50-T1c is shown in Figure 4.32.

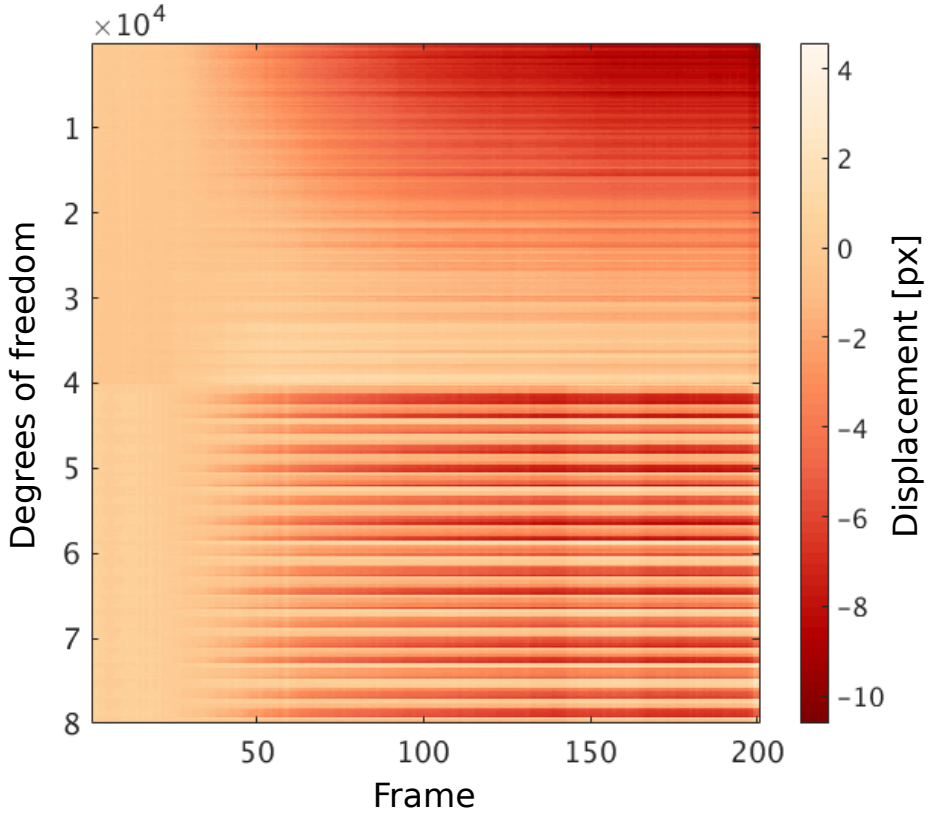

Figure 4.32: Illustration of the matrix containing the displacements used in the SVD of the PCA applied to specimen T50-H50-F2c

A similar rearrangement of the data was carried out for the maximum strain field $[\epsilon_1]$ computed using the displacements described hereafter. For this strain case, the matrix $[\mathbf{E}]$ is written with the $[\epsilon_1]$ values for each element in the rows while each column contains their development in time, thereby generating an 79,200 $\times$ 200 matrix. The $[\epsilon_1]$ is used because it is the main input of MCOD

computation.

The results of the SVD procedure are the singular values matrix $[\mathbf{S}]$, the Temporal Modes $[\mathbf{T}]$ (TMs), and the Spatial Modes $[\mathbf{V}]$ (SMs). The singular values (s_i) of $\mathbf{S}$ for the displacement field are shown in Figure 4.33 normalized by s_1 (*i.e.,* the most relevant one) and the respective first three TMs.

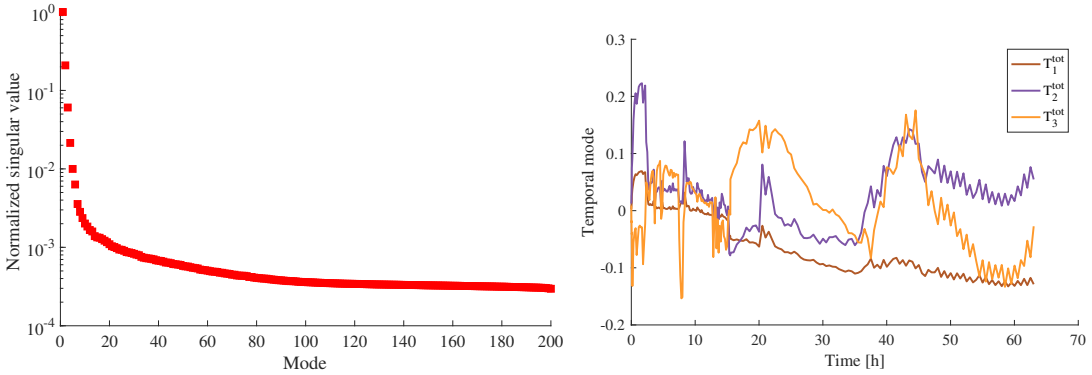

(a) (b)

Figure 4.33: Normalized singular values (a) and first three temporal modes (b) for $\mathbf{u}^{tot}$ of specimen T50-H50-F2c

Figure 4.33 shows that s_2 is more than 10 times less than s_1, which indicates that the mode 1 (*i.e.,* TM1 and SM1) may be sufficient for the reconstruction of the displacement field. TMs 1, 2 and 3 are reported in Figure 4.33(b). Because of very high fluctuations, no clear temporal signature is observed. The singular values and the first three TMs for ϵ_1 are shown in Figure 4.34. The first singular value is five times higher than the second one, thereby indicating a good separation between them. The TMs shown in Figure 4.34 (b) are rather smooth and indicate temporal signatures mainly for TM1 which seems to follow a sigmoidal tendency, except for the (arbitrary) sign.

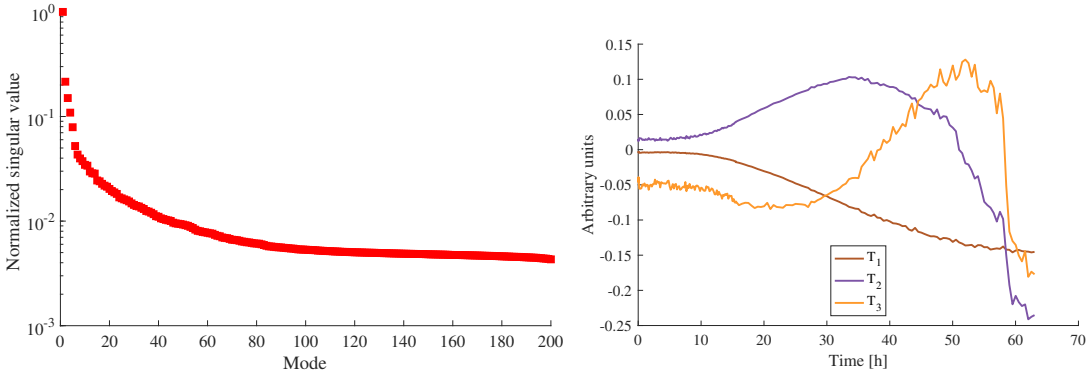

(a) (b)

Figure 4.34: Singular values and first three TMs for ϵ_1 (specimen T50-H50-F2c)

The smoothness of the first three ϵ_1 TMs indicates that the rigid body motion is a source of noise in the $\mathbf{u}^{tot}$ TMs. It is worth noting that the displacement fields provided by DIC (*i.e.,* u^{tot}) can be split into rigid body motions $\mathbf{u^{rbm}}$ and the part that causes deformation, called mechanical displacement $\mathbf{u^{mec}}$

$$\mathbf{u^{tot}}(\mathbf{x},t) = \mathbf{u^{rbm}}(\mathbf{x},t) + \mathbf{u^{mec}}(\mathbf{x},t) \tag{4.1}$$

When the strain fields are computed from the displacement ones, the rigid body motions $\mathbf{u^{rbm}}$ part is automatically discarded, remaining only $\mathbf{u^{mec}}$. The field $\mathbf{u^{mec}}$ then corresponds to the residual $\mathbf{u^{mec}}(\mathbf{x},t) = \mathbf{u^{tot}}(\mathbf{x},t) - \mathbf{u^{rbm}}(\mathbf{x},t)$. This characteristic of strain computation combined with the smoothness of ϵ_1 TMs indicate $\mathbf{u^{rbm}}$ as a source of noise. To confirm such hypothesis, The SVD procedure was applied to each part of $\mathbf{u^{tot}}$. The corresponding normalized singular values and TMs are shown in Figure 4.35 for $\mathbf{u^{rbm}}$. It is interesting to note that the first three singular values associated with $\mathbf{u^{rbm}}$ are very high (*i.e.,* more than ten orders of magnitude) in comparison with all other ones (Figure 4.35(a)). This is to be expected for such field that consists of three components and their measurement uncertainties. The temporal fluctuations of the first three TMs are similar for $\mathbf{u^{rbm}}$ (Figure 4.35(b)) and $\mathbf{u^{tot}}$ (Figure 4.33(b)).

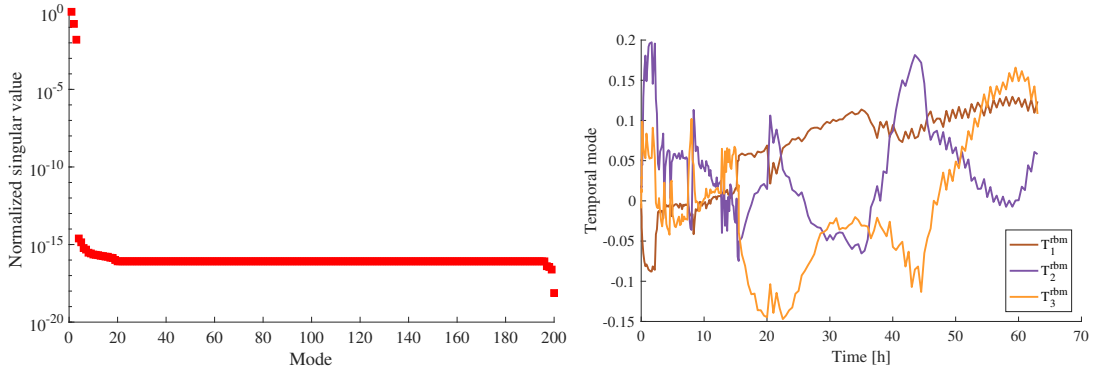

(a) (b)

Figure 4.35: Singular values (a) and first three temporal modes for $\mathbf{u}^{\mathbf{rbm}}$ (b) (specimen T50-H50-F2c)

Figure 4.36(a) shows that for $\mathbf{u}^{\mathbf{mec}}$ the first eigen value is very high in comparison to the next ones. However this difference was not as high for $\mathbf{u}^{\mathbf{tot}}$ (Figure 4.33(a)). Further, smoother changes are observed for the first two TMs (Figure 4.36(b)) in comparison to the previous ones (Figures 4.33(b) and 4.35(b)), validating the hypothesis that the $\mathbf{u}^{\mathbf{rbm}}$ is a source of noise.

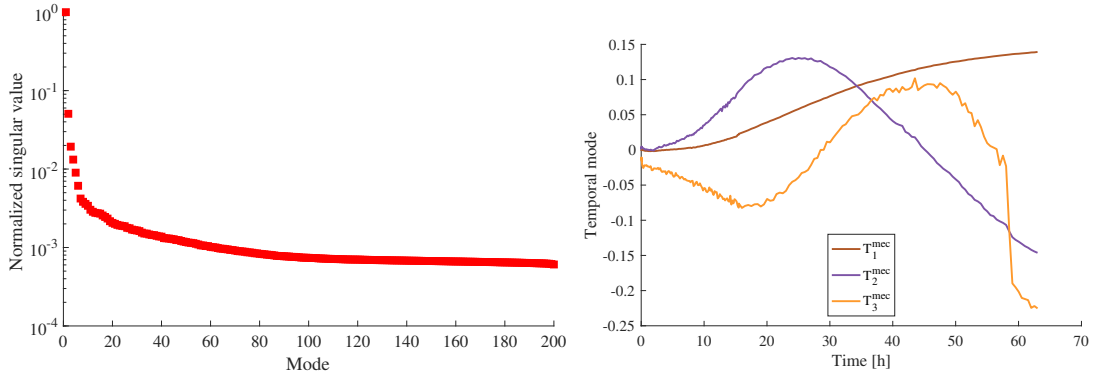

(a) (b)

Figure 4.36: Singular values (a) and first three TMs (b) for $\mathbf{u}^{\mathbf{mec}}$ (specimen T50-H50-F2c)

The first spatial modes of $\mathbf{u}^{\mathbf{tot}}$ and $\mathbf{u}^{\mathbf{mec}}$ are shown in Figure 4.37, which are interpreted as the mapping of ROI sub-regions according to the most relevant displacements. The limits of each sub-region in the SMs appear as abrupt changes in displacements, which indicate the complexity of the crack network. Further, the displacements caused by the development of cracks are dominant because they are the first SM for $\mathbf{u}^{\mathbf{tot}}$ and $\mathbf{u}^{\mathbf{mec}}$. A consequence of measurement uncertainty

is the grainy hues in the sub-regions of $\mathbf{u^{tot}}$ SM when compared to the smoother hues for $\mathbf{u^{mec}}$. This is an additional reason for focusing the study on $\mathbf{u^{mec}}$.

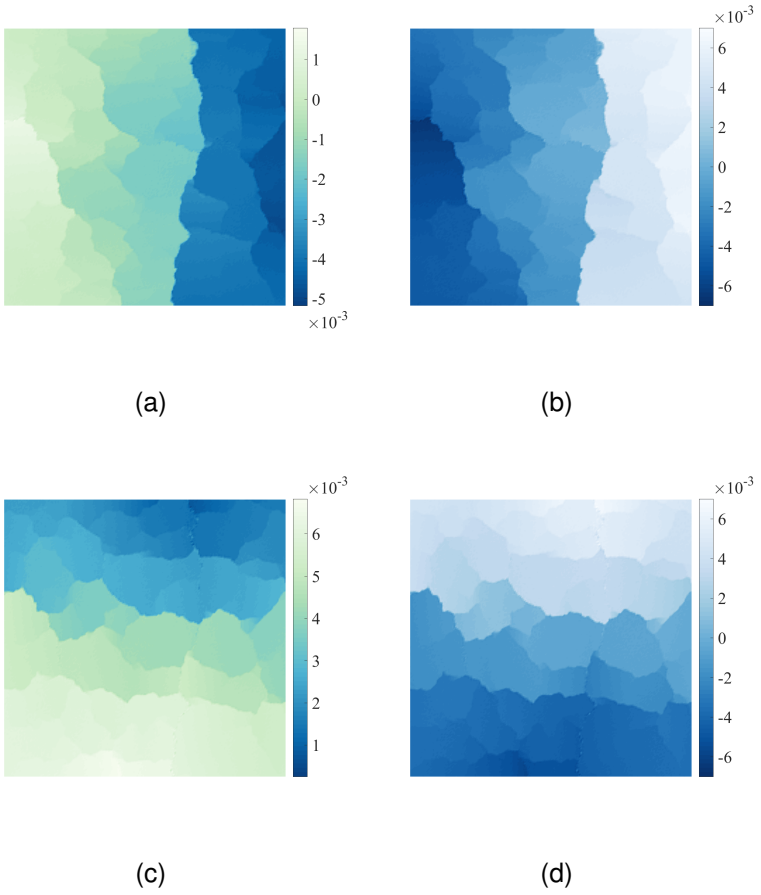

Figure 4.37: First spatial mode for $\mathbf{u^{tot}}$ (a,c) and $\mathbf{u^{mec}}$ (b,d) in the horizontal (a,b) and vertical (c,d) directions (specimen T50-H50-F2c)

The first SM is shown in Figure 4.38 for ϵ_1. The crack network is apparent as in the first SMs $\mathbf{u^{tot}}$ and $\mathbf{u^{mec}}$ of, confirming that crack openings are the main event of the displacements on the surface of the specimen. It is worth noting that the first SM has levels essentially in the contraction regime (*i.e.,* $\epsilon_1 < 0$). This trend is to be expected since the first TM was negative so that their product becomes positive, which is expected for mode I cracks.

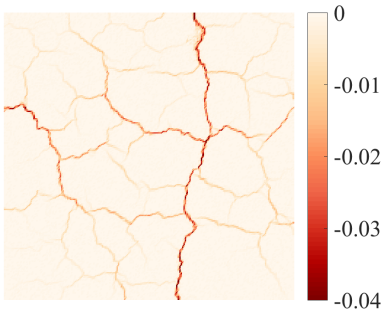

(a)

Figure 4.38: First spatial modes of the maximum principal strain field (specimen T50-H50-F2c)

4.8.1 Truncation Based on Uncertainties

One of the many features of PCA is to reconstruct the original data by using the principal components and discard the others that may correspond to noise. However, it is very important to study the error due to this truncation step and be sure that it is below the measurement uncertainty. First, the 10 initial images acquired before the crack initiation were used to evaluate the measurement uncertainties. For this analysis, each independent image pair was used, thereby resulting in a set of 90 DIC results for displacement and strain fields. The variance was computed time-wise for each degree of freedom of the displacement fields $\mathbf{u}^{\mathbf{tot}}$, $\mathbf{u}^{\mathbf{rbm}}$ and $\mathbf{u}^{\mathbf{mec}}$. Figure 4.39 shows the standard uncertainty fields for all three fields. Some areas with high uncertainties are observed in Figure 4.39(a,c,d,f) due to open pores on the castable surface. Such features create shadow regions that result in low gray level gradients, which increase the uncertainty levels. The spots with higher uncertainty in Figure 4.39(c) are due to the effect of pores, and they are less visible in Figure 4.39(a) because of the high fluctuations associated with rigid body motions, which are higher than those for mechanical displacements. The same phenomenon is observed for the vertical component (Figure 4.39(d-f)). However, the fluctuations of $\mathbf{u}^{\mathbf{rbm}}$ are higher in the vertical direction (Figure 4.39(e)) than in the horizontal one (Figure 4.39(b)), and the gradient of these fields indicates the presence of rotation, which may be caused by an accommodation of the specimen on the metal rods of the specimen

support (Figure 4.1) that may slightly move and bend (*i.e.,* fulfilling their intended role).

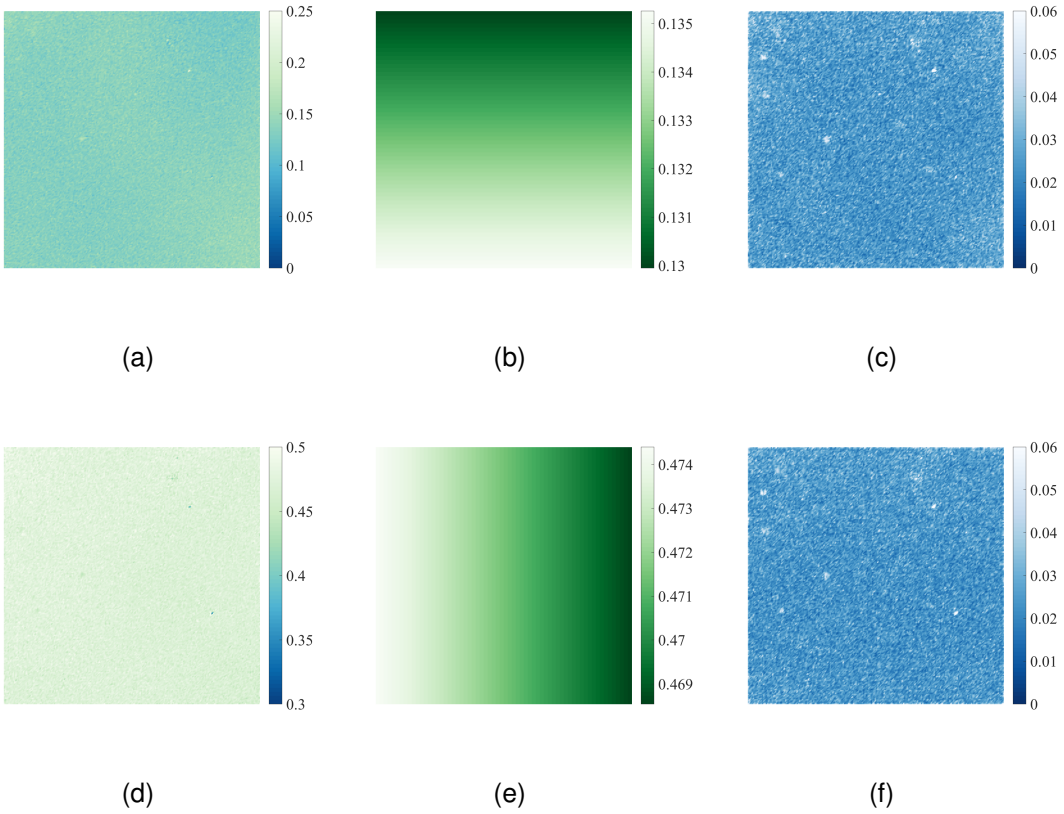

Figure 4.39: Standard displacement uncertainty fields for $\mathbf{u}^{\mathbf{tot}}$ (a,d), $\mathbf{u}^{\mathbf{rbm}}$ (b,e), and $\mathbf{u}^{\mathbf{mec}}$ (c,f) in the horizontal (a-c) and vertical (d-f) directions. The displacements are expressed in pixels

Table 4.5 shows the standard displacement uncertainties computed as the root mean of the variance fields for each direction. For $\mathbf{u}^{\mathbf{rbm}}$, the levels are one order of magnitude higher than those of $\mathbf{u}^{\mathbf{mec}}$, and close to those of $\mathbf{u}^{\mathbf{tot}}$. This result indicates that the temporal fluctuations due to $\mathbf{u}^{\mathbf{rbm}}$ cause most of those of $\mathbf{u}^{\mathbf{tot}}$. The rather low fluctuations of $\mathbf{u}^{\mathbf{mec}}$ are closer to measurement uncertainties expected from DIC measurements [93].

Table 4.5: Standard displacement uncertainties (expressed in px) for the three considered fields

	$\mathbf{u}^{\mathbf{tot}}$	$\mathbf{u}^{\mathbf{rbm}}$	$\mathbf{u}^{\mathbf{mec}}$
x	0.14	0.13	0.03
y	0.47	0.47	0.03

The same analysis was carried out for the maximum eigen strain field computed from $\mathbf{u}^{\mathbf{tot}}$ (or equivalently from $\mathbf{u}^{\mathbf{mec}}$) whose uncertainty field is shown in Figure 4.40. A rather uniform distribution is observed. The corresponding standard strain uncertainty is equal to 0.53%.

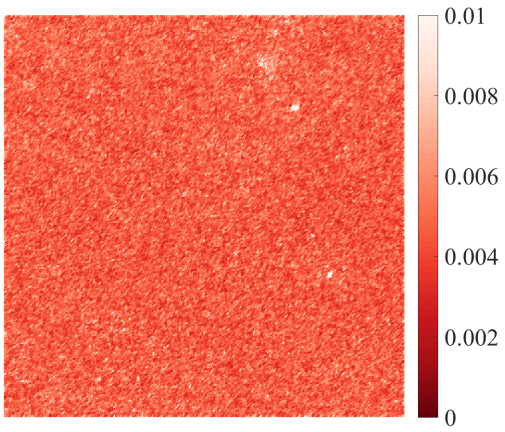

Figure 4.40: Standard uncertainty field for the maximum eigen strain ϵ_1

The Signal to Noise Ratio (SNR) is introduced as an indicator for the truncation error. First, the standard deviation of the truncation error was estimated for various numbers of modes. Then it was divided by the standard displacement uncertainty (Table 4.5). Figure 4.41 shows the change of SNR of the truncation error for the three considered displacement fields and for the maximum eigen strains. The horizontal line SNR$= 1$ shows the limit for which the truncation error reaches the measurement uncertainty. In the present case, using two terms for $\mathbf{u}^{\mathbf{tot}}$, one term for $\mathbf{u}^{\mathbf{rbm}}$ and 7 for $\mathbf{u}^{\mathbf{mec}}$ would be the optimal truncation. If only one mode was kept, the truncation error is about three times the measurement uncertainty, which is already very low.

The optimal truncation for ϵ_1 uses 14 terms as shown in Figure 4.41(b) with a smoother decay. For comparison, the truncation of $\mathbf{u}^{\mathbf{mec}}$ had only one term above twice the uncertainty level (SNR> 2) and ϵ_1 has only two terms (the second being 2.09). If only one mode is kept, the truncation error is less than three times the measurement uncertainty, which is again very low.

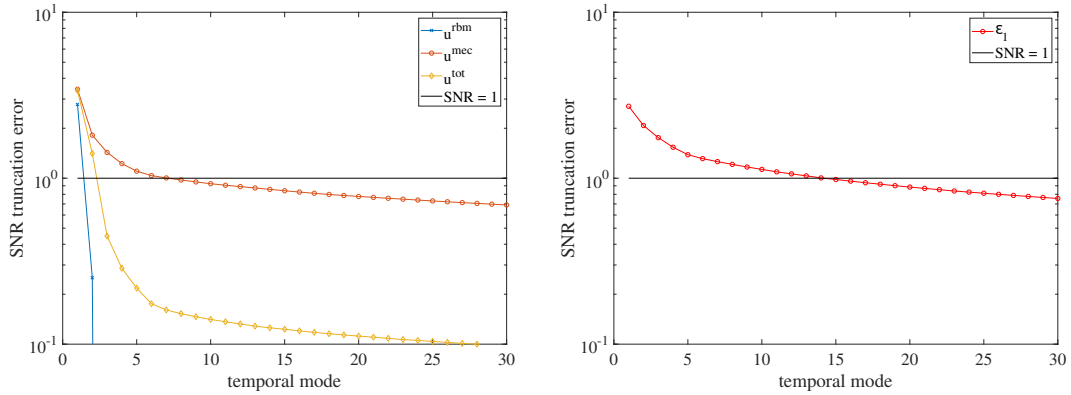

(a) (b)

Figure 4.41: Truncation errors as functions of number of modes for (a) $\mathbf{u^{tot}}$, $\mathbf{u^{rbm}}$, $\mathbf{u^{mec}}$, and (b) ε_1

From all these analysis, it is concluded that the truncation to the the first mode of $\mathbf{u^{mec}}$ and the maximum principal strain field provides most of the experimental information with a big order reduction.

The first TMs are approximated with the two-parameter Weibull law [157, 158]

$$T_1(t) = T_\infty \left(1 - \exp\left(-\left(\frac{t}{t_c}\right)^m\right)\right) \tag{4.2}$$

where m is the shape parameter (or Weibull modulus), t_c the scale parameter, and T_∞ a normalizing constant. In the present case, t_c defines the characteristic time of the transformation, and $\Delta t_c = et_c/m$ the characteristic duration (with $e = \exp(1)$), see Figure 4.42(b) in which the skeletal trend (*i.e.,* trilinear function considering that damage develops linearly from an undamaged to a fully damaged state) is defined by noting that $T_1(t = t_c)/T_\infty = 1 - 1/e$ and $(dT_1/dt(t = t_c))/T_\infty = m/et_c$. Figure 4.42(a) shows that the proposed fit is in good agreement with experimental observations.

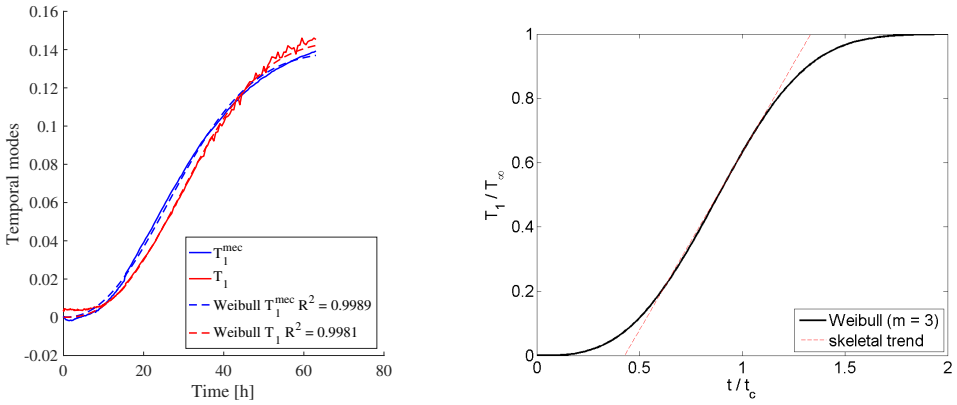

Figure 4.42: (a) First TMs associated with $\mathbf{u^{mec}}$ and $\epsilon_\mathbf{1}$ and their Weibull fit. (b) Weibull law and skeletal trend.

Table 4.6 gathers the Weibull parameters and the corresponding characteristic duration Δt_c. The latter is very close for both ways of expressing the first TM, namely, via $\mathbf{u^{mec}}$ or $\epsilon_\mathbf{1}$ even though the characteristic time and Weibull modulus are different. In the present case, the first kinematic mode is related to the development of the crack network, which is caused by the excess of MgO hydration during the curing and drying of the castable. The hydration kinetics is followed by means of damage evaluations [159]. The parameter Δt_c characterizes the duration of damage growth (due to the underlying reaction). From the skeletal trend (Figure 4.42(b)), the damage initiation time reads $t_{ini} = \frac{m+1-e}{m} t_c$ and the saturation time becomes $t_{end} = \frac{m+1}{m} t_c$ (with $\Delta t_c = t_{end} - t_{ini}$).

Table 4.6: Weibull parameters and characteristic duration for the first TM associated with $\mathbf{u^{mec}}$ and $\epsilon_\mathbf{1}$

Analyzed field	m	t_c [h]	Δt_c [h]	t_{ini} [h]	t_{end} [h]
$\mathbf{u^{mec}}$	2.3	33.7	39.8	8.5	48.4
ϵ_1	2.5	36.4	39.6	11.4	51.0

The characteristic duration Δt_c is virtually identical when using $\mathbf{u^{mec}}$ or $\epsilon_\mathbf{1}$ (Table 4.6), which is very important for the kinetic characterization of the studied process. If Δt_c had varied with the analyzed field, it would mean that there existed an interference of the PCA procedure in the kinetics, which may be an apparent acceleration (*i.e.,* reduced Δt_c) or retardation (*i.e.,* increase in Δt_c). The only effect is a shift of the initiation and saturation times depending on the analyzed field. The shift is ≈ 3 h or approximately 7% of the duration of the damage process

(*i.e.,* 40 h). In the next section, the two-parameter Weibull is applied to the other specimens to study the effect of the temperature and the relative air humidity in the kinetics of curing and drying.

4.9 Adaptive Meshing for DIC

The standard uncertainties of ϵ_1 and MCOD were computed for decreasing element sizes using images acquired before the crack initiation. The curves for the specimen T50-H50-T1c are shown in Figure 4.43, and their slopes provide the α and $\alpha + 1$.

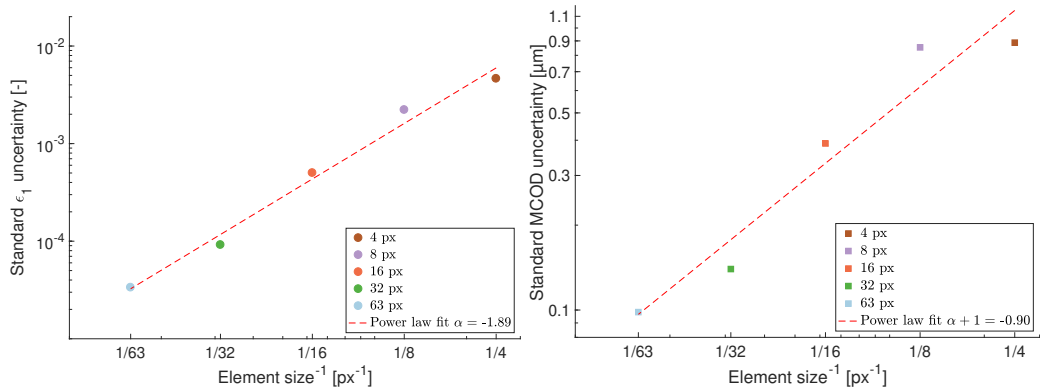

Figure 4.43: Standard uncertainties of the maximum eigen strain (a) and MCOD (b) as functions of the inverse of the element size L for the initial images of the curing and drying experiment. The dashed lines depict power law fits according to Equations (3.20) and (3.21)

The slopes of the power law fit in the semi-log plots are -1.89 and -0.90 for the ϵ_1 and for MCOD, respectively, which validates the Equations (3.20) and (3.21).

The standard deviation of the GLR normalized by the dynamic range of the reference image is shown in Figure 4.44. It was used uniform meshes (UMs) with different element sizes, *e.g.,* 64, 32, 16, 8 and 4 px, to investigate their effect on the GLR. In the beginning of the experiment, it means before the crack initiation, the overall GLR level is mainly related to acquisition noise due to lighting variations and the environment of the climatic chamber (presence of vapor streams). The correction proposed in the Brightness and Contrast Correction section (page 58) were not used herein to highlight the increase in noise sensitivity with a decrease of the element size (*i.e.,* higher spikes for small element

UMs).

Figure 4.44 shows the standard deviation of the GLR when normalized by the dynamic range of the reference picture. The effect of the element size for a uniform mesh (UM) was first investigated. At the beginning of the test, the overall GLR level is mainly related to acquisition noise. The fluctuations are also due to lighting variations and the environment of the climatic chamber. They are more pronounced in this second experiment, as highlighted by the spikes. Corrections to the gray level fluctuations were suggested for such cases [160]. However, the correction was not used herein to evidence the increase in noise sensitivity with a decrease of the element size (*i.e.,* increase in spike amplitudes for small elements).

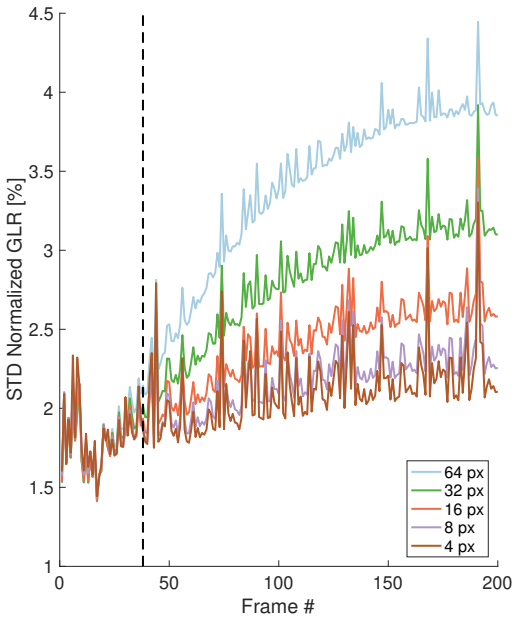

Figure 4.44: Frame by frame normalized standard deviation of the gray level residuals (GLR) as % of the dynamic range for uniform meshes with different element sizes (64, 32, 16, 8 and 4 px) for specimen T50-H50-T1c. The vertical dashed line depicts frame #38

The GLR for each UM are very close until frame #38, in which cracks start to show measurable MCOD. For the following frames, the GLR curves are distinguishable because of the lack of degrees of freedom (DOFs) to properly describe the crack network. This contribution to the GLR is less pronounced as the element size decreases and the number of DOFs increase.

The MCOD fields for frame #38 computed using the different UMs and the relation 1 px ≡ 50µm are shown in Figure 4.45. The 63 and 32-px meshes yield very coarse crack patterns, being difficult to identify a crack network. From 16 down to 4-px meshes it is easier to distinguish regions with high MCOD levels (*i.e.,* cracks) and other ones with very low values (*i.e.,* clusters of aggregates). It is worth noting that the MCOD provided by the 4-px mesh showed smaller values, which indicates an effect of mechanical regularization that can be described as an over regularization.

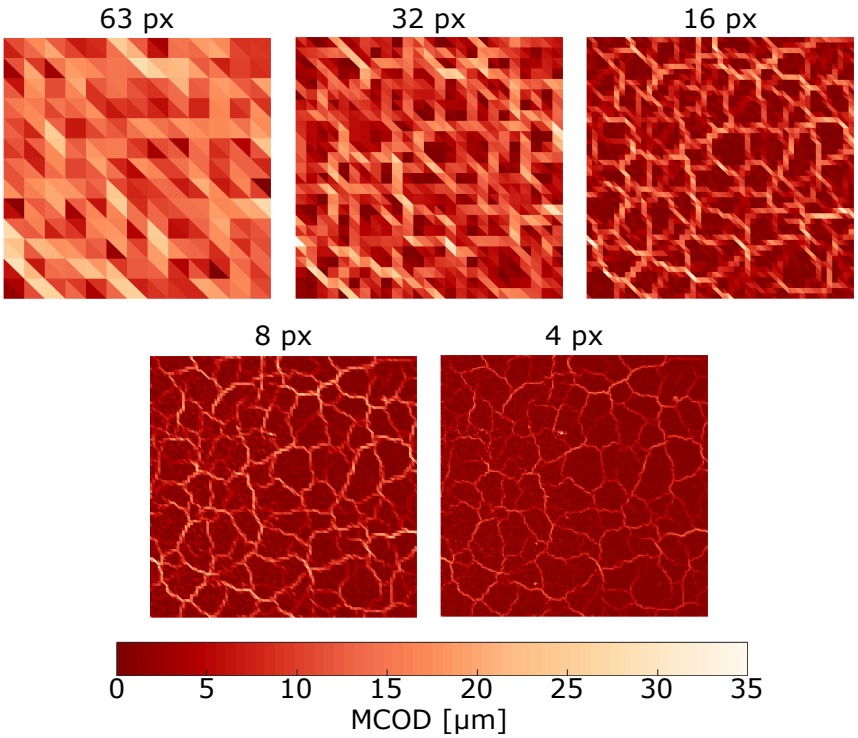

Figure 4.45: Specimen T50-H50-T1c mean crack opening displacement (MCOD) fields for frame #38 using different size UMs (1 px ≡ 50µm)

Since the AMs contain more than one element size it is convenient to classify them by the k value, *i.e.,* by the gain applied to the uncertainty threshold (Equation (3.21) page 47). Figure 4.46 shows the map of element sizes for four different values of k. For $k = 12$ and 6, the localized refinements are not very effective (the threshold gain is exaggerated), and the AMs are similar to the UMs (Figure 4.46(a-b)). However, it is possible to depict clusters of same size as the elements (*i.e.,* 16 px and 32 px) for $k = 3$ and 1.5 (Figure 4.46(c-d)). The case $k = 1.5$ leads to the best crack network description with 8 px elements for the

cracks and clusters of bigger sizes. It is worth noting that in the present case a very small level of k was needed to properly capture all the fine details associated with the crack network.

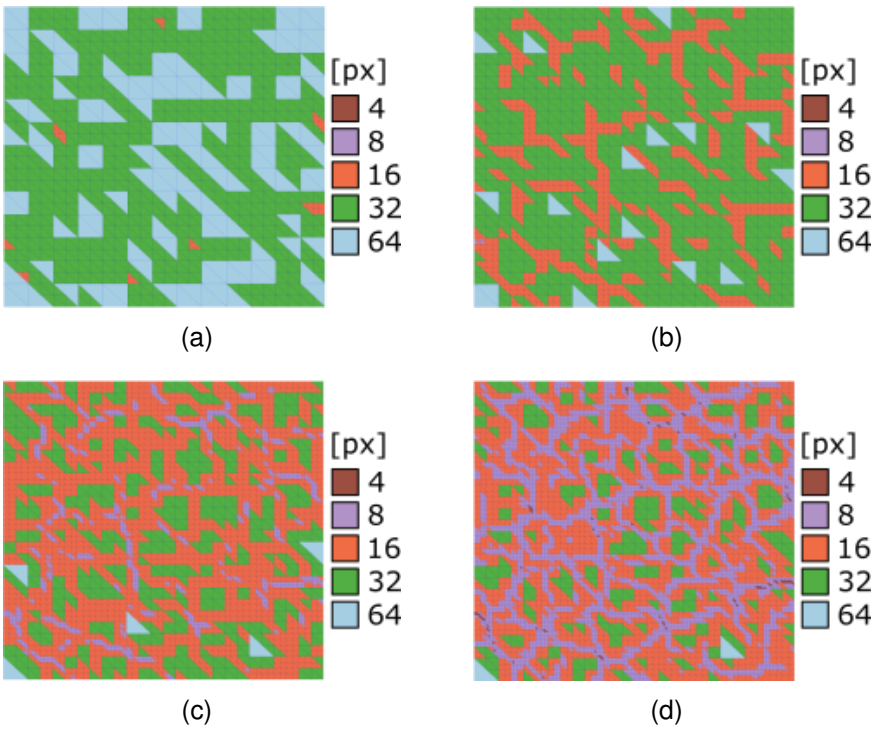

Figure 4.46: Element size maps for different initial threshold ($[\![u^*]\!] = k\sigma$, where k is the gain) for frame #38 of the MgO hydration case, defined as (a) 12, (b) 6, (c) 3, and (d) 1.5 times the displacement uncertainty (specimen T50-H50-T1c)

The resultant MCOD fields for the different AMs are shown in Figure 4.47 for frame #38. The fields for $k = 1.5$ AM (Figure 4.47(d)) and 8-px UM (Figure 4.45) are very similar. The crack network is "blurred" with an increase of k, and follows a similar trend as augmenting the element size. This similarity also indicates that $k = 1.5$ leads to the best AM for Case #3.

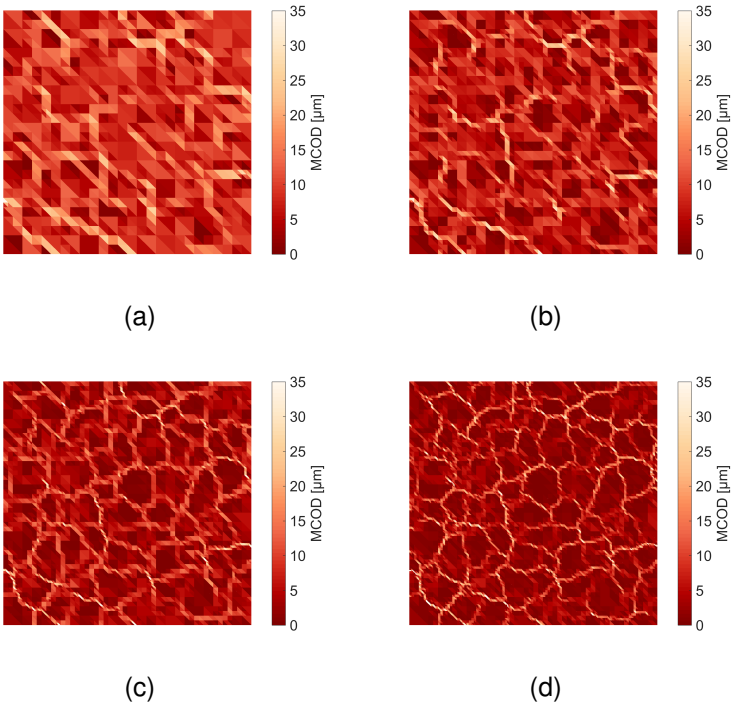

Figure 4.47: MCOD fields for picture #38 and different initial thresholds ($[\![u^*]\!] = k\sigma$) of the MgO hydration case, defined as (a) 12, (b) 6, (c) 3, and (d) 1.5 times the displacement uncertainty (specimen T50-H50-T1c)

The mean element size maps, the hanging and parent nodes, and the MCOD fields are reported in Figure 4.48 to illustrate the refinement steps. The discretizations were obtained for a sub-region of 130 $\times$ 130 px (or 6.5 $\times$ 6.5 mm^2) of specimen T50-H50-T1c for $k = 1.5$.

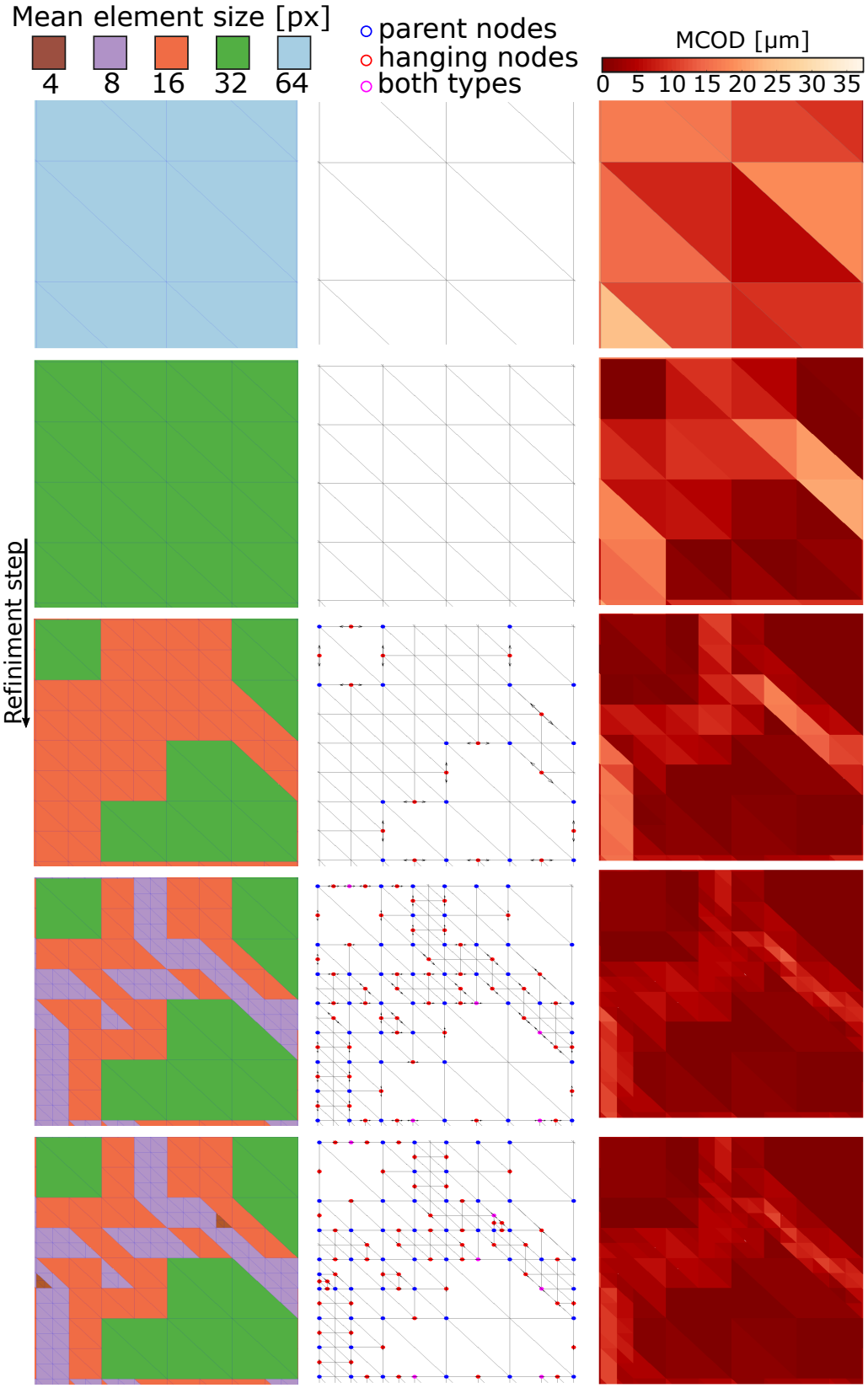

Figure 4.48: DIC + AM $k = 1.5$ for test T70-H50-T1c. (1^{st} column) Element size fields for each refinement step; (2^{nd} column) Hanging nodes and parent nodes are depicted in the meshes; (3^{rd} column) Resulting MCOD fields used to define the targets of the next refinement step (specimen T50-H50-T1c)

The AM procedure is illustrated following the rows of Figure 4.48. First, a coarse structured mesh with elements of 64 px (or 3200 µm) in length, and no hanging nodes, is used in a DIC analysis correlating the reference image and the frame #38. Elements with a MCOD higher than the AM $k = 1.5$ threshold are subdivided. The second row of Figure 4.48 shows the second step of refinement, two mean sizes of elements are present in the mesh, namely, 64 and 32 px (or 3200 and 1600 µm). In the second column, the hanging nodes (red circles) are shown between their parent nodes (blue circles). If the node is both a hanging and a parent node, it is marked in magenta. The Lagrangian matrix is written, and the resultant MCOD field after a new DIC analysis is shown in the third column. The procedure continues until the smallest elements achieve the size of 4 px (or 200 µm). The smallest elements should be longer than 1 px, otherwise, the DIC procedure may present issues during the projector step (*i.e.,* the procedure that maps the pixels in the elements).

The normalized standard deviation of GLR comparing UMs and AMs is shown in Figure 4.49 for the whole experiment. Similarly to the previously analyzed case, the smallest residuals are observed for the 4 px UM, and AM with $k = 3, 1.5$, which are close to 16 px and 8 px UMs, respectively. The similarity of the curves before frame #38 further evidences that no (or very little) cracks propagated until this point. From frame #38 onward, higher residuals are related to the new gray levels induced by the newly created cracks, and consequently the normalized GLR follows the amount of DOFs to allow the capture of this complex kinematics associated with the crack network. An additional contribution is given by the fact that mesh adaption was not performed again after frame #38.

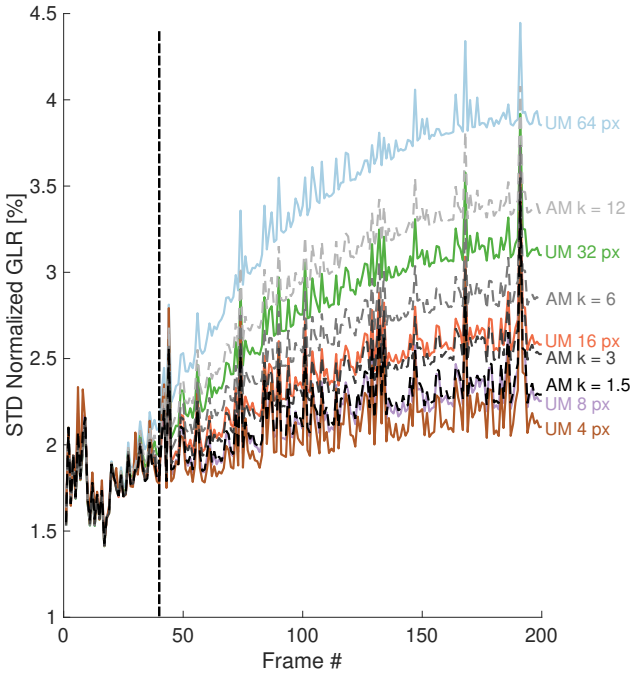

Figure 4.49: Standard deviation of GLR for the different discretizations (*i.e.,* UM: solid lines, and AM: dash dotted lines). The vertical dashed line marks frame #38 (specimen T50-H50-T1c)

The Hessian size for each case shown in Figure 4.49 is reported in Table 4.7 along with the normalized GLR for the last frame. The benefits of using AMs are inversely proportional to the crack density, *i.e.,* case where a large main crack with few branches can profit more from AM than the present case [140]. Although residuals of the 16 px UM are close to the AM with $k = 3$, the 16 px UM uses half of the number of DOFs. The main benefit comes from using the AM with $k = 1.5$, with similar GLR to the 8 px UM but using a 17% smaller Hessian, which even contains few 4 px elements and with a Hessian about 5 times smaller than the 4 px UM. In conclusion, the GLR due to the lack of DOFs to describe the crack network kinematics is reduced with smaller increases in the Hessian size because the AM procedure focuses the mesh refinement on the crack network.

Table 4.7: Sizes of the Hessian matrices for uniform (UM) and adapted (AM) meshes and standard deviation of normalized gray level residuals for the last analyzed frame (#200)

Type	Hessian size	Feature	STD of GLR [%]
UM	588	$L = 64$ px	3.85
UM	2,028	$L = 32$ px	3.10
UM	7,500	$L = 16$ px	2.58
UM	30,000	$L = 8$ px	2.26
UM	120,000	$L = 4$ px	2.11
AM	2,514	$k = 12$	3.34
AM	6,219	$k = 6$	2.83
AM	13,272	$k = 3$	2.53
AM	**24,942**	$\mathbf{k = 1.5}$	**2.29**

One point of interest arises from the frame used for mesh adaption. Figure 4.50 shows the results of an AM with $k = 1.5$ for the very last frame of the test (#200). The crack path is finely described with very small elements (Figure 4.50(a)), with considerably more 4-px elements than for the 38-th frame (Figure 4.46). The corresponding MCOD fields are compared in Figure 4.50(b-c). The fluctuations seen for frame #38 are due the fine discretization related to crack openings and not its initiation. Although the crack network was already visible in earlier frames, its openings were very small.

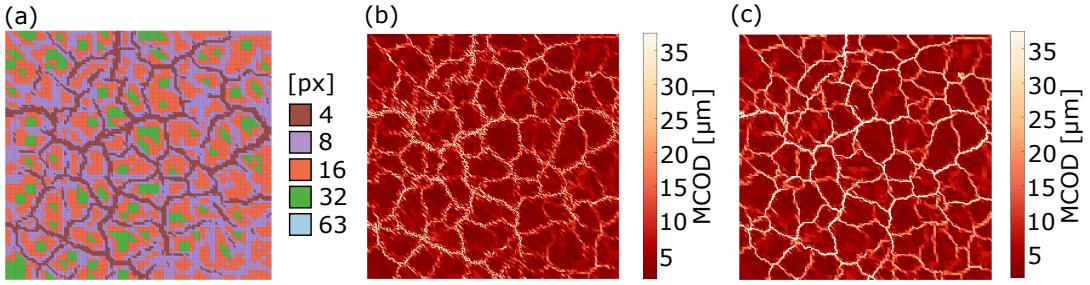

Figure 4.50: Results using a mesh adapted for the last frame. (a) Element size map. MCOD fields for the 38-th (b) and the last (c) frames (specimen T50-H50-T1c)

Last, the ratio between GLR for the AM for the 38-th frame and the last picture is shown in Figure 4.51. For earlier frames, a coarser discretization (provided by the 38-th frame) was slightly better, and as cracks subsequently opened, the second mesh provided little gain. This observation is further evidence that the crack network was already formed in early frames.

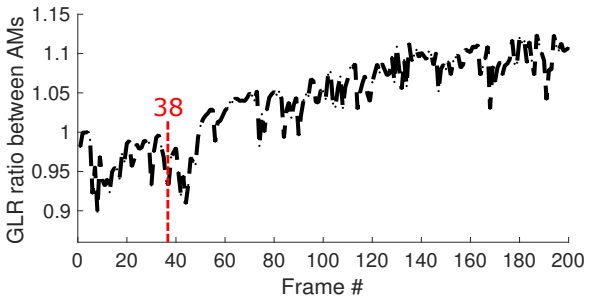

Figure 4.51: Ratio between the GLR for the AM for frame #38 and for the last one (specimen T50-H50-T1c)

5 CONCLUSIONS

Aiming to evaluate the *in situ* development of crack networks via DIC, an in-house climatic chamber with glass windows was built. The importance of using specimens with a size compatible with a Representative Volume Element was pointed out by comparing the crack networks generated by MgO hydration in high alumina castables for cubic and bar-shaped specimens, the latter being required for carrying out Impulse Excitation (IE) analyses. Cube-shaped specimens larger than the bar-shaped samples were used, and highlighted the importance of a satisfactory RVE size, as no significant boundary effects were observed for the cubes. Tomography scans showed that cracks initiated on the surface, and propagated toward the center of the castable specimens. This result validated the use of DIC as a tool to study MgO hydration using surface images. It also showed that *ex situ* scans may be carried out to fully quantify damage via digital volume correlation.

One immediate advantage of DIC over IET is that it provides *in situ* evaluations as the images are captured without taking the specimen out of the climatic chamber, thereby automating the experiment. Besides, DIC supplied more information about the damage development by highlighting its growth over time due to increased crack density, represented by Surface Crack Density (SCD) and crack openings via Mean Crack Opening Displacement (MCOD) for crack networks on the monitored surfaces.

The size of elements in DIC analyses was chosen by comparing the RMS of the gray level residuals and that of the maximum principal strain (*i.e.,* the principal data to compute the MCOD) for different sizes and different regularization lengths. A size of 6 px ($\approx$ 300 µm) was selected with a Mechanical Regularization (MR) length of 10 px. Aiming at studying damage growth generated by MgO hydration, the average MCOD and its standard deviation were computed frame by frame. The network saturation is faster at 70°C than at 50°C, which was hardly reached after 60 h for the latter. The relative air humidity did not show a conclusive effect over MgO hydration kinetics, because the increase of 20% in humidity at

50℃ reduced the brucite formation rate. However, the same increase of humidity at 50℃ sped up hydration. The crack quantification results showed fair reproducibility among similar experiments. Conversely, the SCD results were more reproducible. SCD values saturated faster than MCOD data, which accounted for crack density increase and crack opening displacements as in-depth propagation was still progressing.

Comparing the results of IE to those of DIC, the increase of damage quantified by SCD and MCOD was associated with the reduction of macroscopic Young's modulus. It was observed that macroscopic damage still increased with average MCOD, even though the SCD had saturated. This observation showed that MCOD data better captured the main features of the crack networks observed herein. Combined with the results obtained by tomography scans, all these outcomes validate the use of DIC for cases like those analyzed in this work. The MCOD fields are very useful to quantify crack networks (*e.g.,* damage localization), which is an additional advantage of DIC over IET that provides one (macroscopic) damage value for the entire specimen.

DIC analyses were assisted by MR to restrict the space of solutions and help in convergence. Further, Brightness and Contrast Corrections (BCCs) were studied, namely Brightness (B), Contrast (C), and Brightness and Contrast (BC). The BCCs made use of two discretizations, namely, one 8-noded quadrilateral (Q8) and the same mesh as that used to measure displacement fields (a Fine Mesh (FM) with 6-px triangular elements). The acquired images were divided into a first set composed of 10 images at the beginning of the experiment, and a second set covering the whole experiment. The former was used to analyze the performance of BCCs against vapor stream and temperature effects. The latter ones were used to correct the pore effect without compromising the crack quantification. The uncertainty quantifications showed that all BCCs were able to lower the gray level residuals due to experimental variations of lighting. BC corrections led to the lowest displacement and strain uncertainties for both discretizations, which were one order of magnitude less than standard DIC results. Further, to avoid interpreting pores as cracks, the Q8 discretization should be selected as it fully decouples the

very details of the kinematics from BC corrections.

The benefits of applying Principal Component Analysis (PCA) were also investigated, mainly to reduce the subjective decisions of the user in the procedure.

The first Temporal Mode (TM1) showed a sigmoidal shape, such as the one found in the literature for the MgO hydration kinetics [8]. It is very promising since the TM1 shape was obtained by Singular Value Decomposition (SVD), an algebraic procedure, without having to set a strain threshold defined by the user to classify the elements in damaged or not. By applying PCAs to the displacement fields, it was found that the rigid body motions were one source of fluctuations, which call for the procedure to be applied to $\mathbf{u^{mec}}$ or ϵ_1 fields (*i.e.,* insensitive to rigid body motions). The truncation error showed that the first modes associated with $\mathbf{u^{mec}}$ and ϵ_1 were just about three times the measurement uncertainties, which is very low given the fact that the full experimental data were reduced to one single mode. Further, the mean crack opening displacement (MCOD) fields computed for the first mode associated with $\mathbf{u^{mec}}$ and ϵ_1 were very close to each other and just slightly different, at small MCOD levels, for raw DIC results, which evidences the denoising effect of PCA.

A two-parameter Weibull law was used to approximate the first temporal modes of the analyzed fields. Virtually the same characteristic duration was found for both fields, which demonstrated no influence on the characterization of the reaction kinetics by PCA. Only a small shift in the initiation and saturation times was detected. The shift was about 7% of the characteristic duration, which lasted 40 h. With all these observations, it is concluded that PCAs applied to $\mathbf{u^{mec}}$ or ϵ_1 provided essentially identical trends for the modal characterization of the damage development in curing and drying of an MgO containing refractory castable.

It is important to highlight that the kinetics of curing and drying was studied using the first temporal mode, which was provided by PCA, thereby reducing the influence of user influence for crack definition. The present procedure is also less intrusive than the traditional bar resonance since no mechanical contact is needed nor ex-situ analyses.

Last, an Adaptive Meshing (AM) algorithm was developed to perform local-

ized h-refinement following the elements with higher displacement discontinuities (crack paths), and thus, optimize the mesh refinement for the present case. This challenging case where the specimen is placed inside a climatic chamber showed a the crack network distributed to the entire surface, which reduces the area that does not require refinement. Besides the AM procedure showed benefits for reducing the memory load with a Hessian about 17% smaller (or five times smaller for the smallest tested UM). An additional benefit was that the map for the element size after adapting the mesh already showed the overall crack network. The criterion to divide the elements was based on the standard uncertainty Mean Crack Opening Displacement (MCOD) per element. This metric was estimated by analyzing the initial frames, where no crack initiation was expected, and using uniform meshes with the same element sizes as those that will make part of the adapted meshes. The final threshold was proportional to the MCOD uncertainty to only account for cracks (*i.e.,* a multiplicative factor $k > 1$ was considered).

6 SUGGESTIONS FOR FUTURE WORK

The following suggestions are proposed for future work.

The DIC methodology developed herein can be applied to study the relationship between the packing factor (q) and the crack network. Further, Calcium Aluminate Cement (CAC) content is relevant to damage initiation during MgO hydration, which may affect cracking. Another suggestion is to vary the shape of the specimen. For example, use a WST specimen to study the effect of macroscopic cracks (initiated by stress concentrations in pre-crack initiated on the notch) on the crack network formation.

Digital Volume Correlation may be applied to evaluate the damage in the entire volume of the specimen, not only on the surface. Further, the contrast in tomographic images represents the density of constituents, which may provide insights about the effects of the microstructure on the crack network. The AM procedure has a high potential of reducing the computational cost of Digital Volume Correlation analysis, where data are usually considerably bigger than DIC, especially for cases with localized phenomena as the Wedge Splitting Test. Implementing a refinement termination based on the gray level residuals and real-time applications of this procedure during the DIC analyses of many images are other future improvements of this new methodology.

The kinetics of curing and drying was studied using the first temporal mode can be improved by testing other mathematical models than the two-parameter Weibull described hereafter. The Proper Generalized Decomposition (PGD) may be used to successive enrich the kinematic model used to represent the MgO hydration.

7 REFERENCES

[1] Lee WE, Vieira W, Zhang S, Ahari KG, Sarpoolaky H, Parr C. Castable refractory concretes. International Materials Reviews 2001;46(3):145–67.

[2] Landy RA. Magnesia refractories. Mechanical Engineering-New York and Basel-Marcel Dekker Then Crc Press/Taylor and Francis 2004;178:109.

[3] Salomão R, Bittencourt LRM, Pandolfelli VC. A novel approach for magnesia hydration assessment in refractory castables. Ceramics International 2007;33(5):803–10.

[4] Tripathi HS, Mukherjee B, Das S, Haldar MK, Das SK, Ghosh A. Synthesis and densification of magnesium aluminate spinel: effect of MgO reactivity. Ceramics International 2003;29(8):915–8.

[5] Braulio MAL, Bittencourt LRM, Pandolfelli VC. Magnesia grain size effect on in situ spinel refractory castables. Journal of the European Ceramic Society 2008;28(15):2845–52.

[6] Braulio MA, Castro JF, Pagliosa C, Bittencourt Luis R M, Pandolfelli VC. From macro to nanomagnesia: designing the in situ spinel expansion. Journal of the American Ceramic Society 2008;91(9):3090–3.

[7] Souza TM, Braulio MAL, Luz AP, Bonadia P, Pandolfelli VC. Systemic analysis of MgO hydration effects on alumina–magnesia refractory castables. Ceramics International 2012;38(5):3969–76.

[8] Salomão R, Bittencourt LRM, Pandolfelli VC. A novel magnesia based binder (MBB) for refractory castables. Interceramic 2009;58:21–4.

[9] Souza TM, Luz AP, Braulio MA, Pagliosa C, Pandolfelli VC. Acetic acid role on magnesia hydration for cement-free refractory castables. Journal of the American Ceramic Society 2014;97(4):1233–41.

[10] Santos T, Luz AP, Pagliosa C, Pandolfelli VC. $Mg(OH)_2$ nucleation and growth parameters applicable for the development of MgO-based refractory castables. Journal of the American Ceramic Society 2016;.

[11] ASTM C 1198. Standard test method for dynamic young's modulus, shear modulus, and poisson's ratio for advanced ceramics by sonic resonance. Tech. Rep.; ASTM International; West Conshohocken; 2013.

[12] Braulio MAL, Milanez DH, Sako EY, Bittencourt LRM, Pandolfelli VC. Expansion behavior of cement bonded alumina–magnesia refractory castables. Am Ceram Soc Bull 2007;86(12):9201–6.

[13] ASTM E 1876. Standard test method for dynamic Young's modulus, shear modulus, and Poisson's ratio by impulse excitation of vibration. Tech. Rep.; ASTM International; West Conshohocken; 2015.

[14] Telle R, Traon N, Tonnesen T. The understanding of the microstructural changes of refractory castables after thermal shocks through damping measurements. Refractories Worldforum 2012;4(1):119–24.

[15] Salomão R, Souza ADV, Cardoso PHL. A comparison of $Al(OH)_3$ and $Mg(OH)_2$ as inorganic porogenic agents for alumina. Interceram-International Ceramic Review 2015;64(4-5):193–9.

[16] Hild F, Roux S. Digital Image Correlation. Weinheim (Germany): Wiley-VCH; 2012, p. 183–228.

[17] Saracura RGM, Canto RB, Pandolfelli VC, Schmitt N, Hild F. Surface crack network detection on MgO-based refractory castable by digital image correlation. China's Refractories 2015;24(1):32–7.

[18] Leclerc H, Neggers J, Mathieu F, Roux S, Hild F. Correli 3.0. 2015. IDDN.FR.001.520008.000.S.P.2015.000.31500.

[19] Neggers J, Mathieu F, Hild F, Roux S, Swiergiel N. Improving full-field identification using progressive model enrichments. International Journal of Solids and Structures 2017;:–URL: http://www.sciencedirect.com/science/article/pii/S0020768317301191. doi:https://doi.org/10.1016/j.ijsolstr.2017.03.013.

[20] Riul C, Tita V, de Carvalho J, Canto RB. Processing and mechanical properties evaluation of glass fiber-reinforced ptfe laminates. Composites Science and Technology 2012;72(11):1451–8. URL: http://www.sciencedirect.com/science/article/pii/S0266353812002084?v=s5. doi:10.1016/j.compscitech.2012.05.021.

[21] Saracura RGM, Santos FS, Razzino CA, Libardi W, Tarpani JR, Canto RB. Análise dos campos de deslocamento e de deformação pela técnica de correlação de imagens digitais em laminados compósitos sólidos ensaia-

dos por compressão após impacto. In: Congresso Brasileiro de Engenharia e Ciência dos Materiais. 2012, p. 5494–501.

[22] Tarpani JR, Canto RB, Saracura RGM, Ibarra-Castanedo C, Maldague XPV. Compression after impact and fatigue of reconsolidated fiber-reinforced thermoplastic matrix solid composite laminate. Procedia Materials Science 2014;3(0):485 –92. URL: http://www.sciencedirect.com/science/article/pii/S2211812814000820. doi:http://dx.doi.org/10.1016/j.mspro.2014.06.081; 20th European Conference on Fracture.

[23] Sciuti VF, Angélico RA, Bose-Filho WW, Schmitt N, Canto RB. Identificação dos parâmetros de um modelo de comportamento mecânico para o PTFE sob -10$^{\circ}C$ assistida pela técnica de correlação de imagens digitais e por métodos de otimização. In: Congresso Brasileiro de Engenharia e Ciência dos Materiais - 21° CBECiMat. Cuiabá; 2014, p. 7109–16.

[24] Gamboni OC, Riul C, Billardon R, Bose Filho WW, Schmitt N, Canto RB. On the formation of defects induced by air trapping during cold pressing of PTFE powder. Polymer 2016;82:75–86. doi:10.1016/j.polymer.2015.11.014.

[25] Strabelli PG, Sciuti VF, Montilha FS, Canto LB, Canto RB. Influência de variáveis de sinterização na microestrutura de peças de PTFE moldadas por prensagem isostática. Polímeros: Ciência e Tecnologia 2014;24(5):612–9. doi:http://dx.doi.org/10.1590/0104-1428.1660.

[26] Montilha FS, Sciuti VF, Riul C, Bose-Filho WW, Schmitt N, Canto RB. Análise da aplicação do método da normalização linear da carga para identificação de curvas J-R e da tenacidade à fratura do politetrafluoretileno (PTFE). In: Congresso Brasileiro de Engenharia e Ciência dos Materiais - 21° CBECiMat. Cuiabá; 2014, p. 7141–8.

[27] Melo CC. Desenvolvimento de um ensaio mecânico não convencional para a análise da relaxação de tensões do politetrafluoretileno. Master's thesis; Universidade Federal de São Carlos; 2016.

[28] Sciuti VF, Melo CC, Montilha FS, Rocco FO, Canto RB. Numerical simulation procedure for design optimization of the mold used in rubber isostatic pressing of metal powders. In: Tenth International Latin American Conference on Powder Technology (PTECH). 2015,.

[29] Tita V, Caliri MF, Angélico RA, Canto RB. Experimental analyses of the poly(vinyl chloride) foams' mechanical anisotropic behavior. Polymer Engineering & Science 2012;52(12):2654–63. URL: http://dx.doi.org/10.1002/pen.23222. doi:10.1002/pen.23222.

[30] Montilha FS, Rocco FO, Melo CC, Sciuti VF, Canto RB. Identification of dilatancy in green compacted ceramic powder via digital image correlation. Powder Technology 2018;330:471–6.

[31] Rocco FO, Melo CC, Balancin O, Canto RB. Identificação de parâmetros para a simulação computacional da prensagem de pós ferrosos. In: Congresso Brasileiro de Engenharia e Ciência dos Materiais - 21° CBECiMat. Cuiabá; 2014, p. 5400–7.

[32] Vargas R, Neggers J, Canto RB, Rodrigues JA, Hild F. Analysis of wedge splitting test on refractory castable via integrated DIC. Journal of the European Ceramic Society 2016;36(16):4309–17.

[33] Vargas R, Neggers J, Canto RB, Rodrigues JA, Hild F. Comparison of two full-field identification methods for the wedge splitting test on a refractory. Journal of the European Ceramic Society 2018;38(16):5569 –79.

[34] Vargas R, Neggers J, Canto RB, Rodrigues JA, Hild F. Analysis of a castable refractory using the wedge splitting test and cohesive zone model. Journal of the European Ceramic Society 2019;39(13):3903–14.

[35] Robert L, Nazaret F, Cutard T, Orteu JJ. Use of 3D digital image correlation to characterize the mechanical behavior of a fiber reinforced refractory castable. Experimental Mechanics 2007;47(6):761–73.

[36] Belrhiti Y, Pop O, Germaneau A, Doumalin P, Dupré JC, Harmuth H, et al. Investigation of the impact of micro-cracks on fracture behavior of magnesia products using wedge splitting test and digital image correlation. Journal of the European Ceramic Society 2015;35(2):823–9.

[37] Sutton MA, Zhao W, McNeill SR, Helm JD, Piascik RS, Riddell WT. Advances in fatigue crack closure measurement and analysis: Second Volume; chap. Local crack closure measurements: Development of a measurement system using computer vision and a far-field microscope. West Conshohocken: ASTM STP 1343; 1999, p. 145–56.

[38] Benboudjema F, Mauroux T, Turcry P, Ait-Mokthar A, Deves O. Experimental analysis of drying shrinkage cracking in coating mortars by digital image correlation. In: Mechanics and Physics of Creep, Shrinkage, and Durability of Concrete: A Tribute to Zdeněk P. Bažant: Proceedings of the Nineth International Conference on Creep, Shrinkage, and Durability Mechanics (CONCREEP-9), September 22-25, 2013 Cambridge, Massachusetts. ASCE Publications; 2013, p. 235.

[39] Hild F, Bouterf A, Roux S. Damage measurements via DIC. International Journal of Fracture 2015;191(1-2):77–105.

[40] Garbers-Craig A. Presidential address: How cool are refractory materials? Journal of the Southern African Institute of Mining and Metallurgy 2008;108(9):491–506.

[41] Nishikawa A. Technology of Monolithic Refractories, Tech. Rept. No 33-7 1984;.

[42] Lee WE, Moore RE. Evolution of in situ refractories in the 20th century. Journal of the American Ceramic Society 1998;81(6):1385–410.

[43] Banerjee S. Properties of refractories. Mechanical Engineering-New York And Basel-Marcel Dekker Then Crc Press/Taylor And Francis 2004;178:1.

[44] Wachtman J. Materials and Equipment - Whitewares - Refractory Ceramics - Basic Science: Ceramic Engineering and Science Proceedings, Volume 16. No. 1 in Ceramic Engineering and Science Proceedings; Wiley; 2009. ISBN 9780470316306.

[45] Luz AP, Braulio MAL, Pandolfelli VC. Refractory Castable Engineering; vol. 1. 1 ed.; São Carlos, SP: Göller Verlag; 2015.

[46] Ko YC, Lay JT. Thermal expansion characteristics of alumina–magnesia and alumina–spinel castables in the temperature range 800–1650°C. Journal of the American Ceramic Society 2000;83(11):2872–4.

[47] Schnabel M, Buhr A, Exenberger R, Rampitsch C. Spinel: In-Situ Versus Preformed- Clearing The Myth. Refractory Worldforum 2010;2(2):87–93.

[48] Sugawara M, Asano K. The recent developments of castable technology in japan? 2005;:30–4.

[49] McGeary RK. Mechanical packing of spherical particles. Journal of the

American ceramic Society 1961;44(10):513–22.

[50] Oliveira IR, Ortega FS, Pandolfelli VC. Hydration of CAC cement in a castable refractory matrix containing processing additives. Ceramics International 2009;35(4):1545–52.

[51] Innocentini M, Pileggi R, Ramal Jr F, Pandolfelli V. Psd-designed refractory castables. American Ceramic Society Bulletin 2003;82(7):1–6.

[52] Salomao R, Pandolfelli VC. The particle size distribution effect on the drying efficiency of polymeric fibers containing castables. Ceramics International 2008;34(1):173–80.

[53] DINGER DR. Particle Packing, Part III: discrete versus continuous particles sizes. 1992.

[54] Dinger D, Funk J. Particle packing. II: Review of packing of polydisperse particle systems. Interceram 1992;41(2):95–7.

[55] Furnas CC. Department of commerce, bureau of mines, report of investigation serial no. 2894, 1928. Bulletin of US Bureau of Mines 1929;307:74.

[56] Oliveira I, Studart A, Pileggi R, Pandolfelli V. Dispersion and packing of particles—basic principles and applications to ceramic processing. Fazendo Arte Editorial 2000;.

[57] Studart AR, Pandolfelli VC, Tervoort E, Gauckler LJ. Selection of dispersants for high-alumina zero-cement refractory castables. Journal of the European Ceramic Society 2003;23(7):997–1004.

[58] Studart AR, Zhong W, Pandolfelli VC. Rheological design of zero-cement self-flow castables. American Ceramic Society Bulletin 1999;78(5):65–72.

[59] Ortega FS, Pileggi RG, Sepulveda P, Pandolfelli VC. OPTIMISING PARTICLE PACKING IN POWDER CONSOLIDATION. American ceramic society bulletin 1999;78(8):106–11.

[60] Ismael MR, Salomao R, Pandolfelli VC. Colloidal silica bonded refractory castables: optimization of the particle size distribution. Refractories Applications and News 2008;13(1):10–5.

[61] Scrivener KL, Nemati KM. The percolation of pore space in the cement paste/aggregate interfacial zone of concrete. Cement and Concrete Research 1996;26(1):35–40.

[62] Roy DM, Scheetz BE, Silsbee MR. Processing of optimized cements and concretes via particle packing. MRS bulletin 1993;18(3):45–9.

[63] Myhre B. The Effect of Particle Size Distribution on Flow of Refractory Castables. Elkem Refractories. International Ceramics, Norway 1994;.

[64] Myhre B, Hundere AM. The use of particle size distribution in development of refractory castables. In: XXV ALAFAR Congress, San Carlos de Bariloche, Argentina. 1996,.

[65] Pileggi RG, Ramal FT, Paiva AE, Pandolfelli VC. High performance refractory castables: particle size design. Refract Appl News 2003;8(5):17–21.

[66] Pileggi RG, Studart AR, Innocentini M, Pandolfelli VC. High-performance refractory castables. American Ceramic Society Bulletin 2002;81(6):37–42.

[67] Nouri-Khezrabad M, Braulio MAL, Pandolfelli VC, Golestani-Fard F, Rezaie HR. Nano-bonded refractory castables. Ceramics International 2013;39(4):3479–97.

[68] Oliveira IR, Pandolfelli VC. Castable matrix, additives and their role on hydraulic binder hydration. Ceramics international 2009;35(4):1453–60.

[69] Innocentini MDM, Cardoso F, Paiva AEM, Pandolfelli VC. Dewatering refractory castables. American Ceramic Society Bulletin 2004;83(7):9101–8.

[70] Cardoso FA, Innocentini MDM, Miranda MFS, Valenzuela FAO, Pandolfelli VC. Drying behavior of hydratable alumina-bonded refractory castables. Journal of the European Ceramic Society 2004;24(5):797–802.

[71] Nonnet E, Lequeux N, Boch P, Colston SL, Barnes P. In Situ X-ray Diffraction and Young's Modulus Measurement during Heat Treatment of High-Alumina Cement Castables. Journal of the American Ceramic Society 2001;84(3):583–7.

[72] Simonin F, Wohrmeyer C, Parr C, Kerneos S. New method for assessing calcium aluminate cements. In: Unitecr'05. Proc. Unified Int. Tech. Conf. on Refractories. 9 th Biennial Worldwide Congress on Refractories; vol. 8. 2006, p. 849–53.

[73] Chotard T, Gimet-Breart N, Smith A, Fargeot D, Bonnet JP, Gault C. Characterisation of calcium aluminate cement hydration at young age by ultrasonic testing. In: International conference on calcium aluminate cements.

2001, p. 155–67.

[74] Innocentini MDM, Cardoso FA, Akyioshi MM, Pandolfelli VC. Drying Stages during the Heating of High-Alumina, Ultra-Low-Cement Refractory Castables. Journal of the american ceramic society 2003;86(7):1146–8.

[75] Salomão R, Pandolfelli VC. Microsilica addition as anti-hydration technique of magnesia in refractory castables. Cerâmica 2008;54(329):43–8.

[76] Hall CW, Others . Dictionary of drying. Marcel Dekker, Inc.; 1979.

[77] Innocentini M, Salomão R, Ribeiro C, Cardoso F, Pandolfelli V, Rettore R, et al. Permeability of fiber-containing refractory castables-part 1. American Ceramic Society Bulletin 2002;81(7):34.

[78] Innocentini M, Salomão R, Ribeiro C, Cardoso F, Pandolfelli V, Rettore R, et al. Permeability of fiber-containing refractory castables-part 2. American Ceramic Society Bulletin 2002;81(8):65.

[79] Myhre B, Ødegård C, Feldborg H. Periclase castables based on the bond MgO–SiO2–H2O: Properties and current status. In: Presented at the INREFCON (5th India International Refractories Congress) in Bhubaneswar, India. 2002,.

[80] Salomao R, Pandolfelli VC, Salomão R, Pandolfelli VC. The role of hydraulic binders on magnesia containing refractory castables: calcium aluminate cement and hydratable alumina. Ceramics International 2009;35(8):3117–24.

[81] Sutcu M, Akkurt S, Okur S. Influence of crystallographic orientation on hydration of MgO single crystals. Ceramics International 2009;35(7):2571–6.

[82] Birchal VS, Rocha SDF, Mansur MB, Ciminelli VST. A simplified mechanistic analysis of the hydration of magnesia. The Canadian Journal of Chemical Engineering 2001;79(4):507–11.

[83] Landy RA. Magnesia refractories. Mechanical Engineering-New York And Basel-Marcel Dekker Then Crc Press/Taylor And Francis 2004;178:109.

[84] Jansen H. Refractories for the production of steel. CN-Refractories, Germany 1999;6:15–9.

[85] Chatterji S. Mechanism of expansion of concrete due to the pres-

ence of dead-burnt CaO and MgO. Cement and Concrete Research 1995;25(1):51–6.

[86] Lobo Carneiro FC. Um novo método para determinacão da resistência à tração dos concretos. Proc Anais 5a reunião da Associação Brasileira de Normas Técnicas (ABNT) em São Paulo 1943;:127–9.

[87] Besnard G, Hild F, Roux S. “Finite-Element” displacement fields analysis from digital images: Application to Portevin-Le Chatelier bands. Experimental Mechanics 2006;46(6):789–803.

[88] McNeill S, Peters W, Sutton M. Estimation of stress intensity factor by digital image correlation. Engineering Fracture Mechanics 1987;28(1):101–12.

[89] Abanto-Bueno J, Lambros J. Investigation of crack growth in functionally graded materials using digital image correlation. Engineering Fracture Mechanics 2002;69:1695–711.

[90] Forquin P, Rota L, Charles Y, Hild F. A method to determine the toughness scatter of brittle materials. International Journal of Fracture 2004;125(1):171–87.

[91] Mathieu F, Hild F, Roux S. Identification of a crack propagation law by digital image correlation . International Journal of Fatigue 2012;36(1):146–54.

[92] Sutton MA. Computer Vision-Based, Noncontacting Deformation Measurements in Mechanics: A Generational Transformation. Applied Mechanics Reviews 2013;65(AMR-13-1009, 050802).

[93] Hild F, Roux S. Digital image correlation. In: Rastogi P, Hack E, editors. Optical Methods for Solid Mechanics. A Full-Field Approach. Weinheim (Germany): Wiley-VCH; 2012, p. 183–228.

[94] Hild F, Roux S. Comparison of local and global approaches to digital image correlation. Experimental Mechanics 2012;52(9):1503–19.

[95] Vargas R, Tsitova A, Bernachi-Barbe F, Bary B, Canto RB, Hild F. On the identification of cohesive zone model for curved crack in mortar. submitted for publication 2020;.

[96] Burt PJ. Local correlation measures for motion analysis: a comparative study. In: Proc. Pattern Recognition and Image Processing Conf., Las

Vegas, 1982. 1982,.

[97] Sutton MA, Wolters WJ, Peters WH, Ranson WF, McNeill SR. Determination of displacements using an improved digital correlation method. Image and Vision Computing 1983;1(3):133 –9.

[98] Sutton MA, McNeill SR, Helm JD, Chao YJ. Advances in two-dimensional and three-dimensional computer vision; vol. 77 of *Topics in Applied Physics*. 2000.

[99] Sutton MA, Orteu JJ, Schreier H. Image correlation for shape, motion and deformation measurements: Basic concepts, theory and applications. Springer Science & Business Media; 2009.

[100] Lewis JP. Fast template matching. In: Vision interface; vol. 95. 1995, p. 15 –9.

[101] Roux S, Hild F, Berthaud Y. Correlation image velocimetry: A spectral approach. Applied Optics 2002;41(1):108–15.

[102] Wagne B, Roux S, Hild F. Spectral approach to displacement evaluation from image analysis. European Physical Journal Applied Physics 2002;17:247–52.

[103] Broggiato GB. Adaptive image correlation technique for full-field strain measurement. In: Pappalettere C, editor. Proceedings of ICEM12-12th International Conference on Experimental Mechanics. McGraw Hill, Lilan (Italy); 2004, p. 420–1.

[104] Sun Y, Pang J, Wong C, Su F. Finite-element formulation for a digital image correlation method. Applied Optics 2005;44(34):7357–63.

[105] Leclerc H, Périé J, Roux S, Hild F. Integrated digital image correlation for the identification of mechanical properties; vol. LNCS 5496. Berlin (Germany): Springer; 2009, p. 161–71.

[106] Roux S, Hild F, Leclerc H. Mechanical assistance to DIC. In: Espinosa H, Hild F, editors. Full field measurements and identification in Solid Mechanics; vol. Procedia I. Elsevier; 2012, p. 159–68.

[107] Réthoré J, Hild F, Roux S. Extended digital image correlation with crack shape optimization. International Journal for Numerical Methods in Engineering 2008;73(2):248–72.

[108] Roux S, Hild F. Stress intensity factor measurements from digital image correlation: post-processing and integrated approaches. International Journal of Fracture 2006;140(1-4):141–57.

[109] Leclerc H, Périé JN, Roux S, Hild F. Integrated digital image correlation for the identification of mechanical properties. In: International Conference on Computer Vision/Computer Graphics Collaboration Techniques and Applications. Springer; 2009, p. 161–71.

[110] Mathieu F, Leclerc H, Hild F, Roux S. Estimation of elastoplastic parameters via weighted FEMU and integrated-DIC. Experimental Mechanics 2015;55(1):105–19.

[111] Réthoré J, Roux S, Hild F. An extended and integrated digital image correlation technique applied to the analysis of fractured samples: The equilibrium gap method as a mechanical filter. European Journal of Computational Mechanics 2009;18(3-4):285–306.

[112] Tomičevć Z, Hild F, Roux S. Mechanics-aided digital image correlation. The Journal of Strain Analysis for Engineering Design 2013;48(5):330–43.

[113] Saracura RGM, Canto RB, Pandolfelli VC, Schmitt N, Hild F. Digital image correlation as a tool for monitoring crack networks on the surface of MgO-based refractory castables. Advances in Science and Technology 2014;92:242–7. doi:10.4028/www.scientific.net/AST.92.242.

[114] Claire D, Hild F, Roux S. A finite element formulation to identify damage fields: The equilibrium gap method. Int J Num Meth Engng 2004;61(2):189–208.

[115] Leclerc H, Périé J, Roux S, Hild F. Voxel-scale digital volume correlation. Exp Mech 2011;51(4):479–90.

[116] Sutton MA, Li N, Garcia D, Cornille N, Orteu JJ, McNeill SR, et al. Scanning electron microscopy for quantitative small and large deformation measurements part II: Experimental validation for magnifications from 200 to 10,000. Experimental Mechanics 2007;47(6):789–804.

[117] Kammers AD, Daly S. Digital image correlation under scanning electron microscopy: Methodology and validation. Experimental Mechanics 2013;53(9):1743–61.

[118] Meyer P, Waas AM. Measurement of in situ-full-field strain maps on ceramic matrix composites at elevated temperature using digital image correlation. Experimental Mechanics 2015;55(5):795–802.

[119] Gao G, Yao W, Xia K, Li Z. Investigation of the rate dependence of fracture propagation in rocks using digital image correlation (DIC) method. Engineering Fracture Mechanics 2015;138:146–55.

[120] Su YQ, Yao XF, Wang S, Ma YJ. Improvement on measurement accuracy of high-temperature DIC by grayscale-average technique. Optics and Lasers in Engineering 2015;75:10–6.

[121] Maynadier A, Poncelet M, Lavernhe-Taillard K, Roux S. One-shot measurement of thermal *and* kinematic fields: Infra-red image correlation (IRIC). Experimental Mechanics 2011;52(3):241–55.

[122] Charbal A, Roux S, Hild F, Vincent L. Spatiotemporal regularization for digital image correlation: Application to infrared camera frames. International Journal for Numerical Methods in Engineering 2018;114(12):1331–49.

[123] Charbal A, Vincent L, Hild F, Poncelet M, Dufour JE, Roux S, et al. Characterization of temperature and strain fields during cyclic laser shocks. Quantitative InfraRed Thermography Journal 2016;13(1):1–18. doi:10.1080/17686733.2015.1077544.

[124] Archer T, Beauchene P, Huchette C, Hild F. Global digital image correlation up to very high temperatures with grey level corrections. Measurement Science and Technology 2020;31(2):024003.

[125] Ciddor PE. Refractive index of air: new equations for the visible and near infrared. Applied optics 1996;35(9):1566–73.

[126] Mendoza A, Neggers J, Hild F, Roux S. Complete mechanical regularization applied to digital image and volume correlation. Computer Methods in Applied Mechanics and Engineering 2019;355:27 – 43. URL: http://www.sciencedirect.com/science/article/pii/S0045782519303457. doi:https://doi.org/10.1016/j.cma.2019.06.005.

[127] Mani NK, Haug EJ, Atkinson KE. Application of Singular Value Decomposition for Analysis of Mechanical System Dynamics. Journal of Mechanisms, Transmissions, and Automation in Design 1985;107(1):82–7.

[128] Hou Z. Adaptive singular value decomposition in wavelet domain for image denoising. Pattern Recognition 2003;36(8):1747–63.

[129] Trebuňa F, Huňady R, Bobovskỳ Z, Hagara M. Results and experiences from the application of digital image correlation in operational modal analysis. Acta Polytechnica Hungarica 2013;10(5):159–74.

[130] Grama SN, Subramanian SJ. Computation of full-field strains using principal component analysis. Experimental Mechanics 2014;54(6):913–33.

[131] Hao W, Zhu J, Zhu Q, Chen L, Li L. Displacement field denoising for high-temperature digital image correlation using principal component analysis. Mechanics of Advanced Materials and Structures 2017;24(10):830–9.

[132] Passieux JC, Périé JN. High resolution digital image correlation using proper generalized decomposition: PGD-DIC. International Journal for Numerical Methods in Engineering 2012;92(6):531–50.

[133] Charbal A, Roux S, Hild F, Vincent L. Spatiotemporal regularization for digital image correlation: Application to infrared camera frames. Int J Num Meth Eng 2018;114(12):1331–49.

[134] Babuška I, Rheinboldt W. Error estimates for adaptive finite element computation. SIAM J Num Anal 1978;15(4):736–54.

[135] Zhu J, Zienkiewicz O. Adaptive techniques in the finite element method. Communications in applied numerical methods 1988;4(2):197–204.

[136] Wittevrongel L, Lava P, Lomov SV, Debruyne D. A self adaptive global digital image correlation algorithm. Experimental Mechanics 2015;55(2):361–78.

[137] Kleinendorst S, Hoefnagels J, Verhoosel C, Ruybalid A. On the use of adaptive refinement in isogeometric digitalimage correlation. International Journal for Numerical Methods in Engineering 2015;104(10):944–62.

[138] Vuong AV, Giannelli C, Jüttler B, Simeon B. A hierarchical approach to adaptive local refinement in isogeometric analysis. Computer Methods in Applied Mechanics and Engineering 2011;200(49-52):3554–67.

[139] Baldi A, Bertolino F. Assessment of h-refinement procedure for global digital image correlation. Meccanica 2016;51(4):979–91.

[140] Sciuti VF, Vargas R, Canto RB, Hild F. Pyramidal adaptive meshing for dic

dealing with cracks. submitted for publication 2020;.

[141] ASTM C1424-15. Standard test method for monotonic compressive strength of advanced ceramics at ambient temperature. Tech. Rep.; ASTM International; 2015.

[142] Leplay P, Lafforgue O, Hild F. Analysis of asymmetrical creep of a ceramic at 1350 ℃ by Digital Image Correlation. Journal of the American Ceramic Society 2015;98(7):2240–7.

[143] Bayer BE. Color imaging array. 1976. US Patent 3,971,065.

[144] Vakulenko A, Kachanov M. Continuum theory of medium with cracks. Isv AN SSSR, Mekh Tverdogo Tela 1971;4:159–66.

[145] Baldi A, Bertolino F. Assessment of h-refinement procedure for global digital image correlation. Meccanica 2016;51:979–91.

[146] Panin S, Titkov V, Lyubutin P. Effect of the mesh size of the vector displacement field on the strain estimate in the digital image correlation method. Journal of Applied Mechanics and Technical Physics 2017;58:425–35.

[147] Réthoré J, Hild F, Roux S. Shear-band capturing using a multiscale extended digital image correlation technique. Comp Meth Appl Mech Eng 2007;196(49-52):5016–30.

[148] Réthoré J, Hild F, Roux S. Extended digital image correlation with crack shape optimization. Int J Num Meth Eng 2008;73(2):248–72.

[149] Roux S, Hild F, Leclerc H. Mechanical assistance to DIC. In: Espinosa H, Hild F, editors. Full field measurements and identification in Solid Mechanics; vol. Procedia IUTAM, 4. Elsevier; 2012, p. 159–68.

[150] Fagerholt E, Børvik T, Hopperstad OS. Measuring discontinuous displacement fields in cracked specimens using digital image correlation with mesh adaptation and crack-path optimization. Optics Lasers Eng 2013;51(3):299–310.

[151] Wang X, Ma S. Mesh-Based Digital Image Correlation Method Using Non-Uniform Elements for Measuring Displacement Fields with High Gradient. Experimental Mechanics 2014;54:1545–54.

[152] Vargas R, Tsitova A, Bernachy-Barbe F, Bary B, Canto R, Hild F. On the identification and validation of fracture mechanics models for curved crack

in mortar. Strain 2020;.

[153] Besnard G, Hild F, Roux S. “Finite-element” displacement fields analysis from digital images: Application to Portevin-Le Chatelier bands. Exp Mech 2006;46:789–803.

[154] Sciuti VF, Hild F, Pandolfelli VC, Santos T, Smaniotto B, Canto RB. Digital image correlation applied to *in situ* evaluation of surface cracks upon curing of MgO-containing refractory castables. Journal of European the Ceramic Society submitted to the Journal of the European Ceramic Society;.

[155] Salomão R, Pandolfelli VC. The role of hydraulic binders on magnesia containing refractory castables: calcium aluminate cement and hydratable alumina. Ceramics International 2009;35(8):3117–24.

[156] Lemaitre J. A Course on Damage Mechanics. 2 ed.; Berlin (Germany): Springer-Verlag; 1992. doi:10.1007/978-3-642-18255-6.

[157] Weibull W. A statistical theory of the strength of materials. Tech. Rep. Report 151; Roy. Swed. Inst. Eng. Res.; 1939.

[158] Weibull W. A statistical distribution function of wide applicability. ASME J Appl Mech 1951;18(3):293–7.

[159] Sciuti V, Hild F, Pandolfelli V, Santos T, Smaniotto B, Canto R. Digital Image Correlation applied to *in situ* evaluation of surface cracks upon curing of MgO-containing refractory castables. Journal of the European Ceramic Society 2021;41(1).

[160] Sciuti V, Canto R, Neggers J, Hild F. On the benefits of correcting brightness and contrast in global digital image correlation: Monitoring cracks during curing and drying of a refractory castable. Optics and Lasers in Engineering 2020;136:106316.